Contribution to the Design of a Real-Time Fourier Transformer in Integrated Technology

João Alberto De França Ferreira

université PARIS-SACLAY

CentraleSupélec

UNIVERSITÉ PARIS SUD
Comprendre le monde, construire l'avenir

NNT : 2019SACLS502

Thèse de doctorat

Contribution to the Design of a Real-Time Fourier Transformer in Integrated Technology

Thèse de doctorat de l'Université Paris-Saclay
préparée à l'Université Paris-Sud

Ecole doctorale n°575 Electrical, Optical, Bio: PHYSICS-AND-ENGINEERING (EOBE)
Spécialité de doctorat : électronique et optoélectronique, nano- et microtechnologies

Thèse présentée et soutenue à Gif-sur-Yvette, le le 11 décembre 2019, par

JOÃO ALBERTO DE FRANÇA FERREIRA

Composition du Jury :

Aziz Benlarbi-Delai Professeur des Universités (HDR), Sorbonne Université (L2E)	Président du Jury
Emilie Avignon-Meseldzija Maître de Conférence, CentraleSupélec (GeePs)	Examinateur
François Rivet Maître de Conférence (HDR), Bordeaux INP (IMS)	Rapporteur
Hassan Aboushady Maître de Conférence (HDR), Sorbonne Université (LIP6)	Rapporteur
Hervé Barthelemy Professeur des Universités (HDR), Université de Toulon (IM2NP)	Examinateur
Mathieu Thevenin Scientist/Researcher, CEA Saclay (LETS)	Invité
Philippe Bénabès Professeur des Universités (HDR), CentraleSupélec (GeePs)	Directeur de thèse
Pietro Maris Ferreira Maître de Conférence, CentraleSupélec (GeePs)	Invité

Contents

Résumé

Titre : Contribution à la Conception d'un Transformateur de Fourier Temps Réel en Technologie Intégrée

Mots clés : traitement du signal analogique, temps réel, transformateur de Fourier à modulation de fréquence, rétard de groupe arbitraire, filtre dispersif, circuit intégré

Contexte et Positionnement de ce Travail de Thèse

L'accroissement constant des bandes passantes et des débits dans les applications de la vie courante (e.g., télécommunications, objets connectés), comme dans des applications plus spécialisées (e.g., radar, observations en radioastronomie), imposent de très fortes contraintes en termes de vitesse, consommation de puissance et dissipation thermique aux étages de conversion analogique-numérique des chaînes d'acquisition. Par conséquent une tendance actuelle consiste à effectuer le traitement de signaux (comme la transformation de Fourier) dans le domaine analogique pour pouvoir traiter des signaux ultra-large bande avec une faible latence et de manière plus efficace en termes énergétiques.

L'étude de l'état de l'art effectué dans le cadre de la thèse, sur les architectures de calcul de la transformée de Fourier directement dans le domaine analogique et en temps réel, a mis en évidence deux grandes approches. L'une de ces approches consiste à implémenter avec des solutions analogiques intégrées l'algorithme de la FFT [1–7]. Cette approche s'avère très efficace pour repérer les sous-bandes où se trouve le signal et permet alors aux convertisseurs analogique-numérique de travailler à cadence très réduite et de lever le verrou préalablement cité. Si initialement cette approche nécessitait un gros budget en puissance, les dernières réalisations à base de réutilisation de charge [4–7] ont montré qu'il était possible de considérablement diminuer ce budget puissance. Mais les difficultés liées à cette approche échantillonnée restent cependant : la complexité des circuits, la grande précision exigée sur les valeurs d'échantillons, la consommation qui augmente avec la fréquence d'échantillonnage et enfin la résolution qui dépend de cette fréquence d'échantillonnage.

L'autre grande approche se base sur des architectures à base de filtres dispersifs [8–11]. De tels filtres, encore relativement peu explorés dans la littérature, présentent des retards de groupe différents en fonction de la fréquence. Suivant les applications, la caractéristique du retard de groupe en fonction de la fréquence devra être différemment dimensionnée. On parle alors de filtre à retard de groupe arbitraire. Ces filtres à retard de groupe arbitraires sont plutôt

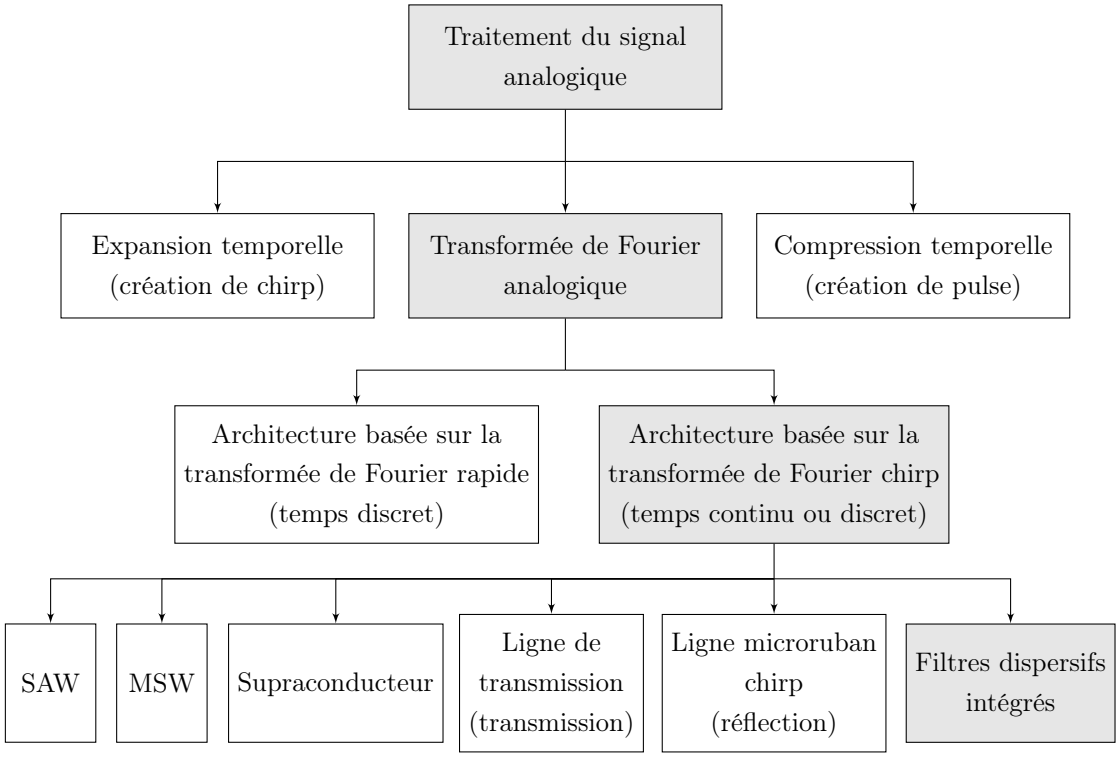

FIGURE 1 – Positionnement de ce travail de thèse par rapport à l'état de l'art.

jusqu'à aujourd'hui réalisés en technologie SAW ou avec des structures microondes discrètes (non intégrées), conduisant à des filtres avec des bandes passantes limitées et beaucoup de pertes, dans le cas des dispositifs SAW, ou avec un encombrement et poids importants, dans le cas des filtres microondes. Très peu de réalisations intégrées en semi-conducteurs ont été reportées à ce jour.

Dans ce contexte, l'orientation de recherche de ce travail de thèse est l'approche temps continu à base de filtres dispersifs pour obtenir un transformateur de Fourier analogique temps réel intégré qui soit large bande, compact et de faible consommation.

Dans le contexte de cette orientation de recherche, plusieurs verrous ont pu être levés pour obtenir un tel transformateur de Fourier :

- des solutions architecturales haut niveau visant à améliorer la précision des spectres obtenus sont proposées ;

- une méthode mathématique de conception de filtres à retard de groupe arbitraire a été mise en œuvre pour la conception de plusieurs filtres à retard de groupe linéaire en technologie intégrée ST BiCMOS 130 nm.

La Figure 1 vient situer ce travail de thèse parmi les différentes orientations de recherche de l'état de l'art. Il est à noter que l'apport de cette thèse sur l'aspect conception de filtres dispersifs ne se limite pas au dispositif de transformation de Fourier mais présente un intérêt pour de très nombreuses applications de traitement du signal analogique, comme le traitement de signaux large bande en radars et la discrimination de fréquences dans des systèmes de communication.

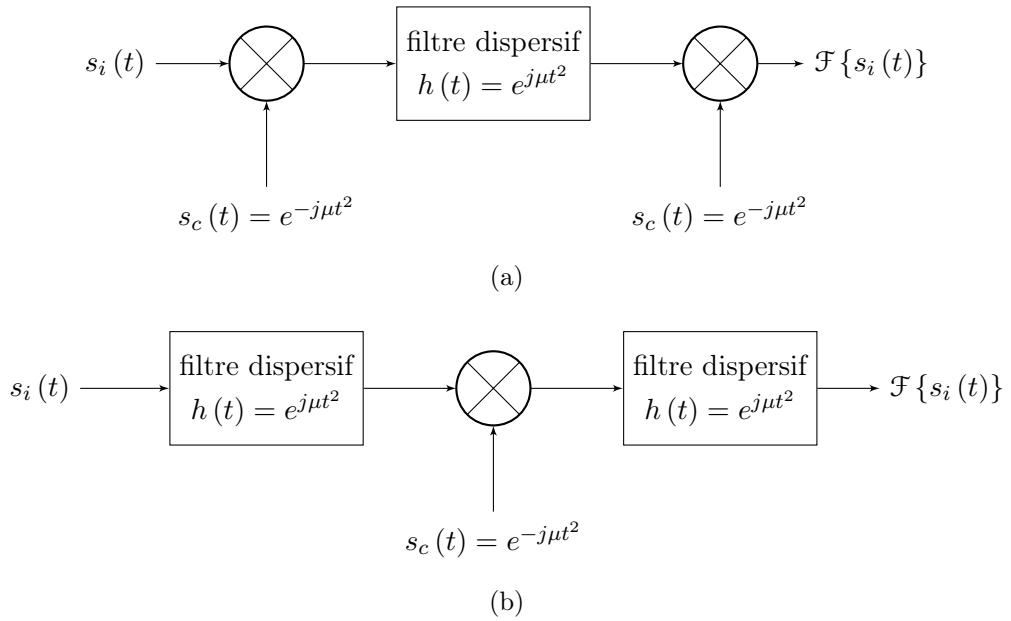

FIGURE 2 – Algorithmes pour la réalisation de la transformée de Fourier : (a) multiplier-convoluer-multiplier (MCM) et (b) convoluer-multiplier-convoluer (CMC).

Etude d'Architectures de Transformateur de Fourier à Modulation de Fréquence

Pour l'orientation choisie dans cette thèse, l'architecture de transformateur de Fourier basé sur la transformée chirp est considérée. La transformée se nomme ainsi en raison de l'utilisation de signaux chirp (modulés en fréquence) et de filtres dispersifs à réponse impulsionnelle chirp (donc également modulés en fréquence). La littérature mentionne deux algorithmes capables de calculer la transformée de Fourier selon cette approche, appelés MCM (Multiplier-Convoluer-Multiplier) et CMC (Convoluer-Multiplier-Convoluer). Elles sont présentées en Figures 2a et 2b.

Dans ce travail, le schéma MCM de la Figure 2a est développé pour obtenir l'architecture d'un transformateur de Fourier analogique physiquement implémentable et sans décalage fréquentiel dans le spectre. Le développement aboutit à deux modèles analytiques pour le système. Un modèle analytique avec un niveau d'abstraction élevé, exprimé en termes d'exponentielles complexes, et un modèle analytique de niveau d'abstraction plus basse, mais capable d'implémentation physique et exprimé en termes de fonctions trigonométriques.

Il est montré que le système exécute la transformée de Fourier finie, car le signal à la sortie du transformateur peut être mappé sur le domaine fréquentiel par le biais d'une relation linéaire donnée par la caractéristique des signaux et des filtres chirp (qui ont tous la même caractéristique selon une relation temps-fréquence). Un exemple analytique montre le principe de fonctionnement du système. Basé sur le modèle simplifié du transformateur, la Figure 3 illustre cet exemple. Les composantes spectrales ont une amplitude et une résolution qui augmentent (ou s'améliorent) avec le temps en raison de la limitation temporelle de la transformation.

Ensuite, afin d'évaluer la viabilité d'une implémentation physique de l'architecture proposée, l'influence des variations des paramètres du système est étudiée, la principale étant la différence entre le taux de variation de la fréquence du signal chirp et la caractéristique du retard de groupe

par rapport à la fréquence du filtre chirp. La conclusion sur ce travail montre que des imperfections dans la caractéristique linéaire du retard de groupe des filtres chirp conduisent à une diminution de la résolution spectrale, une réduction de l'amplitude des composantes spectrales et un décalage du spectre (une erreur dans la relation de correspondance entre les domaines temporel et fréquentiel). D'une manière générale, l'architecture est viable pour une implémentation physique. Cependant, la viabilité de l'architecture pour une application spécifique dépendra de l'amplitude des non-idéalités affectant le système et des exigences imposées par cette application.

En outre, sur la base de l'architecture proposée pour le transformateur de Fourier, un schéma est proposé pour égaliser l'amplitude et la résolution des composantes spectrales, comme le montre la Figure 4. Ce schéma est proposé en observant le fait qu'un transformateur de Fourier implémenté avec des chirps dont la fréquence décroît avec le temps, génèrent un spectre inversé dans le temps. Il est ensuite suggéré que ce spectre soit inversé [12] pour correspondre au spectre donné par un transformateur de Fourier implémenté avec des chirps dont la fréquence accroît avec le temps, afin que les spectres puissent être additionnés et aboutissent à un spectre avec toutes les composantes spectrales égalisées en amplitude et en résolution spectrale.

Dans toutes ces architectures, les filtres à retard de groupe linéaire sont l'élément clef, le reste de la thèse concerne ainsi la synthèse mathématique et la mise en œuvre électronique de tels filtres.

Conception de Filtres Passe-Bande Dispersifs à Retard de Groupe Arbitraire

Une première version de filtre à retard de groupe arbitraire est mise en œuvre via des réseaux en échelle à double terminaison. Ces filtres sont intéressants pour présenter une faible sensibilité aux variations des valeurs des composants.

Après un état de l'art effectué en théorie des filtres, une méthode récursive qui permet d'obtenir des polynômes à phase arbitraire est introduite. Ce polynôme est utilisé pour générer la fonction de transfert d'un filtre prototype passe-bas à retard de groupe linéaire. Ce filtre prototype peut ensuite, être transformé dans un autre type (passe-haut, passe-bande ou coupe-bande)

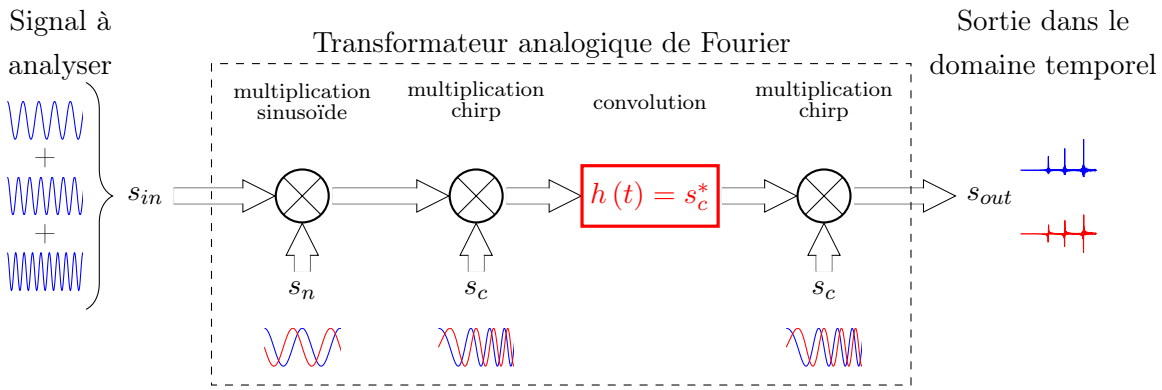

FIGURE 3 – Schéma synoptique simplifié du transformateur de Fourier analogique en temps réel illustrant la transformation d'un signal à trois tons et tous les signaux complexes nécessaires à son fonctionnement.

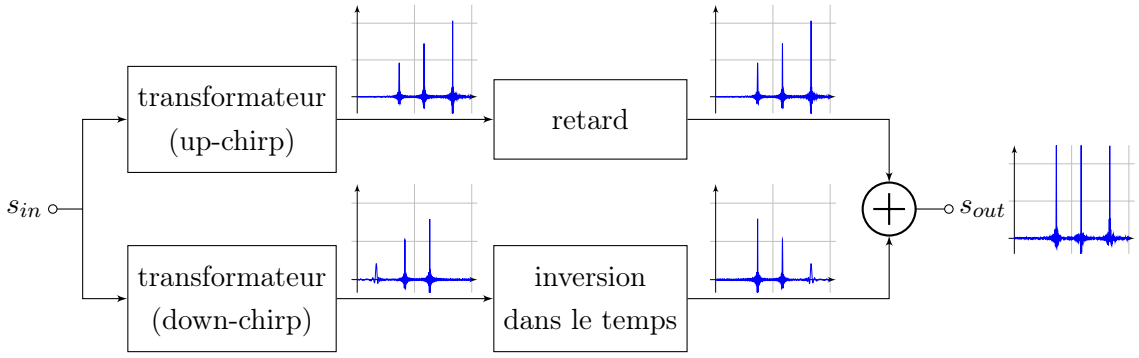

FIGURE 4 – Schéma pour égaliser la variation en amplitude des composantes spectrales e la résolution spectrale, avec les représentations graphiques montrant uniquement la partie réelle du spectre résultant d'un signal d'entrée sinusoïdale à trois tons.

et synthétisé dans une structure en échelle. Les valeurs des composants sont déterminées en fonction du niveau d'impédance et de la bande de fréquence spécifiés. Cette méthode a été utilisée pour concevoir un filtre avec une bande passante de 500 MHz autour de 1 GHz. Le filtre a été implémenté dans une technologie BiCMOS de 0.13 µm utilisant les condensateurs metal-insulator-metal (MIM) et les inductances planaires de la technologie. Ont également été illustrées la distorsion dans la caractéristique du retard de groupe provoquée par la transformation passe-bande et la relation entre la largeur de bande et l'amplitude du retard de groupe, où l'amplitude du retard de groupe diminue avec l'augmentation de la largeur de bande du filtre et vice versa (voir Figure 5).

Conception de Filtres Passe-Tout Dispersifs à Retard de Groupe Arbitraire

Une deuxième version de filtre à retard de groupe linéaire se base sur des filtres passe-tout à résistance constante. L'avantage de ces filtres est que ce sont des filtres à résistance constante, ce qui facilite l'interfaçage avec d'autres circuits et la cascade de filtres pour augmenter l'amplitude du retard de groupe. Bien entendu, les implémentations pratiques de ces filtres entraînent des pertes et leur cascade entraîne l'accumulation des pertes. Cependant, des filtres transversaux actifs peuvent être créés sur la base des filtres passe-tout conçus.

Pour concevoir ces filtres, la méthode récursive est à nouveau utilisée pour générer la fonction de transfert d'un filtre passe-tout prototype qui est ensuite denormalisé en impédance et fréquence. Cette méthode a été utilisée pour concevoir deux filtres passe-tout d'ordre quatre, l'un avec un retard de groupe linéaire à pente négative, mis en oeuvre via un réseau en treillis (équilibré) et un autre avec un retard de groupe linéaire à pente positive, mais implémenté par un réseau en T ponté (non équilibré). Le schéma et le layout du filtre en treillis sont montrés à la Figure 6, tandis que la Figure 8 illustre le schéma et le layout du filtre en T ponté. Des simulations électromagnétiques quasi-statiques du layout complète des filtres ont été réalisées pour extraire les réponses en fréquence des filtres dans le cas typique (RCTYP) et dans les cas où les parasites sont au minimum (RCMIN) et au maximum (RCMAX). Ces simulations sont montrés dans la Figure 7, pour le filtre en treillis, et dans la Figure 9, pour le filtre en T ponté.

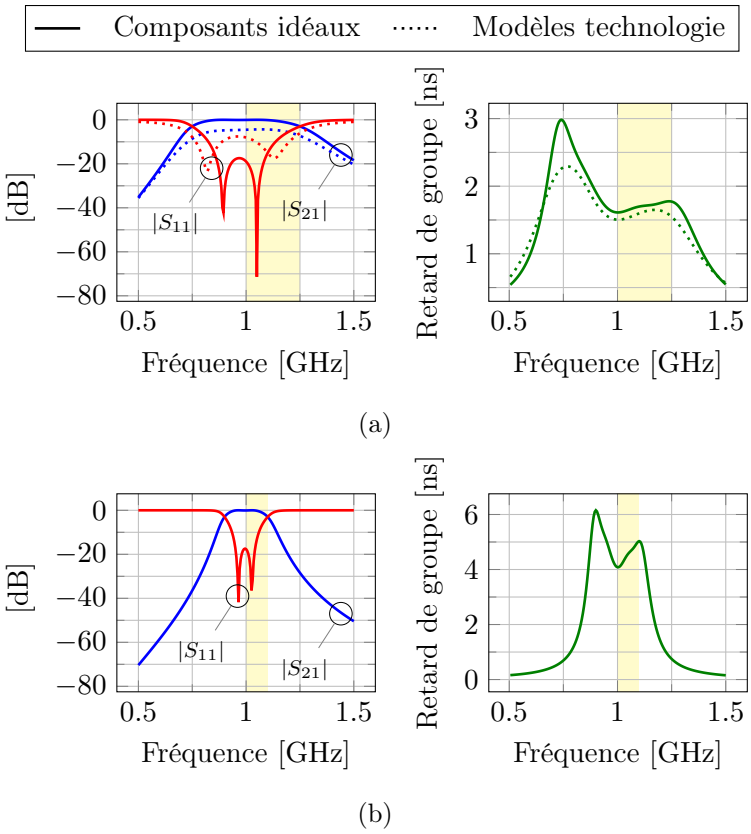

FIGURE 5 – Réponse en fréquence et retard de groupe pour : (a) un réseau en échelle à bande passante centré sur 1 GHz et avec une largeur de bande de 500 MHz, (b) un réseau en échelle à bande passante centré sur 1 GHz et avec une largeur de bande de 200 MHz.

Comparés à l'état de l'art en termes de filtres de retard de groupe linéaire intégrés, les filtres conçus ont un retard de groupe bien linéaire et une réponse en amplitude uniforme sur toute leur bande.

Conclusion et Perspectives

Ce travail de thèse s'est concentré sur la problématique de conception d'un transformateur de Fourier temps réel à modulation de fréquence. Une architecture de type MCM a été proposée pour améliorer la précision spectrale par rapport à celles implémentées précédemment. Puis le travail de recherche s'est concentré sur la conception de filtre à retard de groupe arbitraire grâce à une méthode récursive pour obtenir la fonction de transfert souhaitée. Plusieurs types de filtres ont été conçus avec la technologie ST BiCMOS 130 nm.

Quelques idées peuvent être explorées pour aider à la mise en œuvre physique de l'architecture de transformateur de Fourier proposée. Une de ces idées, pour permettre l'augmentation de l'amplitude du retard de groupe, est de généraliser le méthode récursive de génération de polynômes à phase arbitraire [13] afin de permettre la génération de polynômes à coefficients complexes. Ensuite, les fonctions de transfert composées de tels polynômes peuvent être synthétisées au moyen de réseaux de résonateurs couplés [14, 15]. Une autre idée est de tirer parti des filtres passifs précédemment synthétisés dans une architecture de filtre transverse (basée sur

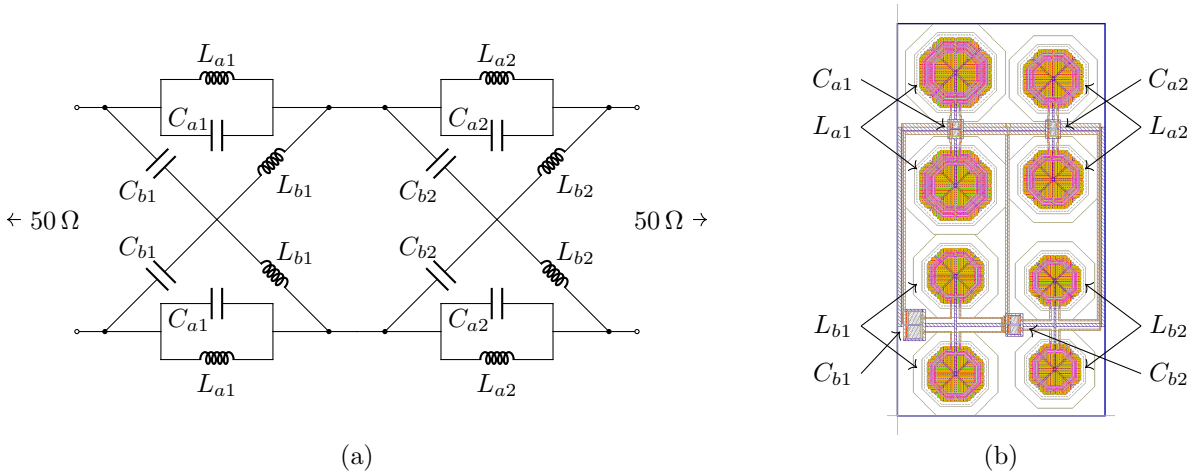

(a) (b)

FIGURE 6 – Filtre passe-tout en treillis à résistance constante : (a) schéma, et (b) layout.

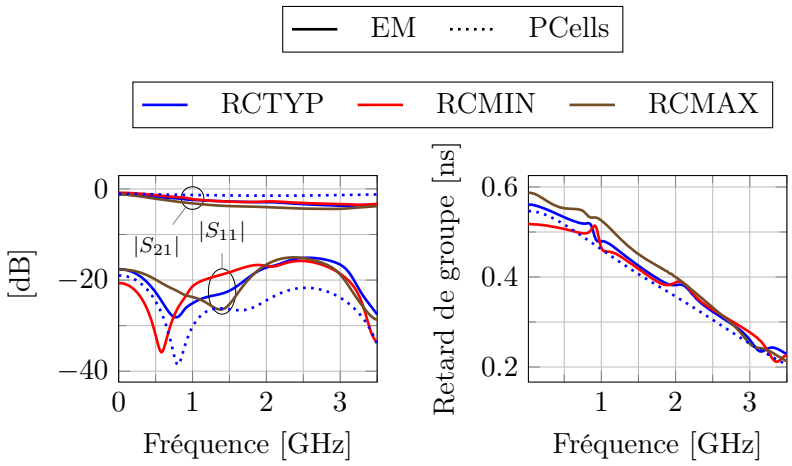

FIGURE 7 – Réponse en fréquence et retard de groupe du filtre en treillis de la Figure 6.

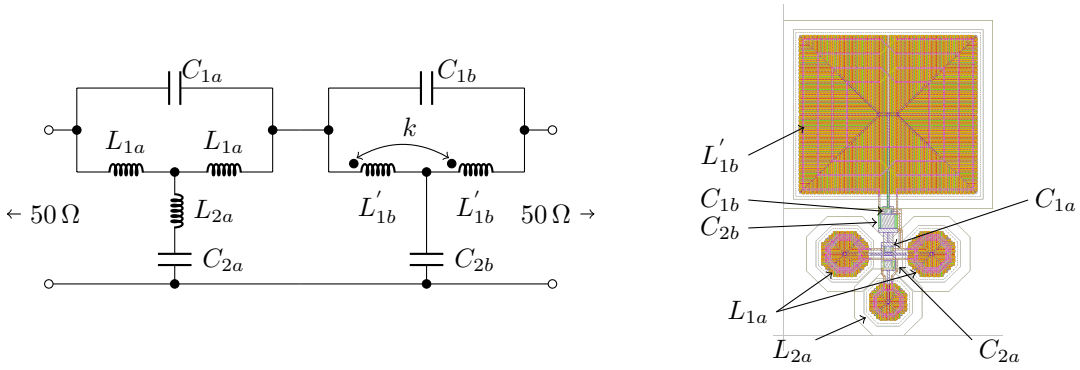

(a) (b)

FIGURE 8 – Filtre passe-tout en T ponté à résistance constante : (a) schéma, et (b) layout.

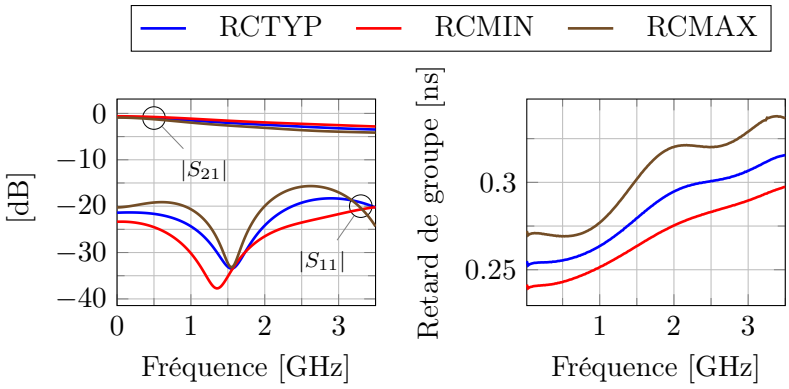

FIGURE 9 – Réponse en fréquence et retard de groupe du filtre en T ponté de la Figure 8.

une structure d'amplificateur distribué), comme déjà reporté dans la littérature [16, 17]. Pour minimiser les effets des imperfections intrinsèques à une implémentation physique, la mise en place d'un système de contrôle permettant d'adapter le signal chirp (généré de manière actif) à la réponse impulsionnelle du filtre chirp, comme reporté en [18], est très intéressant.

Références

[1] F. RIVET, Y. DEVAL, J.-B. BEGUERET, D. DALLET et D. BELOT, "A disruptive software-defined radio receiver architecture based on sampled analog signal processing", in *Proc. 2007 IEEE Radio Frequency Integrated Circuits Symp.*, Honolulu, HI, USA : IEEE, juin 2007, p. 197–200. DOI : 10.1109/RFIC.2007.380864.

[2] F. RIVET, Y. DEVAL, J.-B. BEGUERET, D. DALLET, P. CATHELIN et D. BELOT, "A disruptive receiver architecture dedicated to software-defined radio", *IEEE Trans. Circuits Syst. II, Exp. Briefs*, t. 55, n° 4, p. 344–348, avr. 2008. DOI : 10.1109/TCSII.2008.919512.

[3] ——, "The experimental demonstration of a SASP-based full software radio receiver", *IEEE J. Solid-State Circuits*, t. 45, n° 5, p. 979–988, mai 2010. DOI : 10.1109/JSSC.2010.2041402.

[4] B. SADHU, M. STURM, B. M. SADLER et R. HARJANI, "A 5gs/s 12.2 pJ/conv. analog charge-domain FFT for a software defined radio receiver front-end in 65nm CMOS", in *2012 IEEE Radio Frequency Integrated Circuits (RFIC) Symp. Dig. Papers*, Montreal, QC, Canada : IEEE, juin 2012, p. 39–42. DOI : 10.1109/RFIC.2012.6242227.

[5] ——, "Analysis and design of a 5 GS/s analog charge-domain FFT for an SDR front-end in 65 nm CMOS", *IEEE J. Solid-State Circuits*, t. 48, n° 5, p. 1199–1211, mai 2013. DOI : 10.1109/JSSC.2013.2250457.

[6] H. SHIN, R. K. PALANI, A. SAHA, F.-L. YUAN, D. MARKOVIC et R. HARJANI, "An eight channel analog-FFT based 450ms/s hybrid filter bank ADC with improved SNDR for multi-band signals in 40nm CMOS", in *2015 IEEE Custom Integrated Circuits Conf.*, San Jose, CA, USA : IEEE, sept. 2015, p. 1–4. DOI : 10.1109/CICC.2015.7338459.

[7] H. Shin et R. Harjani, "Low-power wideband analog channelization filter bank using passive polyphase-FFT techniques", *IEEE J. Solid-State Circuits*, t. 52, n° 7, p. 1753–1767, juil. 2017. doi : 10.1109/JSSC.2017.2700792.

[8] C. Atzeni, G. Manes et L. Masotti, "Programmable signal processing by analog chirp-transformation using SAW devices", in *1975 Ultrasonics Symp. Proc.*, Los Angeles, CA, USA : IEEE, sept. 1975, p. 371–376. doi : 10.1109/ULTSYM.1975.196539.

[9] O. W. Otto, "The chirp transform signal processor", in *1976 Ultrasonics Symp.*, Annapolis, MD, USA : IEEE, oct. 1976, p. 365–370. doi : 10.1109/ULTSYM.1976.196699.

[10] M. A. Jack, P. M. Grant et J. H. Collins, "The theory, design, and applications of surface acoustic wave Fourier-transform processors", *Proc. IEEE*, t. 68, n° 4, p. 450–468, avr. 1980. doi : 10.1109/PROC.1980.11674.

[11] C. Campbell, *Surface Acoustic Wave Devices and Their Signal Processing Applications*. London, UK : Academic Press, Inc., 1989, chap. 16, isbn : 0-12-157345-1.

[12] J. Zhang et J. Yao, "Broadband and precise microwave time reversal using a single linearly chirped fiber Bragg grating", *IEEE Trans. Microw. Theory Techn.*, t. 63, n° 7, p. 2166–2172, juil. 2015. doi : 10.1109/TMTT.2015.2432016.

[13] T. Henk, "The generation of arbitrary-phase polynomials by recurrence formulae", *Int. J. Circ. Theor. Appl.*, t. 9, n° 4, p. 461–478, oct. 1981. doi : 10.1002/cta.4490090407.

[14] W. Meng, H.-M. Lee, K. A. Zaki et A. E. Atia, "Synthesis of multi-coupled resonator filters with frequency-dependent couplings", in *2010 IEEE MTT-S Int. Microwave Symp. Dig.*, Anaheim, CA, USA : IEEE, mai 2010, p. 1716–1719. doi : 10.1109/MWSYM.2010.5517793.

[15] W. Meng, K. A. Zaki et A. E. Atia, "Prototype network synthesis for wideband microwave filters", in *2011 IEEE MTT-S Int. Microwave Symp. Dig.*, Baltimore, MD, USA : IEEE, juin 2011, p. 1–4. doi : 10.1109/MWSYM.2011.5972894.

[16] B. Xiang, "Integrated Dispersive Delay Line (DDL) for Real Time Analog Signal Processing", en, Doctoral thesis, Cornell University, août 2012.

[17] A. Salvucci, S. Colangeli, M. Palomba, G. Polli et E. Limiti, "An active dispersive delay line in GaN MMIC technology for X-band applications", in *2016 21st Int. Conf. Microwave, Radar and Wireless Commun.*, Krakow, Poland : IEEE, mai 2016, p. 1–4. doi : 10.1109/MIKON.2016.7492059.

[18] G. L. Villanueva, P. Hartogh et L. M. Reindl, "A digital dispersive matching network for SAW devices in chirp transform spectrometers", *IEEE Trans. Microw. Theory Techn.*, t. 54, n° 4, p. 1415–1424, juin 2006. doi : 10.1109/TMTT.2006.871244.

List of Figures

List of Tables

Acronyms

ADC analog-to-digital converter.

AOS acousto-optical spectrometer.

ASIC application-specific integrated circuit.

ASP analog signal processing.

CEBG chirped electromagnetic bandgap.

CMC convolve-multiply-convolve.

CMOS complementary metal-oxide-semiconductor.

CRAFT charge reuse analog Fourier transform.

CRLH composite right/left-handed.

CT chirp transform.

CTS chirp transform spectrometer.

CZT chirp Z-transform.

DA distributed amplifier.

DAC digital-to-analog converter.

D-CRLH dual composite right-left handed.

DDL dispersive delay line.

DDS direct digital synthesis.

DFT discrete Fourier transform.

DSP digital signal processing.

EM electromagnetic.

FDMA frequency division multiple access.

FFT fast Fourier transform.

FM frequency modulated.

FPGA field-programmable gate array.

FWHM full width at half maximum.

GaN gallium nitride.

GREAT German REceiver for Astronomy at Terahertz frequencies.

HWHM half width at half maximum.

IBW instantaneous bandwidth.

IC integrated circuit.

IDT interdigital transducer.

IF intermediate frequency.

IIP3 third order input intercept point.

IoT internet of things.

LCFBG linearly chirped fiber Bragg grating.

LCFG linearly chirped fiber grating.

LCIC linearly chirped intermodal coupler.

LPE liquid phase epitaxial.

MCD multicarrier demodulator.

MCM multiply-convolve-multiply.

MIM metal-insulator-metal.

MIRO Microwave Instrument for Rosetta Orbiter.

MIT Massachusetts Institute of Technology.

MMIC monolithic microwave integrated circuit.

MSW magnetostatic wave.

NUTL nonuniform transmission line.

OTA operational transconductance amplifier.

PCell parameterized cell.

PED portable electronic device.

PGS patterned ground shield.

PLL phase-locked loop.

QPSK quadrature phase-shift keying.

RAC reflective array compressor.

REIC rare-earth ion doped crystals.

RF radio frequency.

RMS roor mean square.

ROM read only memory.

RTACFT real-time analog chirp Fourier transformer.

SASP sampled analog signal processor.

SAW surface acoustic wave.

SDR software-defined radio.

SH sample-and-hold.

SHB spectral hole burning.

SNDR signal-to-noise and distortion ratio.

SOFIA Stratospheric Observatory For Infrared Astronomy.

TBP time-bandwidth product.

TBWP time-bandwidth product.

TDM time division multiplexed.

TL transmission line.

UWB ultra-wideband.

VCO voltage controlled oscillator.

VGA variable gain amplifier.

YAG yttrium aluminum garnet.

YIG yttrium iron garnet.

Symbols

φ arbitrary phase value of a signal (in units of cycles).

$\phi(t)$ instantaneous phase of a signal (in units of rad).

ω_0 frequency of a single-tone sinusoid (in units of rad/s).

$A(t)$ time-varying amplitude of signal.

$f(t)$ instantaneous frequency of a signal (in units of Hz).

f_0 frequency of a single-tone sinusoid (in units of Hz).

f_1 chirp start frequency (in units of Hz); frequency of the complex sinusoid (in units of Hz).

f_2 chirp end frequency (in units of Hz).

$h(t)$ impulse response of a complex filter.

k rate of change of chirp (in units of Hz/s or, equivalently, cycles/s^2).

s_c complex chirp signal.

s_i input signal.

s_n complex sinusoid.

T sweep time of the chirp or group delay swing of the filter (in units of s).

Chapter 1

Introduction

Modern life is full of practical applications that need to process a large amount of information in real-time. Many emerging applications even require processing capabilities that far exceed the capabilities of today's digital processing systems. To give an idea, applications such as pulse-compression radar, spread-spectrum communications, and electronic warfare require digital systems with processing capacity on the order of 10^{12} operations per second. In terms of instantaneous bandwidths[1], requirements are on the order of 10 GHz [1].

With the widespread use of portable electronic devices (PEDs) and communications systems (wired and wireless), and the advent of the internet of things (IoT), not only the amount of information to be processed has significantly increased, but the requirements of reliability, portability, and responsiveness of processing devices have become much more stringent. These requirements usually result in the need for low power integrated circuits (ICs) with low latency and high processing power.

Processing devices commonly employ digital signal processing (DSP) circuits due to their flexibility and reliability. However, DSP circuits face unprecedented challenges to comply with the requirements of real-time operation, higher operating frequencies, and low power consumption imposed by emerging applications. When operating at high-frequency ranges, like the decimeter-, centimeter-, and millimeter-wave bands, DSP circuits face significant technical hurdles, such as high power consumption and heat dissipation, decreasing noise margins, and limited performances of interfacing data converters.

Analog signal processing (ASP) has recently reemerged as an alternative or complementary approach to DSP for processing ultra-wideband radio frequency signals [2]. It enables devices to perform real-time signal processing at higher operating frequencies and with lower power consumption. The most critical and fundamental components of ASP systems are filters with engineered group delay. Each application requires filters with specific group delay characteristics. For instance, Fourier transformers require filters with linear group delay [3], while spectrum sniffers require filters with a stair shaped characteristic [4].

[1] *Instantaneous bandwidth (IBW)* refers to the bandwidth in which all frequency components can be simultaneously captured and analyzed.

1.1 Motivation

Whether working on DSP or ASP, numerous applications need to transform signals from the time domain to the frequency domain, and vice versa, to facilitate the analysis and performance of particular operations.

In DSP, the primary transform used is the *fast Fourier transform (FFT)*, which is, actually, an optimized algorithm that computes the *discrete Fourier transform (DFT)*. Which, in turn, is a particular case of the *Z-transform*. In ASP, the primary transform used is the *Fourier transform*, a particular case of the more general *Laplace transform*.

Regarding DSP, the FFT is the most efficient way to transform a digital signal in the time domain to the frequency domain and is generally implemented in general-purpose computers, digital signal processors, application-specific integrated circuits (ASICs) or field-programmable gate arrays (FPGAs). Although different implementations of the FFT are capable of processing ultra-wideband signals, under the constraint of real-time operation, their performances are limited by the conversion speed and power consumption of interfacing analog-to-digital and digital-to-analog data converters [3, 5, 6]. They also present high power consumption and difficulties with the decreasing noise margins and with the increasing heat generated, consequences of operating at high frequencies.

Furthermore, since complementary metal-oxide-semiconductor (CMOS) technology is the foundation of modern digital circuits, and the scaling trend of CMOS transistors is approaching its limit, it is unlikely that digital technology can continue to increase its operating frequency indefinitely.

In order to overcome the difficulties encountered by digital systems operating at high frequencies, this thesis is interested in exploring the realization of the Fourier transform through the ASP approach. Such a system could be used in a variety of applications, such as spectrum analysis, network analysis, beamforming, waveform synthesis, in fields as varied as radar, sonar, communications, and radio astronomy.

1.2 Objectives

This thesis aims to study and develop an innovative ASP system capable of performing the Fourier transform of ultra-wideband signals in real-time, and that meets the performance requirements of emerging applications. An integrated circuit implementation in an IC technology compatible with the current technology used by digital systems will be considered during the development. Firstly, the work will focus on proposing the system architecture, and then the thesis will focus on the design of the basic block of the architecture, namely the linear group delay filter. As much as possible, the results obtained will be generalized in order to allow their use in other ASP applications.

1.3 Thesis Structure

The thesis presents in Chapter 2, the literature review and state of the art in systems capable of performing the Fourier transform of signals in the analog domain.

Chapter 3 introduces the proposed architecture for a real-time analog chirp Fourier transformer (RTACFT), explaining in detail its working principle and presenting an illustrative example. Then, system imperfections are modeled, and their effects are analyzed.

Chapters 4 and 5 deal with the design and synthesis of filters with engineered group delay, a main block in the proposed RTACFT architecture. More specifically, Chapter 4 discusses the design of minimum-phase filters with engineered group delay and their synthesis through ladder networks, while Chapter 5 considers the design of all-pass filters with engineered group delay and their synthesis through lattice and bridged-T networks. Both chapters present illustrative examples.

Chapter 6 presents the conclusions for the thesis and suggestions to eventual future works on the topic.

Chapter 2

Literature Review and State of the Art

After World War II, researchers were working on new techniques to increase radar capabilities, both in range and range resolution[1], to keep up with the requirements imposed by increasingly fast aircraft and missiles, capable of flying at ever-higher altitudes. The conventional pulsed radars were limited in range by the average power radiated, and in range resolution by the transmitted pulse width. Since range performance was improved by increasing the amount of energy being transmitted (i.e., increasing the area under the pulse curve in its power versus time plot) and range resolution was enhanced by reducing pulse width, it was impossible to simultaneously improve range and range resolution without increasing transmitter peak power. However, the increase in peak power introduced some drawbacks, such as the requirement for high voltage power supplies and tubes capable of withstanding the high power levels, and the likelihood of electrical arcing [7, 9].

In this context, Klauder et al. published in 1960 an entirely theoretical article on the theory and design of chirp radars [9], where they presented the concept of pulse compression as a way of simultaneously improving range and range resolution without needing to increase transmitter peak power.

In the pulse compression technique, a linear frequency modulated (FM) pulse signal of length T, constant amplitude, and sweeping a frequency band Δ, is generated and transmitted by the radar. An example of such a signal is depicted in Fig. 2.1a, while Fig. 2.1b gives its instantaneous frequency versus time characteristic. The received echo passes through a filter device with a delay characteristic equal to the one illustrated in Fig. 2.1c, resulting in an output signal with an envelope given by

$$\left| \sqrt{D} \frac{\sin(\pi \Delta t)}{\pi \Delta t} \right|, \tag{2.1}$$

where $D = T\Delta$ is known as the *dispersion factor*, *pulse compression ratio*, or, more commonly, *time-bandwidth product (TBP or TBWP)*.

In this article, the authors remarked that the envelope of the output signal of the filter (sketched in Fig. 2.1d) is the Fourier transform of the envelope of the input signal (shown dashed in Fig. 2.1a). Actually, the envelope of the filter output signal is the magnitude response of

[1] The *range* of a radar is the maximum target distance at which reliable echo returns can be expected [7], while the *range resolution* is the ability of a radar system to distinguish between two or more targets on the same bearing but at different ranges [8].

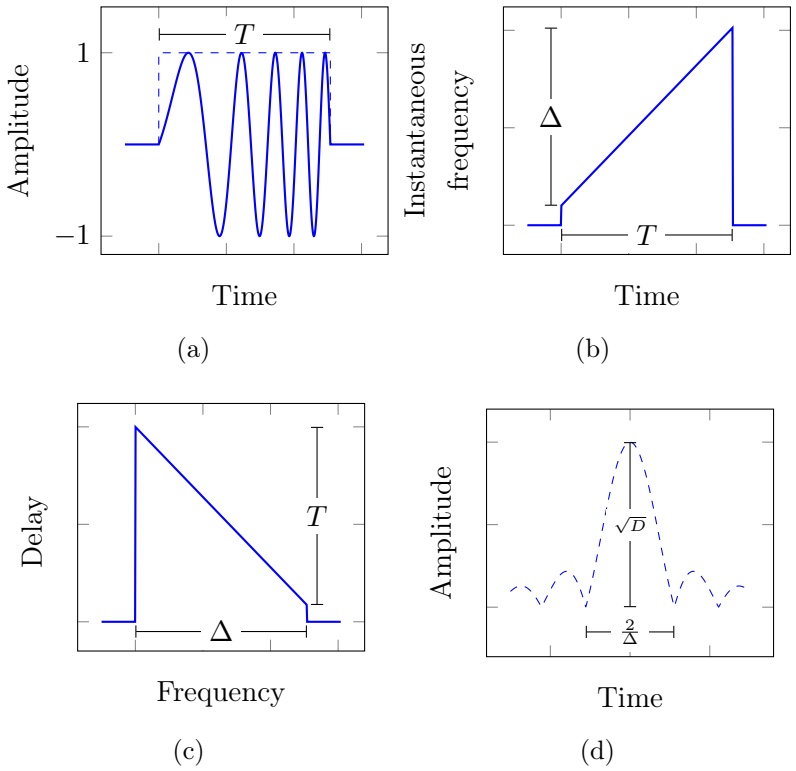

Figure 2.1 – (a) Idealized linear FM pulse signal (continuous line) and its rectangular envelope (dashed line). (b) Instantaneous frequency versus time characteristic of the linear FM pulse signal. (c) Filter network delay characteristic. (d) Envelope of the waveform outputted by the filter.

the Fourier transform of the envelope of the input signal. This remark sparked great interest, and several groups started researching systems capable of performing the Fourier transform of electronic signals. Consequently, research on filter devices with linear group delay, essentials in such systems, also proliferated.

2.1 Real-Time Fourier Transformers Employing SAW Devices

Apparently, Otto [10], in 1972, was the first to demonstrate the generation of Fourier transforms of electronic signals in real-time with an acoustic-surface-wave convolver, a nonlinear surface acoustic wave (SAW) device with two contra-directional inputs (cf. Fig. 2.2). In his work, Otto does not cite Klauder et al. [9], but acknowledges other authors, from fields, as optics and digital signal processing (DSP), as having previously observed that the operation of multiplying by a complex chirp[2], convolving with a complex chirp, and finally multiplying by a complex chirp (all chirps matched) corresponds to Fourier transformation.

Otto contemplated three configurations capable of performing real-time Fourier transformation. In the first configuration, the detector electrode would have a chirp wave vector response (i.e., a transducer whose periodicity is linearly tapered), with one of the inputs receiving the

[2]A chirp is a signal whose frequency changes with time (i.e., a frequency modulated (FM) signal). When the frequency increases, it is called an up-chirp. When the frequency decreases, it is called a down-chirp.

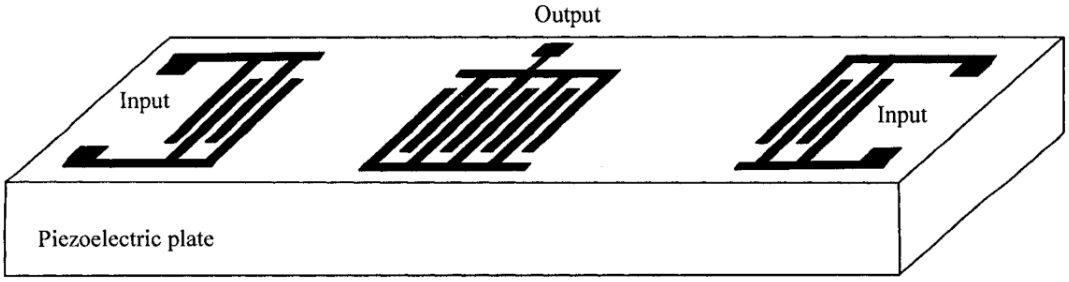

Figure 2.2 – Illustration of a SAW convolver (from [11]).

electronic signal to be transformed, mixed with a chirp matched to the detector electrode, and the second input receiving a continuous wave. The second configuration would have the same chirp-detector response, but the first input would receive the input signal to be analyzed modulating a radio frequency (RF) signal, while the second input would receive a chirp matched to the detector. The third configuration would employ a detector of uniform periodicity, with the first input receiving the signal to be transformed pre-multiplied by a chirp, and the second input receiving a chirp matched to the chirp on the first input.

In his demonstration, he used the third configuration, with a chirp presenting a duration of 1.2 µs and a bandwidth of 18 MHz, corresponding to a time-bandwidth product of 21.6.

In a later article [12], Otto analyzes the characteristics of surface wave implemented systems[3] that perform the Fourier transform. He calls this kind of system a *chirp transform (CT) processor*. In this article, he points out that two algorithms exist for the realization of the Fourier transform, referred to as the multiply-convolve-multiply (MCM), and the convolve-multiply-convolve (CMC), given by (2.2) and (2.3), respectively, where $s_i(t)$ is an input signal and $\mathcal{F}\{s_i(t)\}$ its Fourier transform, $s_c(t)$ is a complex chirp signal and $h(t)$ is the impulse response of a dispersive filter. These algorithms are illustrated in Fig. 2.3. He highlights that these algorithms are well known from optics, where lenses perform quadratic phase (chirp) multiplication, and that diffraction through a distance convolves the object against the point response of the medium (a quadratic phase front in the para-axial approximation).

$$\mathcal{F}\{s_i(t)\} = s_c(t)\{[s_i(t)\, s_c(t)] * h(t)\} \tag{2.2}$$

$$\mathcal{F}\{s_i(t)\} = h(t) * \{[s_i(t) * h(t)]\, s_c(t)\} \tag{2.3}$$

In practice, the multiplying chirps and the impulse response of the dispersive filters have finite durations, leading to finite bandwidth and frequency resolution in the chirp transform processor, which results in what is called the finite Fourier transform (see Section 3.2). The filters impulse responses are more appropriately given by

$$h(t) = A_f W_f(t)\, e^{j\left(\omega_f t + \frac{\mu}{2}t^2\right)}, \tag{2.4}$$

where

$$W_f(t) = \begin{cases} 1, & \text{if } |t| \leqslant \frac{T_f}{2} \\ 0, & \text{otherwise} \end{cases} \tag{2.5}$$

[3]Beyond the SAW convolver, two other types of SAW devices are commonly employed in the realization of chirp filters (i.e., a filter with a chirp impulse response), the interdigital transducer (IDT) and the reflective array compressor (RAC), illustrated in Fig. 2.4. Table 2.1 gives typical values for some characteristics of these devices.

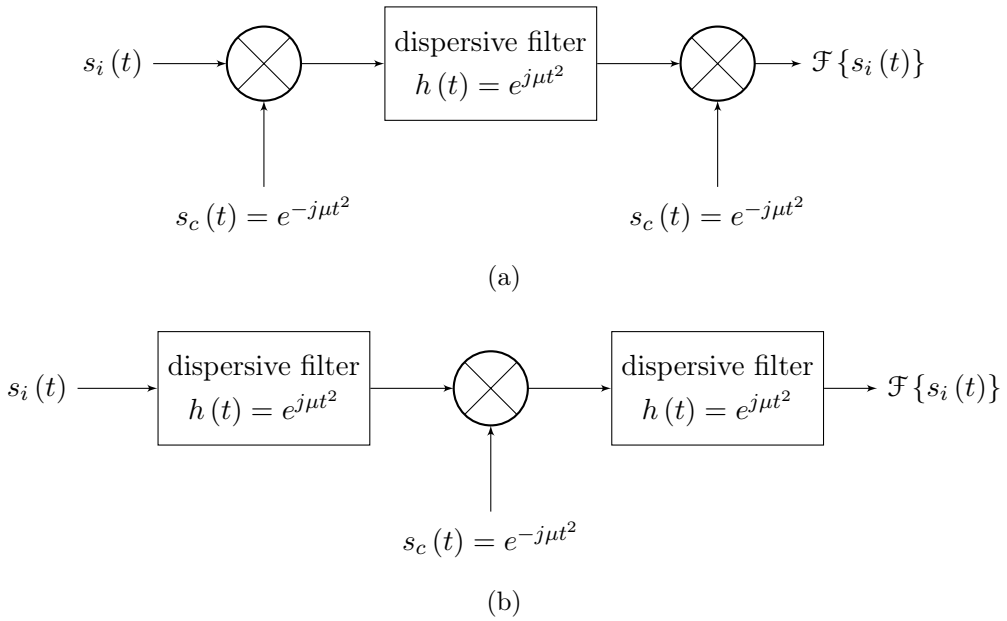

Figure 2.3 – Algorithms for the realization of the Fourier transform: (a) multiply-convolve-multiply (MCM) and (b) convolve-multiply-convolve (CMC).

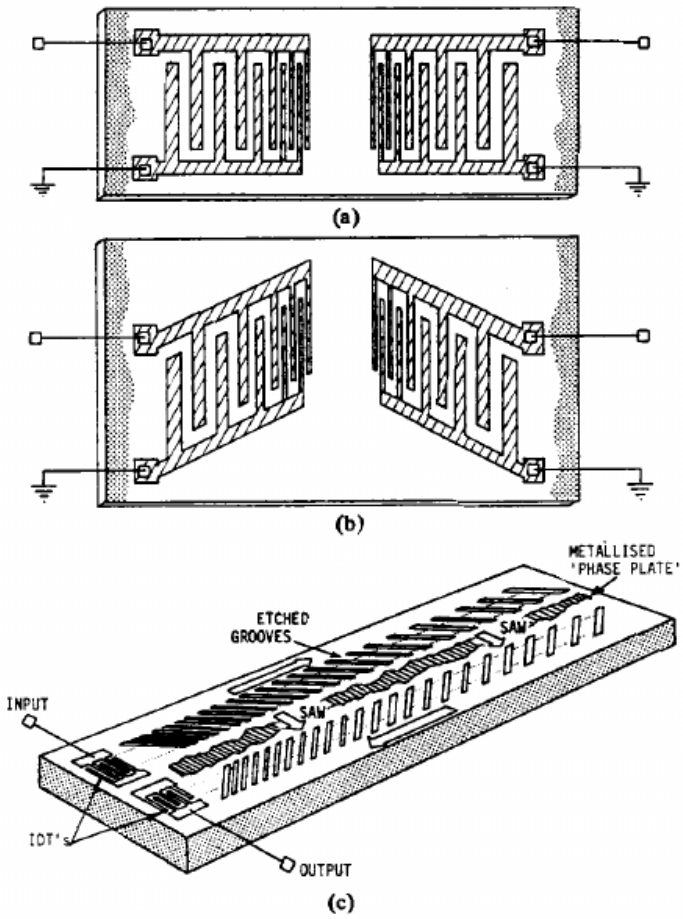

Figure 2.4 – Other types of SAW devices (chirp filters): (a) in-line interdigital transducer (IDT), (b) inclined IDT and, (c) reflective array compressor (RAC) device (from [5]).

Table 2.1 – Comparison of the characteristics of SAW IDT and RAC devices (adapted from [5]).

Parameter	IDT	RAC
Centre frequency (MHz)	10 to 1200	60 to 1200
Bandwidth (MHz)	1 to 500	1 to 500
Time dispersion (µs)	0.5 to 50	1 to 100
Time-bandwidth product	4 to 800	10 to 16 000
Ripple amplitude (dB peak-to-peak)	0.2	0.5
Phase error (degrees RMS)	0.5	0.5

is the window function, T_f is the group delay swing[4], A_f and ω_f are the amplitude and center frequency of the filter, respectively, and μ is the chirp slope (the ratio between bandwidth and group delay swing).

The multiplying chirps are given by

$$s_c(t) = A_c W_c(t)\, e^{j\left(\omega_c t - \frac{\mu}{2} t^2\right)}, \tag{2.6}$$

where

$$W_c(t) = \begin{cases} 1, & \text{if } |t| \leqslant \frac{T_c}{2} \\ 0, & \text{otherwise} \end{cases}, \tag{2.7}$$

and T_c, A_c, and ω_c are, respectively, the sweep time, amplitude, and center frequency of the chirp.

The input signal, $s_i(t)$, is assumed to be modulating a sinusoidal carrier signal of frequency $\omega = \omega_c - \omega_f$, i.e.,

$$s(t) = s_i(t)\, e^{j\omega t}. \tag{2.8}$$

Considering the MCM algorithm, the maximum bandwidth and time duration of the input signal, respectively, $\Delta\omega_{max}$ and t_{max}, are given by

$$\Delta\omega_{max} = \mu\,(T_f - T_c)\,, \tag{2.9}$$

$$t_{max} = T_c. \tag{2.10}$$

Based on (2.9) and (2.10), and considering that $T_c = \alpha T_f$, Otto defines the time-bandwidth product (TBWP) of the transform as

$$t_{max} \cdot \Delta\omega_{max} = \mu\alpha\,(1-\alpha)\,T_f^2, \tag{2.11}$$

and finds out that the TBWP has a maximum of $\frac{\mu T_f^2}{4}$ for $\alpha = 0.5$, concluding that the TBWP of the filters must be at least four times that of the processor.

The chirp transform corresponding to $\alpha < 1$ ($T_f > T_c$) is named the *"true"* (or *direct* [13]) *transform*, while the transform corresponding to $\alpha > 1$ ($T_f < T_c$) is called the *"sliding" transform*.

[4] *Group delay swing* (T in Fig. 2.1c) is the difference between the maximum and minimum group delay values in the filter passband. For a linear chirp filter, the maximum and minimum group delay values occur at the extremes of the passband.

The latter presents a truncated response and, hence, the input signal cannot be reconstructed through inverse transformation.

In another article [14], he states that the bandwidth that a CT processor is capable of analyzing is limited by the chirp filter bandwidth ($\Delta\omega_f$) and that the number of resolution cells within this bandwidth is equal to the filter TBWP. Hence, he concludes that the maximum frequency resolution attainable by the CT processor is given by

$$\omega_{r,max} = \frac{\Delta\omega_f}{TBWP} = \frac{\cancel{\Delta\omega_f}}{\cancel{\Delta\omega_f} T_f} = \frac{1}{T_f}. \tag{2.12}$$

Atzeni, Manes, and Masotti were other researchers interested in the real-time Fourier transform using SAW devices. They again refer to the relation between electronic chirp transformation and spatial transformation in optics, introduced by Mertz in 1965 [15], and explain that for this reason, the chirp transformation is also referred to as *Fresnel transformation*.

In [16], they explore the application of electronic chirp transformation in programmable signal processing, like adaptive filtering and programmable waveform generation. They suggest to filter signals by applying the chirp transform to obtain a time-domain version of its spectrum ($\mathcal{F}\{s_i(t)\} = S_i(\mu t)$, where $\mu t = \omega$), multiplying the obtained transform by a time-domain version of the desired transfer function ($\mathcal{F}\{f(t)\} = F(\mu t)$, where $\mu t = \omega$), and inverse transform the result. Fig. 2.5 depicts this filtering scheme. Fig. 2.5a illustrates the block diagram of the chirp transform (this scheme is also known as a *compressive receiver* or *microscan receiver*) and Fig. 2.5b illustrates the scheme where the spectrum of the signal is multiplied by a transfer function and inverse transformed. The compressive receiver corresponds to the scheme devised by Klauder et al. in [9] and is equal to the MCM architecture of Fig. 2.3a without the post-multiplication, which results in the transformed signal being multiplied by a factor $e^{j\mu t^2}$. This outcome is multiplied by the time-representation of a transfer function $\mathcal{F}\{f(t)\}$ and is then inverse transformed to yield the filtered signal ($s_i(t) * f(t)$).

Based on this scheme and making use of SAW chirp filters, several operations were experimentally demonstrated, like low-pass and band-pass filtering, variable delay, and differentiation. Additionally, a programmable waveform generation was demonstrated by inverse transforming a time-domain representation of the spectrum of the desired signal. This operation was accomplished by directly applying the time-domain signal representing the spectrum of the desired signal to the input of the filter shown in Fig. 2.5b.

A relevant point that the authors make explicit in their article, but related works from other researchers do not make clear, is the fact that, despite modeling the system in terms of complex signals expressed in polar form and complex operations, the experimental demonstrations realized do not represent the complex models. Indeed, (2.13), the Euler's formula, establishes a fundamental relationship between the exponential representation of a complex quantity and its trigonometric representation (cf. Table 2.2). Thus, in practice, a complex signal is composed of two real signals, one representing the real part of the complex signal and the other, the imaginary part. A complex-by-complex multiplication is constituted by four real-by-real multiplications and two addition operations between real quantities, while a complex convolution (complex filter) requires four real convolutions (real filters) and two addition operations between real quantities (cf. [17]). Using a single real multiplier and filter to simplify the required hardware implies that

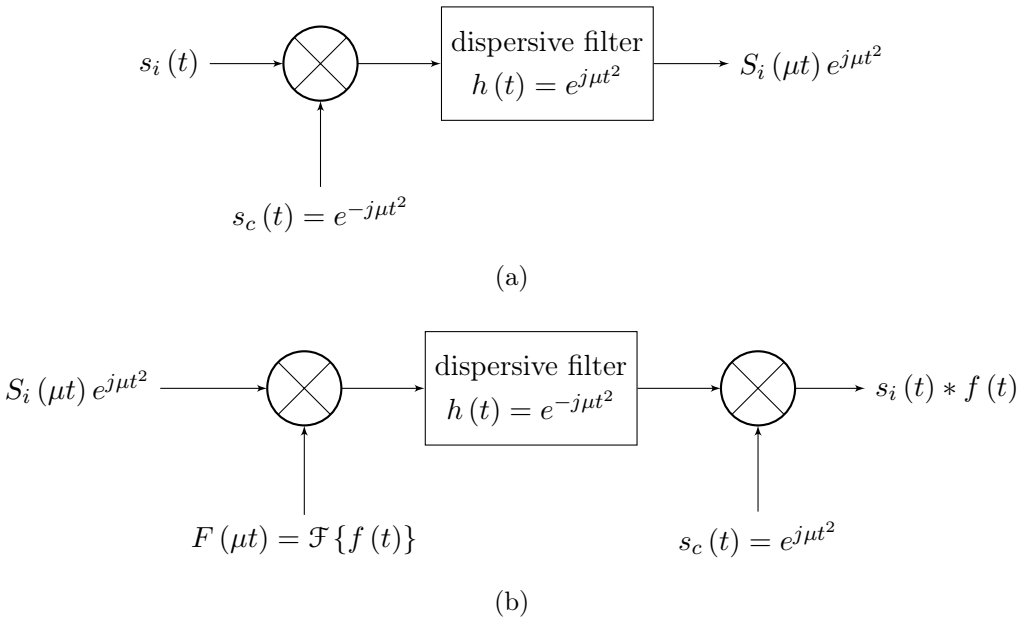

Figure 2.5 – Scheme of adaptive filtering: (a) obtaining signal spectrum by chirp transformation (compressive/microscan receiver), and (b) multiplication of signal spectrum and transfer function, and inverse chirp transformation.

Table 2.2 – Different forms of representation of a complex value.

Notation name	Expression
Rectangular (or cartesian) form	$c = a + jb$
Trigonometric form	$c = M\left[\cos(\phi) + j\sin(\phi)\right]$
Polar (or exponential) form	$c = Me^{j\phi}$
Magnitude-angle form	$c = M\angle\phi$

the implemented system is a particular case of the more general complex system.

$$e^{\pm j\phi} = \cos(\phi) \pm j\sin(\phi) \tag{2.13}$$

Beyond limiting the operations that the system can perform, the simplification of the required hardware causes much confusion when the system being analyzed is modeled in a higher level of abstraction, with complex signals and complex operations, as is often the case. One confusion, related to the way chirp signals are represented, is mentioned at the end of Section A.2.

2.1.1 Discrete Fourier Transform

SAW filters were also used in the design of discrete-time systems, like in [18], where a high-speed 32-point discrete Fourier transform (DFT) hardware based on the chirp Z-transform (CZT) algorithm was designed and applied to beamforming on data from a hydrophone array. The author claim that the CZT algorithm takes advantage of the transversal structure of the SAW filter to calculate the DFT of a signal of length N in a time proportional to N, the transform length, whilst the fast Fourier transform (FFT) algorithm performs the same operation in a time

proportional to $N \log_2(N)$. At a sample rate of 5 MHz, the designed system could compute the 32-point DFT in 6.4 µs.

The scheme of the system, named a *SAW CZT processor*, is shown in Fig. 2.6. The input signal is assumed to be at baseband in a sampled format. For this, a sample-and-hold (SH) is used to sample the real and imaginary parts of the complex input signal. The two SAW devices are functionally used in different ways. The SAW convolver constitutes a $2N-1$ point complex-valued chirp filter for real/imaginary input and output pairs, while the SAW ROM is used as a read-only memory to generate a real/imaginary pair of N-point discrete chirp sampled waveforms at a carrier frequency (29 MHz in the mentioned beamforming application) for use in pre- and post-multipliers. The complex multiplication is performed in double-balanced RF mixers, with products being summed (or subtracted) in transformer-coupled RF summers. The resulting complex-valued product is a pair of sampled-analog sequences on the 29 MHz carrier, suitable for direct input into the SAW filter.

Fig. 2.6 does not present a post-multiplier (after the complex SAW filter) and hence, can be used if only the squared-magnitudes of the DFT coefficients are desired (as a compressive receiver). Squaring is performed via double-balanced RF mixers, with a low-pass filter being used to pass only difference frequencies from the sum of mixer outputs. The use of a post-multiplier is necessary when amplitude and phase information is required.

The periodic convolution required by the CZT algorithm can be realized through at least three schemes, as depicted in Fig. 2.7. The scheme of Fig. 2.7a turns out to be impractical when employing SAW devices, since the acousto-electrical transducers are extremely lossy, and the recirculation of the signal would cause an unacceptable degradation. The scheme used in the application was then that of Fig. 2.7b, the sole that does not require recirculation of the data. This scheme is limited to a maximum duty cycle of 50 % because of the required load/unload time during which periodic convolution is not taking place. However, if two CZT filters are used side-by-side, a 100 % duty cycle can be obtained if continuous throughput is required.

Another 256-point SAW CZT processor was also designed using a different technique to implement the filter (see Fig. 2.8). The filter impulse response was segmented so that adjacent acoustic channels on a single substrate, fed by appropriately delayed replicas of the input signal, could be used to form the equivalent of a single tapped delay line structure with a large TBWP. The scheme of Fig. 2.7c was used since the scheme of Fig. 2.7b became infeasible for such a long transform length. A digital delay line with four taps spaced at 64-samples intervals was used to

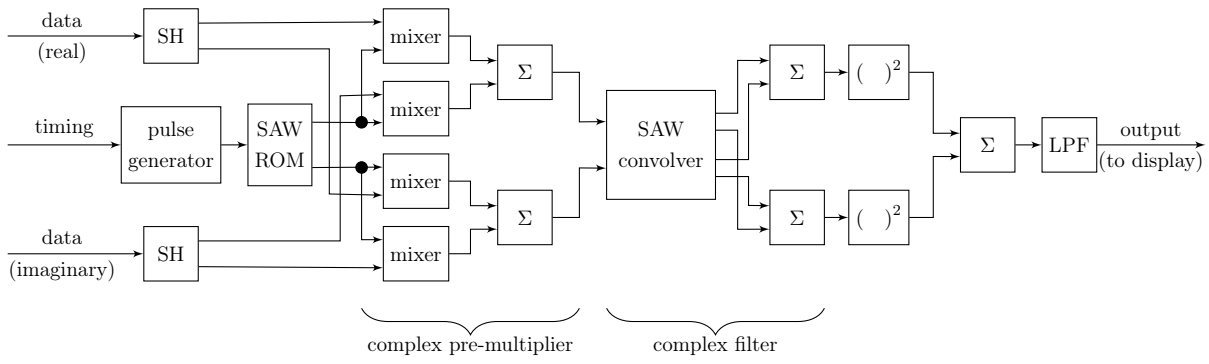

Figure 2.6 – Scheme of the SAW CZT processor designed in [18] (adapted).

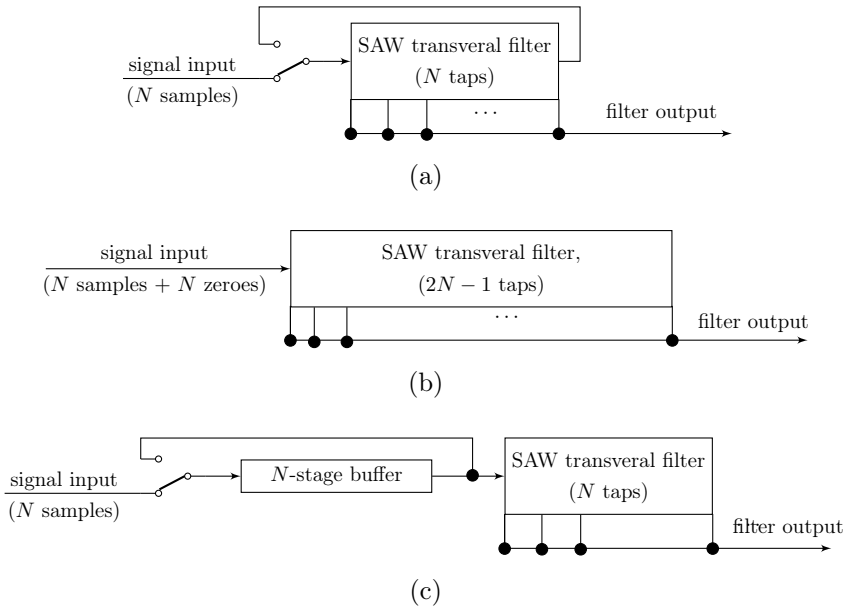

Figure 2.7 – Alternative schemes for the implementation of the periodic convolution operation (from [18]).

obtain the appropriately-delayed inputs for the four acoustic channels. Under this configuration, the maximum duty cycle the system can achieve is 80 %, due to the relatively short (64 sample intervals) load/unload time. This new system can compute the 256-point DFT in 51.2 µs.

Real-time network analysis was another application that made use of discrete-time systems employing SAW chirp filters. In [19, 20], Jack, Grant, and Collins report the realization of an IF network analyzer making use of a *real-time SAW DFT signal processor*.

In this system, illustrated in Fig. 2.9, the response resulting from the excitation of a network under test by an intermediate frequency (IF) pulse train of period 1.25 µs, corresponding to a line spectrum spaced at 800 kHz, is pre-multiplied by a chirp and subsequently convolved in a chirp filter. The amplitude response of the network under test is obtained by envelope detecting and sampling the convolved output. The phase characteristic is found after limiting, post-multiplying

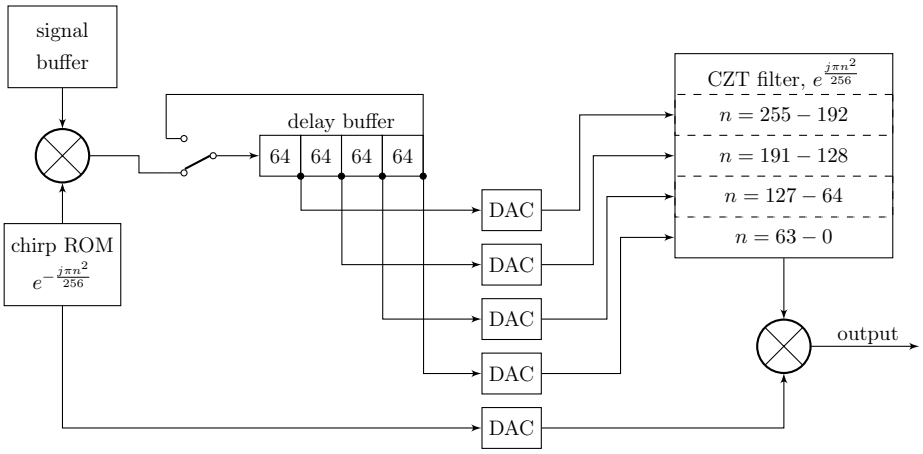

Figure 2.8 – Scheme of the SAW CZT processor designed in [18] implementing a segmented filter response (adapted).

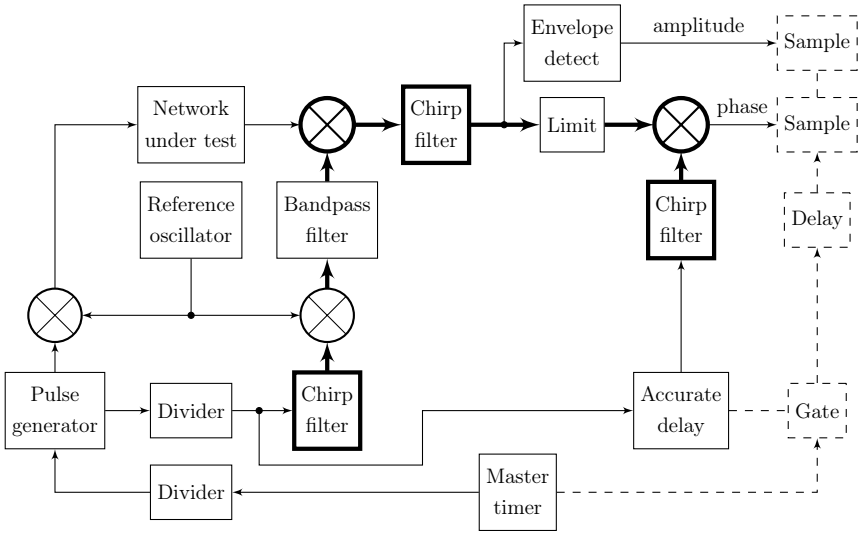

Figure 2.9 – Block diagram of the real-time network analyzer employing SAW DFT processor of [19, 20].

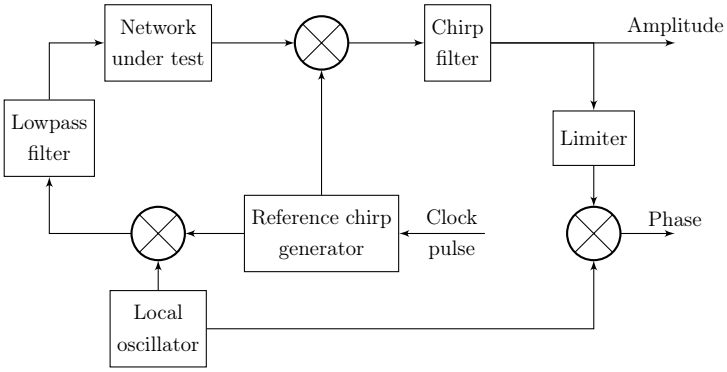

Figure 2.10 – Block diagram of the real-time network analyzer using the dual analog chirp transform (CMC scheme) of [21].

by a chirp, and sampling the convolved output.

The Fourier transform processor, outlined in bold in Fig. 2.9, corresponds to the MCM algorithm of Fig. 2.3a. The pre-multiplying and post-multiplying chirps are generated by exciting SAW chirp filters with impulses of 8 ns pulse length.

The network analyzer operated over a 12.5 MHz band centered at 145 MHz and presented a resolution of 800 kHz. It was used to characterize the transfer function of two filters. The measurements were compared with that of a commercial network analyzer and demonstrated to be correct.

In [21], Atzeni, Manes, and Masotti report the implementation of a network analyzer similar to that described by Jack et al. in [19, 20], but this time using the CMC scheme (cf. Fig. 2.3b), that they call the *dual analog chirp transform*. They were also able to eliminate the first chirp filter of the CMC scheme by impulsing the network under test with a chirp. The same chirp signal is used in the subsequent multiplication, resulting in the simplified configuration of Fig. 2.10.

In their experiments, unlike Jack et al., they used a continuous-time actively generated chirp[5]

[5]For some explanation about the generation of chirp signals, please refer to Section A.3.

swept from 44.9 MHz to 61.1 MHz in 180 µs. The SAW chirp filter had a group delay swing of 30 µs and a bandwidth of 2.7 MHz centered at 9 MHz. The system was, therefore, capable of analyzing a bandwidth of 13.5 MHz centered at 44 MHz with a frequency resolution of 33 kHz. The maximum time-bandwidth product of the network analyzer was thus 405.

In a joint work [13], the groups of Jack and Atzeni compare the performances of the two real-time network analyzers reported previously by each group [19–21] with that of a SAW sliding chirp transform processor and of a conventional network analyzer.

2.1.2 Applications

Several works focus on the applications of Fourier transformers employing SAW devices. For instance, Jack et al. produced a revision work on the theory, design, and applications of SAW Fourier transform processors [5], where they cite several applications of such systems. They divide the applications into two groups, one that requires only one SAW processor, and another that requires more than one processor. Among the applications that require only one processor, they mention real-time spectrum analysis, real-time network analysis, beamforming, and waveform synthesis (where the processor performs the inverse transform). Among the applications that require more than one processor, they cite variable frequency filtering, real-time SAW cepstrum analysis[6], programmable correlation, and variable delay.

In [22, 23], Eng et al. study the use of chirp transform processors for time compression multiplexing of multiple television signals in satellite channels as an alternative approach to the conventional frequency-division multiplexing approach. They found that the technique introduced excessive distortion to the signal, but this distortion could be controlled to a negligible level by proper design of the chirp signal.

In [24], D'Addario studies the use of chirp transform spectrometers (particularly, compressive receivers) for millimeter-wave spectroscopy. He considers applying the spectrometer as a radiotelescope backend by defining reasonable specifications and developing the block diagram of different configurations that can potentially meet the requirements. He concludes that, at that moment (end of the eighties), the use of chirp transform spectrometers was not recommended, as his study showed that the available devices were only marginally able to achieve the required bandwidth and that the high-speed digital processing required would still be formidable. Besides, acousto-optical spectrometers showed feasibility in approaching the required bandwidth (in the order of 1 GHz) and were already being used on several radiotelescopes, apparently with good results.

SAW-based chirp Fourier transform for satellite onboard signal processing was the research topic in [25] and [26]. In [25], the authors were interested in using the chirp Fourier transform to realize multicarrier demodulators (MCDs) to be used in a FDMA/TDM architecture[7]. In [26], two applications were described, an onboard MCD for 9.6 kbps quadrature phase-shift keying (QPSK) carriers, and a processor for filtering, routing, and beam steering for flexible transparent repeaters.

[6] Cepstrum analysis allows the investigation of periodic effects in the frequency domain associated with time repetitive or "echo" waveforms [5].

[7] An architecture consisting of an frequency division multiple access (FDMA) uplink and a time division multiplexed (TDM) downlink.

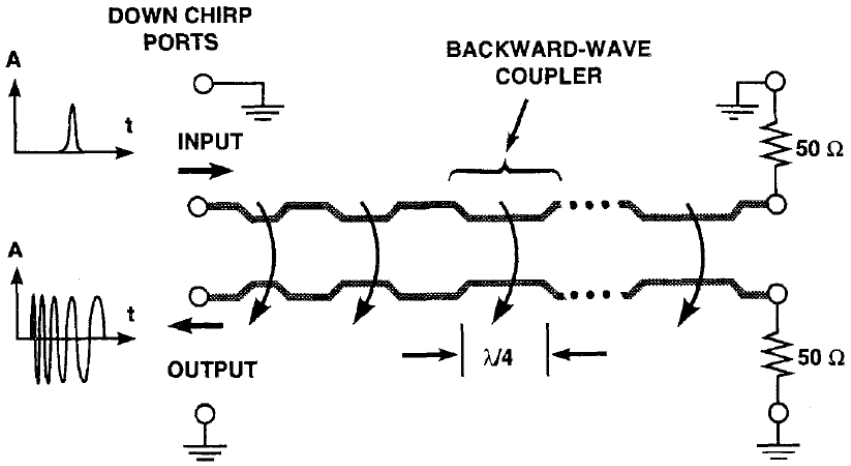

Figure 2.11 – Illustrative scheme of a superconductive device with a down-chirp impulse response (from [31]).

2.1.3 Alternatives to SAW Devices

SAW devices are by far the most employed devices for analog signal processing (ASP) due to their high TBWP (large group delay swing and relatively wide bandwidth), compact size, and low mass. However, other devices exist that can also be designed to present a linear group delay characteristic and, thus, be used in ASP applications, in particular, real-time Fourier transformation.

One of these alternative devices employs magnetostatic wave (MSW) technology. These devices use ferrimagnetic films, such as liquid phase epitaxial (LPE) yttrium iron garnet (YIG) films, and present smaller group delay swing (in the order of hundreds of nanoseconds) than SAW devices. However, they have wider bandwidths and can operate at higher frequencies (several gigahertz) [27, 28]. As for drawbacks, MSW devices require magnets, and its fabrication process is intricate.

In the eighties and nineties, the Analog Device Technology Group on the Lincoln Laboratory of the Massachusetts Institute of Technology (MIT) performed research on the use of superconductive devices for ASP. Several chirp filters were developed, and some compressive receivers employing such devices were reported in [1, 29–32]. Superconductive devices are four-port networks in which a pair of superconductive striplines separated by a variable distance are coupled by a cascade array of backward-wave couplers. Fig. 2.11 illustrates this device, where a portion of the energy propagating in the input line from the input port is transferred to a wave propagating to the other sense in the adjacent line, towards the output port. This mode of operation causes superconductive devices to be classified as reflection-type. The devices previously mentioned are classified as transmission-type. Compared to SAW, superconductive devices present higher bandwidths, but much smaller group delay swing (on the order of several dozen nanoseconds). Consequently, their TBWP is also much smaller. As advantages, superconductive devices present low insertion loss and are capable of operating at high frequencies (several gigahertz), but require cryogenic temperatures and are complex to fabricate.

More recently, artificial transmission lines employing distributed structures on conventional microwave technologies have been studied and developed for ASP applications. In [33], a com-

posite right/left-handed (CRLH) transmission line (TL) implemented on a Rogers Duroid 5870 substrate was employed in the realization of a compressive receiver. An integrated implementation of an active dual composite right-left handed (D-CRLH) dispersive delay line (DDL) using a distributed structure was designed in a gallium nitride (GaN) monolithic microwave integrated circuit (MMIC) technology and reported in [34]. A real-time Fourier transformer was designed using an engineered C-section all-pass network in [35], and an inverse Fourier transformer in [36]. Integrated active delay lines were first demonstrated in [37–39], implemented using a 0.13 µm complementary metal-oxide-semiconductor (CMOS) process.

Chirped microstrips (also known as chirped electromagnetic bandgaps (CEBGs), or nonuniform transmission lines (NUTLs)), a reflection-type structure, can also be designed to present a linear group delay. It seems that Laso et al. [40, 41] were the first to report the realization of a chirped microstrip where the energy spectral density of the input signal was given by the average output power reflected from the device. In [42], Schwartz et al. demonstrate a fully electronic system for the time-magnification (or time-stretching) of ultra-wideband (UWB) signals. The system employs three CEBGs fabricated on a Coorstek ADS-96R substrate and achieves a time-magnification factor of five when operating on a 0.6 ns time-windowed input signal with up to 8 GHz bandwidth. On [43], Ma et al. employ nonuniform coupled-line phasers constructed on a Rogers RO3010 substrate, and with structures resembling that of Fig. 2.11, to perform real-time Fourier transformation and inverse Fourier transformation. In [44, 45], Xiang et al. demonstrate a reconfigurable integrated DDL in 0.13 µm CMOS process capable of real-time spectrum analysis. The DDL presents a transversal filter structure, also resembling that of Fig. 2.11, but presenting tap gains.

Several photonic and optoelectronic devices can be designed to present a linear group delay characteristic. In [46], Azaña and Muriel present a method for the design of linearly chirped fiber grating (LCFG) and linearly chirped intermodal coupler (LCIC) devices that work as real-time spectrum analyzers. LCFG and LCIC are, respectively, reflection- and transmission-type devices. An LCFG device with a linear group delay, 1 ns group delay swing, and 1.2 THz bandwidth centered at 193.1 THz was designed and simulated using the proposed method. In [47, 48], Zhang and Yao use a linearly chirped fiber Bragg grating (LCFBG) to precisely time reverse a microwave broadband signal. This device was fabricated in a single-mode fiber with a length of 1 m, and presented low insertion loss, a group delay swing of 10 ns, and a pretty linear group delay characteristic.

The use of rare-earth ion doped crystals (REIC) with absorption profiles tailored by spectral hole burning (SHB) has been studied recently as a way to achieve very high TBWP [49, 50]. In [49], the absorption profile of erbium ions embedded in a crystalline lattice of yttrium orthosilicate (Y_2SiO_5) was tailored through spectral hole burning to achieve an increase of five orders of magnitude in group delay swing from that of kilometer-long dispersive fibers. An experiment was set up to demonstrate the time reversal of a 6 µs-long signal. For this, the 0.005% Er^{3+}:Y_2SiO_5 crystal was cooled at 1.7 K in a liquid helium cryostat. In [50], a 0.5% thulium-doped yttrium aluminum garnet (YAG) cristal (Tm^{3+}:$Y_3Al_5O_{12}$) cooled at 3 K by a closed-cycle cryostat was used in an experimental demonstration of a multi-gigahertz bandwidth RF spectrum analyzer exhibiting a resolution better than 20 MHz.

Table 2.3 summarizes the characteristics of the different device technologies that can be

employed in real-time Fourier transform systems.

Table 2.3 – Comparison between different chirp filter technologies and their mode of operation (reflection/transmission) (adapted from [33]) (some typical values ranges are presented to give an idea of the order of magnitude).

Technology	Advantages	Drawbacks
SAW (transmission)	• large group delay swing ($\geqslant 10\,\mu s$) • high TBWP (> 1000) • compact size • amplitude weighting	• high insertion loss ($> 30\,dB$ for RAC) • small bandwidths ($< 1\,GHz$) • low operating frequency ($< 1.5\,GHz$)
MSW (transmission)	• high operating frequency ($> 1\,GHz$) • moderate bandwidths ($< 1\,GHz$) • moderate group delay swing ($< 1\,\mu s$) • moderate TBWP	• high insertion loss ($> 30\,dB$) • requires magnet • complex to fabricate
Superconductive (reflection)	• low insertion loss • high operating frequency • large bandwidths ($> 1\,GHz$) • moderate TBWP • amplitude weighting	• small group delay swing ($< 100\,ns$) • requires cryogenics temperatures • complex to fabricate • size-dependent bandwidth
Transmission line (transmission)	• low insertion loss (or gain) • high operating frequency • large bandwidths ($> 1\,GHz$) • simple to fabricate	• small group delay swing ($< 10\,ns$) • small TBWP
Chirped microstrip (reflection)	• low insertion loss (or gain) • high operating frequency • large bandwidths • simple to fabricate	• small group delay swing • size-dependent bandwidth • suitable only for energy or power spectral density estimation
LCFBG (reflection type)	• low insertion loss • high operating frequency • large bandwidths	• small group delay swing
REIC with absorption profile tailored by SHB	• very high operating frequency • very large bandwidths • high TBWP	• requires cryogenics temperatures • complex to fabricate

2.2 Radio Astronomy Spectrometers

In radio astronomy, the power spectrum is of vital importance in the analysis of physical phenomena and the study of celestial bodies. In this domain, the systems that allow the evaluation of the power spectrum are called *spectrometers* (or, more specifically, *radio spectrometers*, when they process radio signals). The CT-based systems mentioned previously constitute the core of a type of radio astronomy spectrometer, namely, a chirp transform spectrometer (CTS). Despite their specialized use, it is worth briefly discussing here the different types of radio spectrometers that exist, since the Fourier transform is the main operation performed by these instruments. There exist five basic types of spectrometers commonly used in radio astronomy.

- Chirp transform spectrometers (CTSs)
- Filterbank spectrometers
- Autocorrelation spectrometers
- Acousto-optical spectrometers (AOSs)
- FFT spectrometers

Each type of spectrometer presents some strong and weak points when compared to the other types. The spectrometers used in radio astronomy are generally composed of discrete circuits (not ICs), even those for airborne/space applications, and have strict requirements in terms of stability, reliability, bandwidth, and spectral resolution.

Filterbank spectrometers are the simplest type of radio astronomy spectrometers. They are constituted by a bank of frequency contiguous IF filter channels. The IF channels usually include an amplifier to overcome signal splitting and filter transmission losses. Individual IF gain controls allow the overall spectrometer magnitude frequency response to be equalized [51].

Autocorrelation spectrometers (also known as digital autocorrelators or, simply, autocorrelators) have been used since the early sixties [52] and are constituted by digital autocorrelators [53]. They perform a one-bit or two-bit quantization of the time signal, being the use of more than two bits of quantization impractical, due to the high complexity of the circuits.

Acousto-optical spectrometers have been used since the early eighties [52]. They are based on a technique combining acoustic bending of a collimated coherent light beam by a Bragg cell, followed by detection by a sensitive array of photodetectors [53]. The bandwidth of an AOS is limited by the bandwidth of the Bragg cell (typically, 1.5 GHz to 2 GHz). AOSs are generally low power but commonly present a high mass due to the mechanical requiriments of their optical parts. Early AOSs often presented stability issues, that were solved after more sophisticated optical, electrical, mechanical, and thermal designs [52].

More recently, the technology scaling trend of integrated circuit (IC) technology enabled the realization of FFT spectrometers with performances surpassing those of other types of spectrometers. They are cheap, lightweight, compact, extremely flexible (reprogrammable), and present low power consumption.

According to these characteristics, filterbank spectrometers are not practical when more than a few frequency channels are required. AOSs are generally used in broadband applications,

Table 2.4 – Characteristics and performances of chirp transform spectrometers developed at the Max-Planck-Institut for Solar System Research at different dates (adapted from [56]).

	1983	1984	1985	1987	1991	1992	1997	2003	2005
Input center frequency (MHz)	180	300	1350	300	300	1350	1350	3000	2100
Input bandwidth (MHz)	25	22	40	40	40	40	178	400	400
Spectral resolution (kHz)	500	150	50	50	22	50	43	100	100
Passband ripple (dB)	3	6	1	1	1	1	2	2	1
Dynamic range (dB)	18	27	26	15	30	30	29	25	40
Frequency linearity (kHz)	20	8	1	1	1	1	2	2	0.5
Frequency scale stability (kHz)	50	1	5	2	2	2	5	10	5
Power consumption (W)	420	520	530	430	50	30	$\leqslant 15$	5	$\geqslant 10$
Mass (kg)	22	20	20	25	10	10	2.3	1	$\leqslant 10$

and autocorrelators in applications that require high resolution. Compared to CTSs and FFT spectrometers, the other systems generally present some disadvantages in terms of size, mass, power consumption, or mechanical and electrical stability [54, 55].

The Max-Planck-Institut for Solar System Research in Katlenburg-Lindau, Germany, is involved in the development of chirp transform spectrometers employing SAW devices since the eighties, having reported several practical realizations (cf. Table 2.4), some of them being in use in scientific instruments like the German REceiver for Astronomy at Terahertz frequencies (GREAT) instrument onboard the Stratospheric Observatory For Infrared Astronomy (SOFIA), and the Microwave Instrument for Rosetta Orbiter (MIRO). All the CTSs developed there are based on the sliding chirp transform (the group delay swing of the chirp filter is half the sweep time of the chirp signal in the pre-multiplier) and present roughly the same architecture [52, 54, 55, 57–62].

Fig. 2.12 shows the block diagram of the lastest CTS developed at the Max-Planck-Institut for Solar System Research. The architecture is composed of two identical paths, each one operating at a 50 % duty cycle in a push-pull arrangement to attain a 100 % duty cycle. This architecture presents an active generation scheme for the pre-multipling chirp signal. An adaptive direct digital synthesis (DDS) processor generates a chirp signal with characteristics matching those of the chirp filter (SAW device) [60]. The architecture does not multiply the output of the chirp filter by a post-multiplying chirp and, for this reason, is characterized as a compressive receiver, being only suitable for power spectra analysis. This block diagram also shows the several amplifiers needed to amplify the signal after each filtering operation, notably after the SAW devices, that present a high insertion loss.

2.3 Analog Implementation of the Fast Fourier Transform

Recently, some works have reported analog discrete-time implementations of the FFT aimed at reducing the burden of analog-to-digital converters (ADCs) in software-defined radios (SDRs),

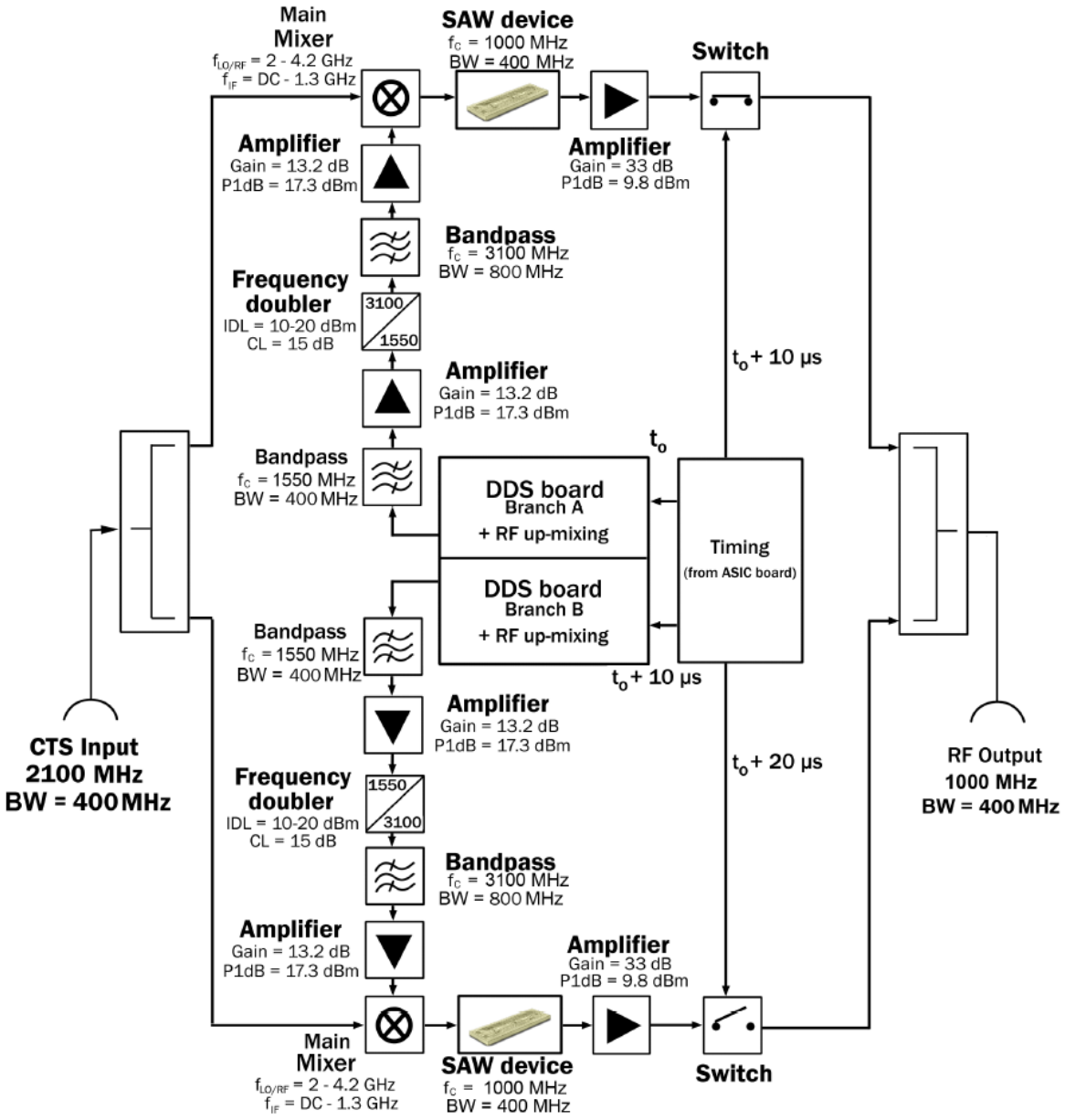

Figure 2.12 – Block diagram of the latest CTS developed at the Max-Planck-Institut for Solar System Research (from [62]).

that need to operate at frequencies up to 5 GHz. The idea is to interpose a preprocessing circuit between the antenna and the ADC to precondition the radio signal. The preprocessing operations consist mainly in sampling and transforming the signal from the time to the frequency domain.

In [63–65], Rivet et al. introduce what they call a *sampled analog signal processor (SASP)*, that samples a signal and recovers its spectrum, to subsequently perform downconversion and channel presorting in the frequency domain. They developed a demonstrator implementing a 64-point radix-4 DFT (FFT butterfly) in a 65 nm CMOS technology. The architecture of this system is shown in Fig. 2.13, and operates by first sampling the input signal through a track and hold and windowing the sampled signal. The sampling frequency (f_s) determines the FFT processing frequency ($64f_s$), the spectrum range (from 0 Hz to $\frac{f_s}{2}$), and the spectral resolution ($\frac{f_s}{64}$). The voltage samples are then sent to the FFT butterfly circuit, which is composed of three

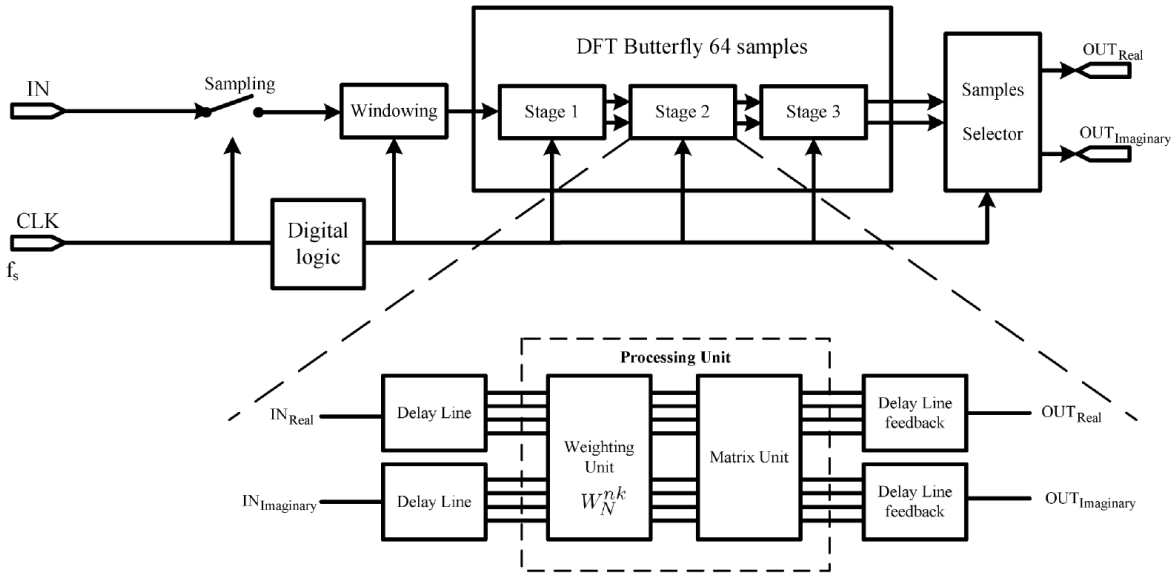

Figure 2.13 – Block diagram of the sampled analog signal processor (SASP) system (from [65]).

stages. Each stage performs delay, addition, and weighting operations on the voltage samples. Delay operation is carried out by storing samples on capacitors, while addition and weighting operations are carried out in the current domain, via a voltage/current/voltage conversion. The weighting and the matrix units operate on a four by four set of samples. A digital logic circuit synchronizes and coordinates all the blocks. Their demonstrator occupies an area of 1200 µm by 1200 µm (with pads) and consumes 389 mW when operating at 1.2 GHz.

Another analog implementation of the FFT was reported by Sadhu et al. in [66, 67]. Their system, named *CRAFT*, from *charge reuse analog Fourier transform*, is based on a 16-point radix-2 FFT (see Fig. 2.14a) and aims to function as an RF front-end channelizer for SDRs. It is built upon passive switched capacitors on a 65 nm technology. The charge reuse analog Fourier transform (CRAFT) core (FFT butterfly) occupies an area of 300 µm by 480 µm, while the complete system, with sampling circuit, state machines, analog latches and multiplexer (cf. Fig. 2.14b), occupies an area of roughly 900 µm by 480 µm (without pads). The system can work with input rates up to 5 GS/s, consuming only 3.8 mW (12.2 pJ/conv.), and presenting a corrected (calibrated) signal-to-noise and distortion ratio (SNDR) of 47 dB. Due to its charge reuse scheme, the CRAFT system presents a power consumption 28 times better than the SASP system of [63–65]. However, the authors recognize the system complexity and susceptibility to circuit non-idealities, like noise, matching, and non-linearities, which calls for a careful layout. The complexity of the layout can be appraised based on the block-level scheme of the CRAFT layout floorplan shown in Fig. 2.14b. Moreover, as an additional complicating factor, circuit simulators and technology models lack support for simulating switching circuit noise, charge-injection, and charge accumulation.

A fully integrated hybrid filter bank ADC based on an analog 8-point radix-2 FFT with a rectangular window, similar to that of Sadhu [66, 67], is reported by Shin et al. in [68]. Compared to the work of Sadhu, Shin modified the complex multiplication operation to reduce the number of switches and, consequently, reduce the dynamic power consumption, the area, and the wire-

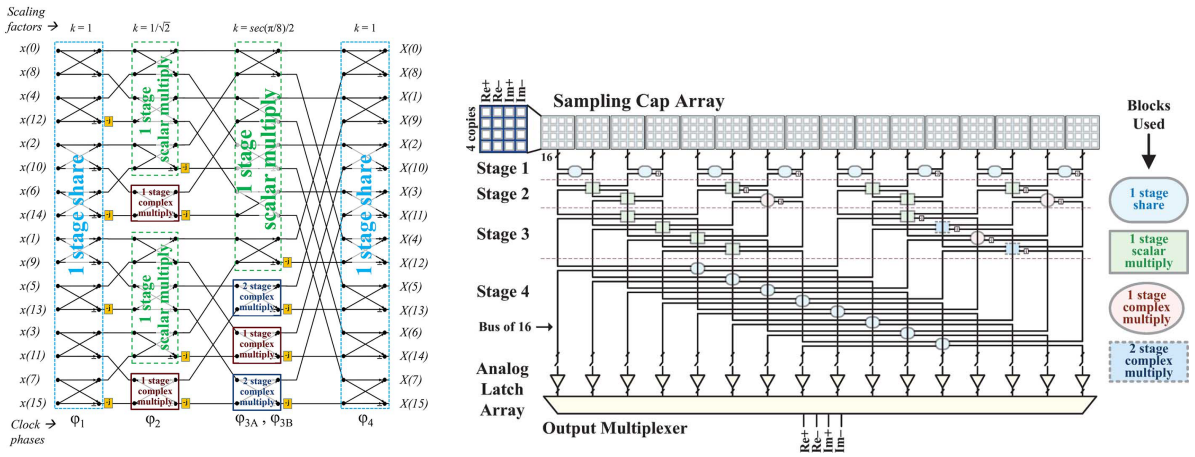

(a) (b)

Figure 2.14 – (a) 16-point radix-2 FFT butterfly scheme implemented by CRAFT, and (b) block-level scheme of the CRAFT layout floorplan showing the different blocks used in each stage and the intricate routing (from [67]).

routing complexity. All this at the expense of one additional clock period. The hybrid filter bank was implemented in a 40 nm CMOS general purpose technology and showed 26.6 dBm of third order input intercept point (IIP3), and power consumption of 4.8 mW.

In [69], Shin presents a different analog FFT system. This time he describes a 4-point polyphase-FFT filter bank implemented in a 65 nm CMOS general purpose technology. The prototype occupies an area of 0.6 mm by 0.3 mm, operating up to 1 GHz, with an IIP3 of 25.3 dBm, and power consumption of 4.33 mW per channel.

A disadvantage of discrete-time systems is that the power consumption is directly linked to the sampling frequency. Thus, the higher the sampling frequency, the higher the power consumption [65]. The migration of modern communication technologies (e.g., 5G and Wi-Fi standard IEEE 802.11ad) to higher frequency bands (above 24 GHz), to benefit from a less crowded spectrum and higher bandwidths, poses a significant challenge to portable discrete-time systems in terms of power consumption.

2.4 Selected Research Direction

Based on the literature review, it is possible to distinguish two primary approaches used to implement real-time analog Fourier transformers, one consisting of the implementation of the fast Fourier transform (FFT) through sampled circuits, and the other comprising the implementation of the chirp transform. This latter approach allows for both discrete-time and continuous-time implementations.

Analog Fourier transformers implementing the fast Fourier transform have been proposed in the context of SDR to identify the signal band containing the information to allow reducing the bandwidth of the signal to be converted, potentially alleviating the requirements imposed on the ADC. Architectures taking this approach are usually able to analyze bandwidths of a few gigahertz, and the spectral resolution is limited by the sampling rate employed. This approach often leads to complex circuits where power consumption increases with an increasing system

operating frequency.

To date, all Fourier transformers that implement the chirp transform have been implemented in technologies that do not lend themselves to integration or are challenging to integrate, such as SAW, superconductive, discrete microwave and optoelectronic technologies. Continuous-time implementations have a continuous spectrum where the spectrum resolution is limited by the time-bandwidth product of the chirp filters employed.

In this context, it was decided in this thesis work to explore an implementation in IC technology based on the continuous-time approach, looking for a versatile, area-efficient, low-power, and ultra-wideband solution.

Chapter 3

Real-Time Analog Chirp Fourier Transformer

Beyond the established method of obtaining the spectrum of a signal by means of a digital circuit implementing the fast Fourier transform (FFT) algorithm, the study of the literature allowed us to identify two primary forms of realizing electronic analog systems that perform the Fourier transform in real-time: the analog implementation of the FFT algorithm by means of discrete-time circuits [63–69], and the implementation of the multiply-convolve-multiply (MCM) or convolve-multiply-convolve (CMC) algorithms[1] in discrete-time or continuous-time [5, 12, 16].

After analysis of the limitations due to the recurrent simplification adopted when implementing the MCM and the CMC architectures, it is proposed here a two-path architecture, based on the MCM arrangement, leading to an accurate spectrum with phase information, as in the theoretical case. Some reasons that led us to choose the MCM algorithm implementation instead of the FFT algorithm implementation were that,

- the MCM algorithm enables the analysis of an arbitrary spectrum range, while the FFT algorithm is constrained to a spectrum range starting at 0 Hz;
- the MCM algorithm allows for a continuous-time implementation, in addition to a discrete-time implementation, while the FFT algorithm is intrinsically a discrete-time algorithm.

A continuous-time implementation presents some appealing characteristics. It presents the potential to attain higher frequencies with less power consumption. As it is dissociated from a clock signal, its power consumption does not necessarily increase as the operating frequency increases. Moreover, continuous-time systems are free from problems inherent to discrete-time systems, like charge injection and clock feedthrough. Regarding circuit simulations, continuous-time circuits are more straightforward to simulate than discrete-time circuits, and their simulation results are also easier to interpret.

[1] These algorithms are said to implement the *chirp transform* (or *chirp Fourier transform*), that is, essentially, the Fourier transform obtained through multiplications and convolutions with exponential functions presenting a quadratic argument.

3.1 Limitations of Common Implementations of the MCM Arrangement

In state of the art, the MCM configuration is usually implemented via a sole chirp filter and a real chirp signal generated by a voltage controlled oscillator (VCO) [3, 58] or by impulsing another chirp filter [33, 54]. This arrangement does not satisfy the complex nature of the MCM algorithm, resulting in the loss of information about the phase spectrum.

Fig. 3.1a illustrates the magnitude spectrum of a signal composed by the superposition of three sinusoids with the same amplitude and different frequencies (1 GHz, 2 GHz, and 2.5 GHz) obtained via the MCM arrangement[2]. The spectrum is normalized to the higher frequency component. Fig. 3.1b illustrates the magnitude spectrum of the same signal obtained when only the real parts of the complex chirp filter and signals constituting the MCM arrangement are considered (the same normalization factor applied in Fig. 3.1a is applied in Fig. 3.1b). It can be seen that the magnitudes of the spectral components are half the correct magnitudes and that a "noisy" floor appears, which can give rise to the detection of false spectral components.

The works in the literature generally implement the MCM arrangement by using down-chirp signals and filters with up-chirp impulse responses (or vice-versa) and boasts that their systems perform matched filtering. However, as Fig. 3.2 illustrates, besides being "noisy", the obtained spectrum is also reversed.

To correctly implement the MCM configuration and, consequently, obtain an accurate spectrum, it is proposed in what follows an architecture with two signal paths in quadrature, one representing the real part of signals, and the other, the imaginary part [17].

3.2 Proposed Analog Chirp Fourier Transformer

The architecture of the analog chirp Fourier transformer proposed here is based on the MCM algorithm but contrasts with previous works by taking on account the imaginary part of the complex operation performed by the algorithm, thus allowing the obtention of an accurate spectrum. The proposed architecture is shown in the bottom part of Fig. 3.3. It presents two signal paths, for the real and imaginary parts of complex signals, according to the principles detailed in [17]. The diagram at the top of the figure presents the operations realized by the system in a simplified manner, according to an exponential notation. In the figure, s_i is an input signal, s_n is a complex sinusoid[3], given by (3.1), s_c is a complex chirp of linearly increasing frequency (up-chirp), defined by (3.2), and $h(t)$ is the impulse response of a complex filter, stated as the complex conjugate of (3.2). Appendix A carefully defines these complex signals and deduce their analytical models.

$$s_n(t) = e^{j2\pi(f_1 t+\varphi)} = \underbrace{\cos\left[2\pi\left(f_1 t+\varphi\right)\right]}_{\mathrm{Re}\{s_n(t)\}} + j\underbrace{\sin\left[2\pi\left(f_1 t+\varphi\right)\right]}_{\mathrm{Im}\{s_n(t)\}} \tag{3.1}$$

[2]The uneven spectrum component magnitudes are due to the limited integration time of the convolution operation.

[3]The complex sinusoid is defined as $Ae^{j(\omega t+\phi)} = Ae^{j\phi}e^{j\omega t} = A\cos(\omega t+\phi) + j\sin(\omega t+\phi)$ [70].

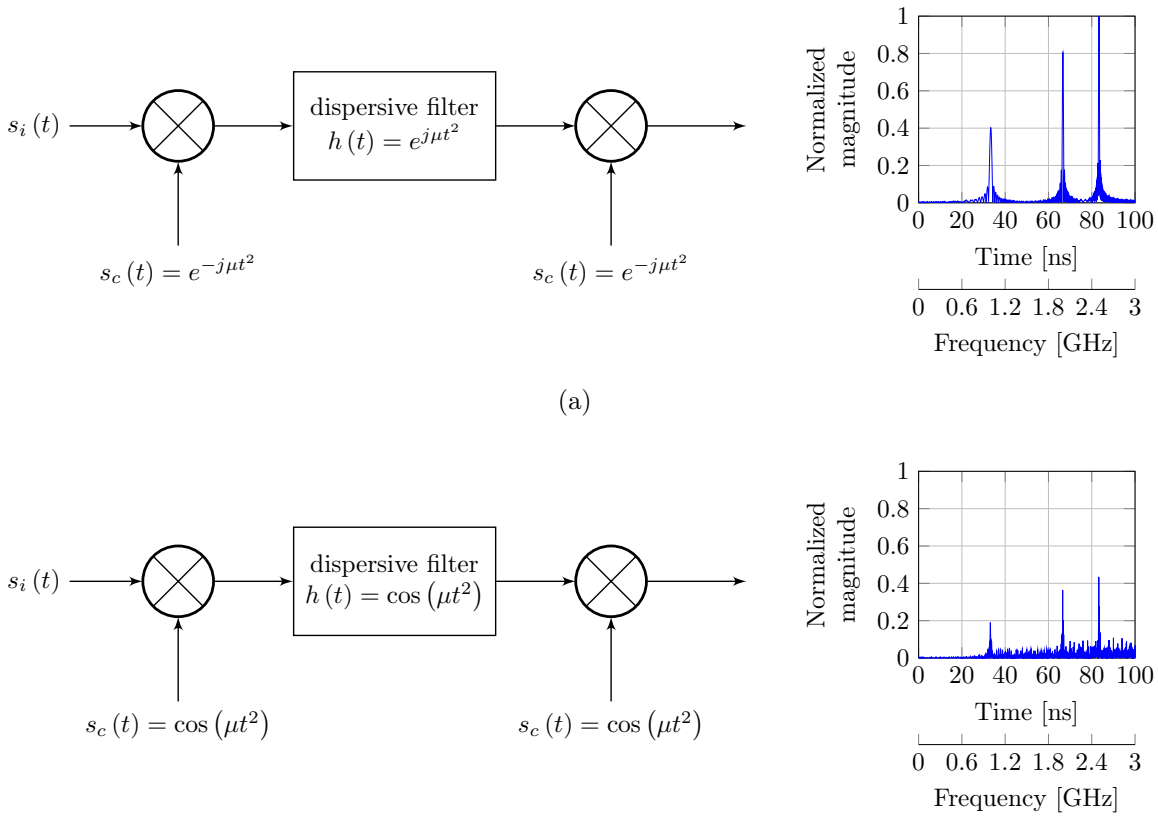

Figure 3.1 – Illustration of the magnitude spectrum of a signal composed by the superposition of three sinusoids of same amplitude and frequencies 1 GHz, 2 GHz, and 2.5 GHz obtained: (a) via the MCM arrangement, (b) via the MCM arrangement when considering only the real part of the complex signals and filter (magnitudes normalized to the higher magnitude component of Fig. 3.1a).

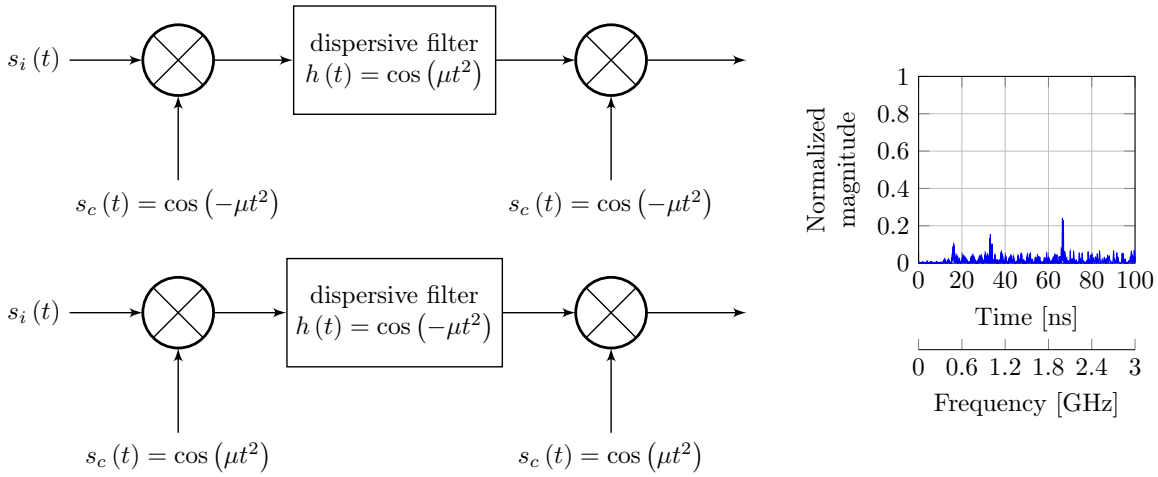

Figure 3.2 – Illustration of the magnitude spectrum of a signal composed by the superposition of three sinusoids of same amplitude and frequencies 1 GHz, 2 GHz and 2.5 GHz obtained via the MCM arrangement when considering only the real part of the complex signals and filter, as in Fig. 3.1b, but with down-chirp signal and filter with an up-chirp impulse response (and vice-versa) (magnitudes normalized to the higher magnitude component of Fig. 3.1a).

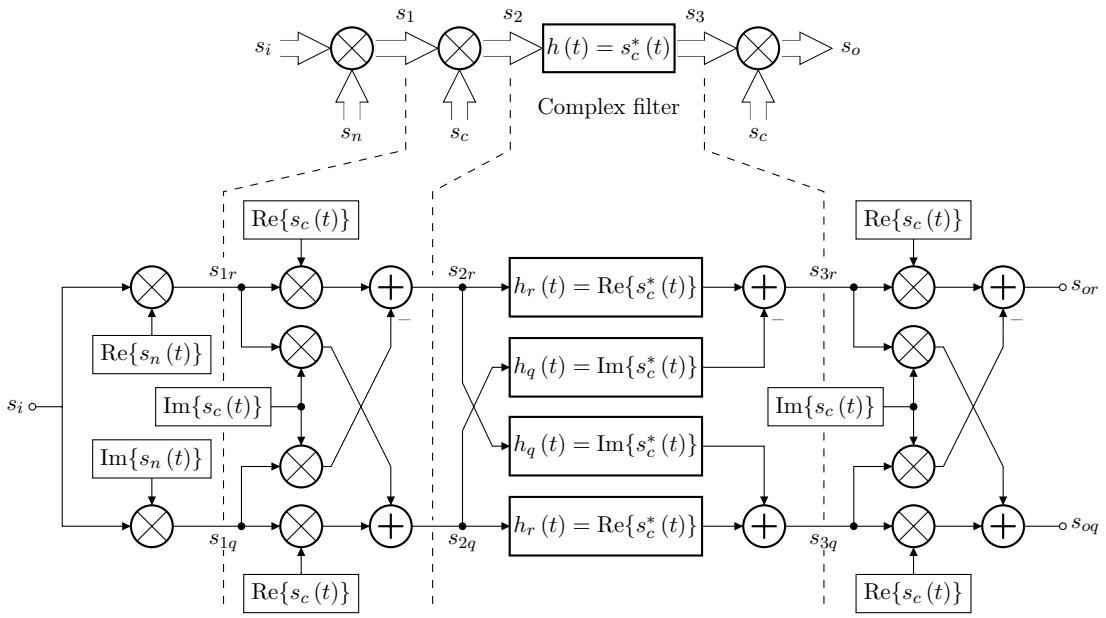

Figure 3.3 – Simplified block diagram (top) and detailed block diagram (bottom) of the proposed analog chirp Fourier Transformer (ACFT).

$$s_c(t) = e^{-j2\pi\left(\frac{k}{2}t^2+f_1t+\varphi\right)} = \underbrace{\cos\left[2\pi\left(\frac{k}{2}t^2+f_1t+\varphi\right)\right]}_{\mathrm{Re}\{s_c(t)\}} - j\underbrace{\sin\left[2\pi\left(\frac{k}{2}t^2+f_1t+\varphi\right)\right]}_{\mathrm{Im}\{s_c(t)\}} \tag{3.2}$$

In the above equations, f_1 is both the chirp start frequency and the frequency of the complex sinusoid, φ is an arbitrary phase, and k, the rate of change of the chirp, given by

$$k = \frac{f_2 - f_1}{T}, \tag{3.3}$$

where f_2 is the chirp end frequency and T, is the chirp sweep time when referring to the chirp signal, or the group delay swing when referring tho the chirp filter.

Considering the simplified diagram, it is easy to verify that the system performs the following operation,

$$\begin{aligned} s_o(t) &= \{[s_i(t)\, s_n(t)\, s_c(t)] * s_c^*(t)\}\, s_c(t) \\ &= \int_0^t s_i(\tau)\, e^{-j2\pi f(t)\tau} d\tau, \end{aligned} \tag{3.4}$$

where $f(t)$ is the instantaneous frequency of the chirp, defined by (3.5), and ψ is the absolute value[4] of the argument of (3.2), the chirp signal. Equation (3.5) establishes a relation between time and frequency that enables mapping the time scale in the frequency scale.

$$f(t) \triangleq \frac{1}{2\pi}\frac{d\psi}{dt} = kt + f_1 \tag{3.5}$$

From (3.4) and (3.5), it can be noticed that the system implements a time-limited version of the causal Fourier integral where, in the frequency band swept by the chirp, each frequency of

[4]If the absolute value of the argument was not taken, the chirp signal would present a negative instantaneous frequency, what is meaningless in practice (see Section A.2).

the spectrum is mapped to a time instant. This directly relates to the *finite Fourier transform* as defined in [71].

Each operation in the simplified block diagram is performed by a set of operations in the detailed ACFT architecture. The architecture allows performing operations on complex signals through the implementation of two signal paths. The upper path (in-phase channel) represents the real part of the complex signal being processed, while the lower path (quadrature channel) represents the imaginary part [17].

The first stage shifts the spectrum so that the correct spectrum is obtained when we are analyzing a spectrum band that does not start at DC. Otherwise, the spectrum would appear shifted at the output of the Fourier transformer. Following the signal paths, the following expressions are obtained for the real and imaginary parts of the intermediate complex signal s_2, respectively.

$$s_{2r}(t) = s_i(t) \cos\left[2\pi\left(\frac{k}{2}t^2\right)\right] \tag{3.6a}$$

$$s_{2q}(t) = -s_i(t) \sin\left[2\pi\left(\frac{k}{2}t^2\right)\right] \tag{3.6b}$$

The above expressions show the input signal modulating a baseband chirp with a rate of change k.

The filter with complex impulse response presents, indeed, a cross-coupled structure with four filters with real impulse responses. The filter with impulse response $h_q(t)$ has a phase that is $\pm\frac{\pi}{2}$ radians (± 90 degrees) shifted from that of the filter with impulse response $h_r(t)$[5]. The output of the complex filter is given by (3.7).

$$s_{3r}(t) = \mathrm{Re}\{s_c(t)\} \int_0^t s_i(\tau) \cos[2\pi f(t)\tau]\, d\tau - \mathrm{Im}\{s_c(t)\} \int_0^t s_i(\tau) \sin[2\pi f(t)\tau]\, d\tau \tag{3.7a}$$

$$s_{3q}(t) = -\mathrm{Re}\{s_c(t)\} \int_0^t s_i(\tau) \sin[2\pi f(t)\tau]\, d\tau - \mathrm{Im}\{s_c(t)\} \int_0^t s_i(\tau) \cos[2\pi f(t)\tau]\, d\tau. \tag{3.7b}$$

The expressions in (3.7) indicate that at the output of the complex filter, the Fourier transform of the input signal modulates the complex chirp. Multiplying s_3 by the chirp, the real and imaginary parts of the complex spectrum are obtained, as shown in (3.8). By squaring both outputs, summing the result, and extracting the square root, we obtain the magnitude spectrum of the input signal.

$$s_{or}(t) = \int_0^t s_i(\tau) \cos[2\pi f(t)\tau]\, d\tau \tag{3.8a}$$

$$s_{oq}(t) = -\int_0^t s_i(\tau) \sin[2\pi f(t)\tau]\, d\tau \tag{3.8b}$$

The last complex multiplication affects only the phase of the signal s_3. If only the magnitude spectrum is desired, this last multiplication can be eliminated.

The real-time analog chirp Fourier transformer (RTACFT) model presented here can be generalized to correspond to any of the Fourier transform definitions (cf. Appendix C). The generalized model is derived in detail in Appendix B.

[5] As explained in [72], a pair of filters, one presenting an impulse response $h_r(t)$, and another presenting an impulse response $h_q(t)$, can be impulsed simultaneously to generate a complex signal (two real signals in quadrature)

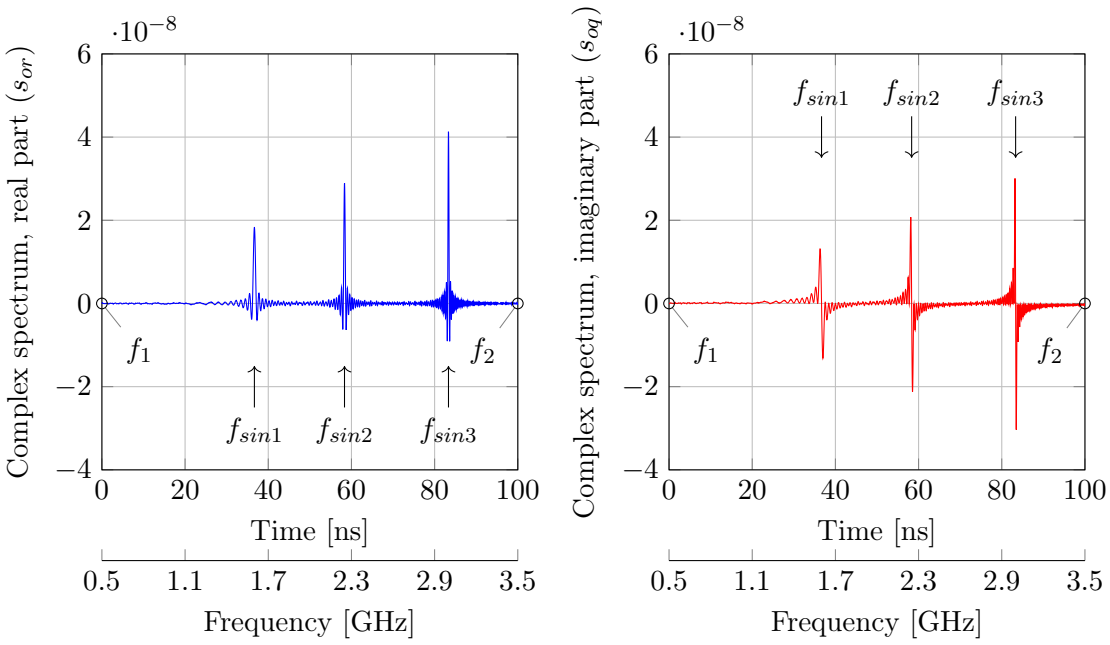

Figure 3.4 – Output complex spectrum for a three-tone input signal.

As the proposed system is based on the MCM algorithm, it is similar to several implementations discussed in Chapter 2. The difference lies in the fact that the continuous-time implementations discussed in Chapter 2 are modeled using complex exponentials according to the MCM algorithm, but their physical implementation does not correspond to this model, but to the compressive receiver architecture described by Klauder et al. in [9].

An architecture similar to the one proposed here is presented in [3], which uses a baseband chirp and omits the multiplication by the complex sinusoid. A baseband chirp is not practical since it entails a frequency sweep starting at DC ($f_1 = 0$). This characteristic, combined with the omission of the multiplication by the complex sinusoid, implies that the system presented in [3] is only capable of generating a baseband spectrum, and is thus a particular case of the more general system presented here. Another difference is that the article in question does not present an architecture suitable for a physical implementation. Actually, the real chirp signal waveform and the real chirp filter impulse response presented in Fig. 1 of that article does not correspond to the complex exponential models given, respectively, in equations (1) and (2) of the same article.

3.3 Discussion on Analytical Results

To verify the system model, the resulting complex spectrum of an input signal composed by the superposition of three pure tones was computed and is shown in Fig. 3.4. Its magnitude spectrum is given in Fig. 3.5. The three tones have unitary amplitudes and frequencies $f_{sin1} = 1.6\,\text{GHz}$, $f_{sin2} = 2.25\,\text{GHz}$ and $f_{sin3} = 3\,\text{GHz}$. The start and stop frequencies for the linear chirps are $f_1 = 500\,\text{MHz}$ and $f_2 = 3.5\,\text{GHz}$, respectively, and the sweep time for all chirp are $T = 100\,\text{ns}$.

Using the simplified block diagram, Fig. 3.6 illustrates this transformation with all the complex signals required by the system, where the blue waveforms correspond to the real part of the

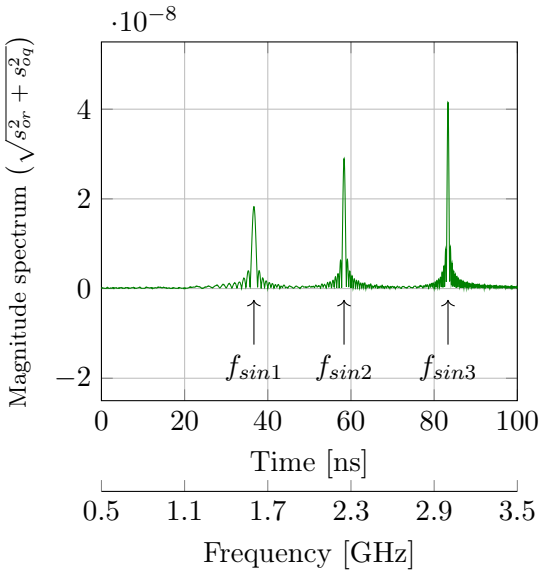

Figure 3.5 – Magnitude spectrum of the three-tone input signal.

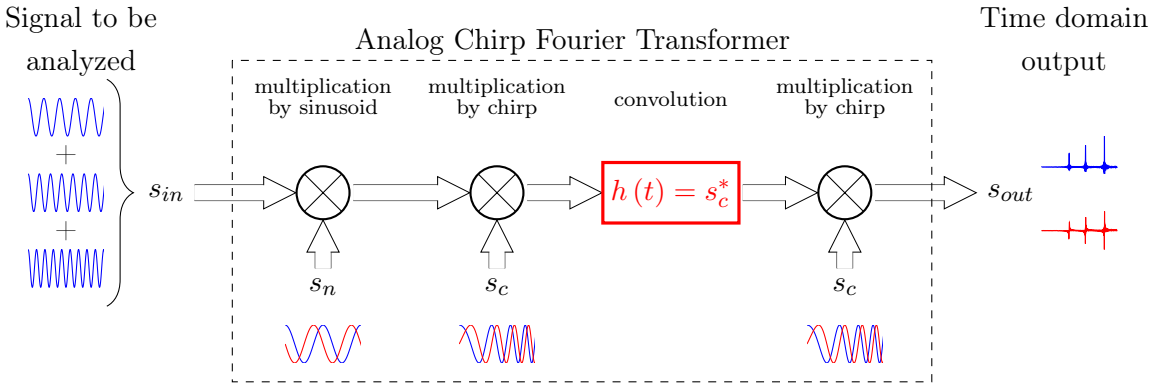

Figure 3.6 – Simplified block diagram of the RTACFT system illustrating the transformation of a three-tone signal, and all the complex signals required for its correct operation.

complex signals, and the red ones to the imaginary parts.

Through the time-to-frequency mapping relation given by (3.5), it can be verified that the frequencies of the three tones are mapped to the time instants $t_1 = 36.7\,\text{ns}$, $t_2 = 58.3\,\text{ns}$ and $t_3 = 83.3\,\text{ns}$. The arrows in Figs. 3.4 and 3.5 indicate these exact instants. Indicated in the figures by small circles, the start and stop frequencies of the chirps, f_1 and f_2, respectively, delimit the spectrum band being analyzed.

Due to the finite integration time of the convolution operation performed by the filter, it can be seen in Fig. 3.4 that the width and amplitude of the pulses improve linearly with time. Ideally, in a time equal to infinity, the pulses become Dirac deltas. Notwithstanding, the components of the spectrum can be equalized through a variable gain amplifier [3].

Active versions of the filters, such as those presented in [34, 37–39], can be used to mitigate the small signal amplitudes at the output of the complex filter due to the finite integration time. In addition, a technique for increasing the group delay slope of the filters, such that presented in [73], can be used to increase the filters group delay swing and, consequently, the integration time.

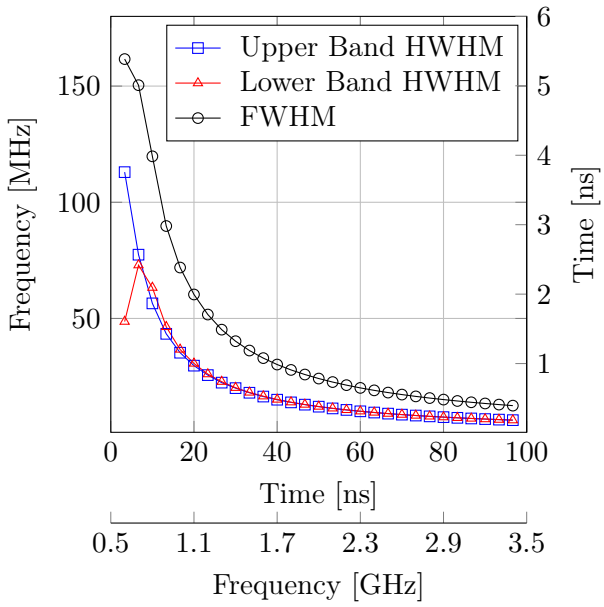

Figure 3.7 – Half width at half maximum (HWHM) and full width at half maximum (FWHM) of the magnitude spectrum for the specified system.

The parameters of *full width at half maximum (FWHM)* and *half width at half maximum (HWHM)*, commonly used to evaluate the resolution of spectrometers [58, 60], can be precisely computed based on (3.8) and a sinusoidal input signal with the frequency of interest. The chirp nature of the system causes the pulses to be slightly asymmetric so that the HWHM of the upper band of the pulse is slightly smaller than that of the lower band. This is only perceptible at the beginning of the spectrum, where the values of the HWHM are large and can be safely ignored. The behavior of the parameters HWHM and FWHM of the magnitude spectrum for the specified system is presented in Fig. 3.7.

The expression of the maximum frequency resolution of a chirp transform (CT) processor given in [14] can be generalized through (3.9) to give an estimate of the frequency resolution at a specific time instant (that relates to a particular frequency component through the time-frequency mapping relation).

$$f_r(t) = \frac{1}{t}. \tag{3.9}$$

3.4 Effects of System Imperfections

Several types of errors were considered in the investigation of the robustness of the proposed system: mismatch between the rates of change of the complex chirp signal and the complex filter impulse response; quadrature imbalance of signals and in the channel (due to complex multipliers and transfer functions), as explained in [17]; and shifts in the frequency of the complex sinusoid and the starting frequencies of the chirps.

As already stated in other works [5, 24, 58, 60], the mismatch between the group delay slope of the chirp filter and the slope of the rate of change of the frequency of the chirp signal, parameter k in (3.2), is essential for proper system operation. Even if the start and end frequencies of the

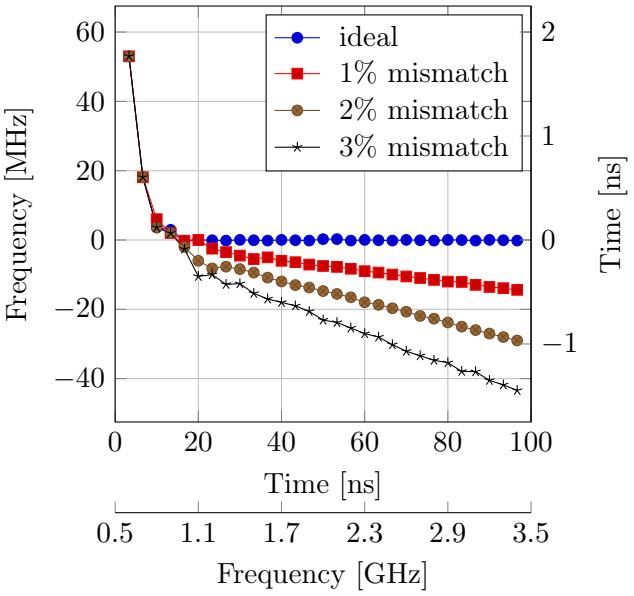

Figure 3.8 – Mapping error for different mismatches between the chirp rate of the chirp signal and the filter impulse response.

chirp signal and the filter impulse response are not the same, the response can be made correct as long as their k parameters match. Considering the system specified in Section 3.3, Fig. 3.8 shows the error of mapping a frequency component to the respective time instant for different mismatch levels. At the beginning of the spectrum, the amplitude of the spectrum components are very small, and a mapping error exists even when no mismatch exists. However, this error is small and of little concern. Fig. 3.11b shows the magnitude spectrum of the example of Section 3.3 when a mismatch of 2 % between the group delay slope of the chirp filter and the slope of the rate of change of the frequency of the chirp signal is present. With a 2 % mismatch, the components are just slightly outside their expected time instant, given by the arrows, even the higher frequency component, that presents the biggest mapping error.

A bigger problem can be seen in the magnitude and the width of the spectral components (compare Fig. 3.11b with the ideal magnitude spectrum presented in Fig. 3.11a). As the mismatch increases, the amplitudes of the spectral components decrease, and their widths widen (i.e., the frequency resolution decreases). Figs. 3.9 and 3.10 show this trend.

A possible solution that can mitigate the problems caused by this mismatch was presented in [60], where an adaptive circuit was used to generate a chirp signal with characteristics matching those of the filter, significantly improving the performance of the overall system.

A 10 % magnitude imbalance between the real and imaginary parts of the complex sinusoid and the two chirp signals is shown in Fig. 3.11c and are of minor concern, as well as imbalances in the complex multipliers. Phase errors may give rise to the appearance of parasitic pulses, as shown in Fig. 3.11d, where a mismatch of 10 degrees was modeled between the real and imaginary parts of the complex sinusoid.

A mismatch between the start frequencies of the chirp signals and the filter impulse responses, in the hypothesis of a matching k parameter, and a shift in the frequency of the complex sinusoid, f_1 in (3.1), results in a displaced spectrum. The displacement of the spectrum is of concern only if

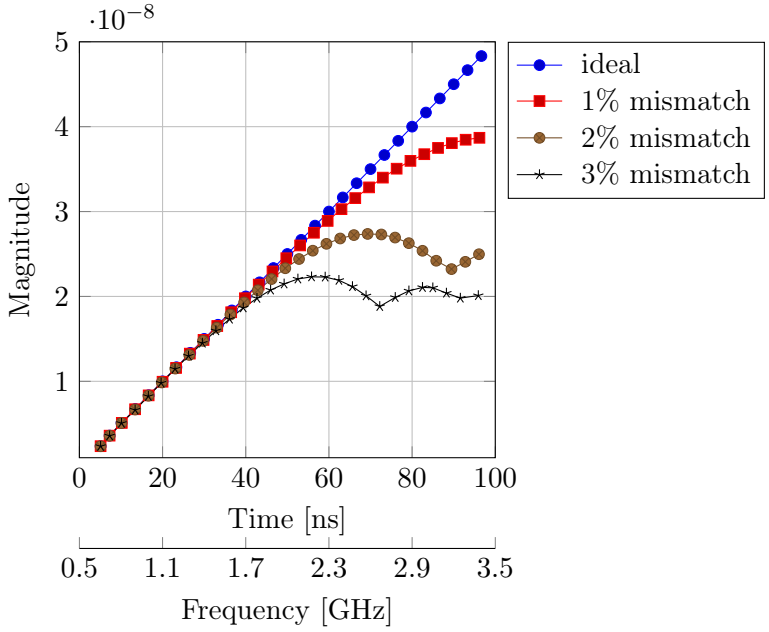

Figure 3.9 – Magnitude deviation considering the maximum magnitude attained by the pulse (not necessarily at its center) for different mismatches between the chirp rate of the chirp signal and the filter impulse response.

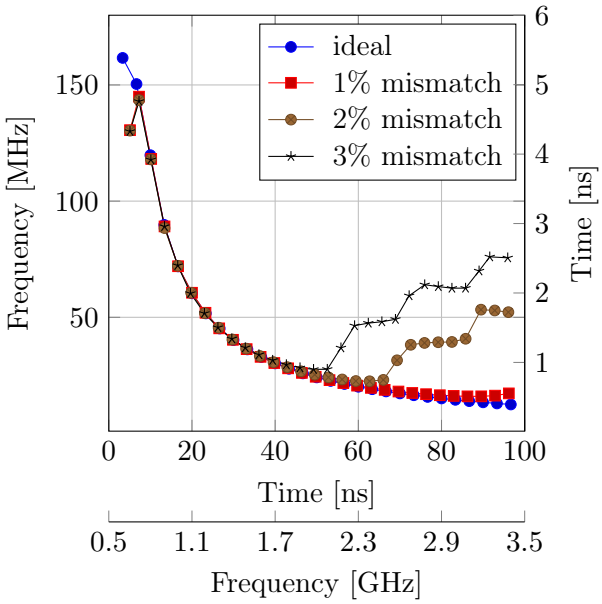

Figure 3.10 – Deviation of the Full width at half maximum (FWHM) characteristic of the magnitude spectrum for the specified system, for different mismatches between the chirp rate of the chirp signal and the filter impulse response.

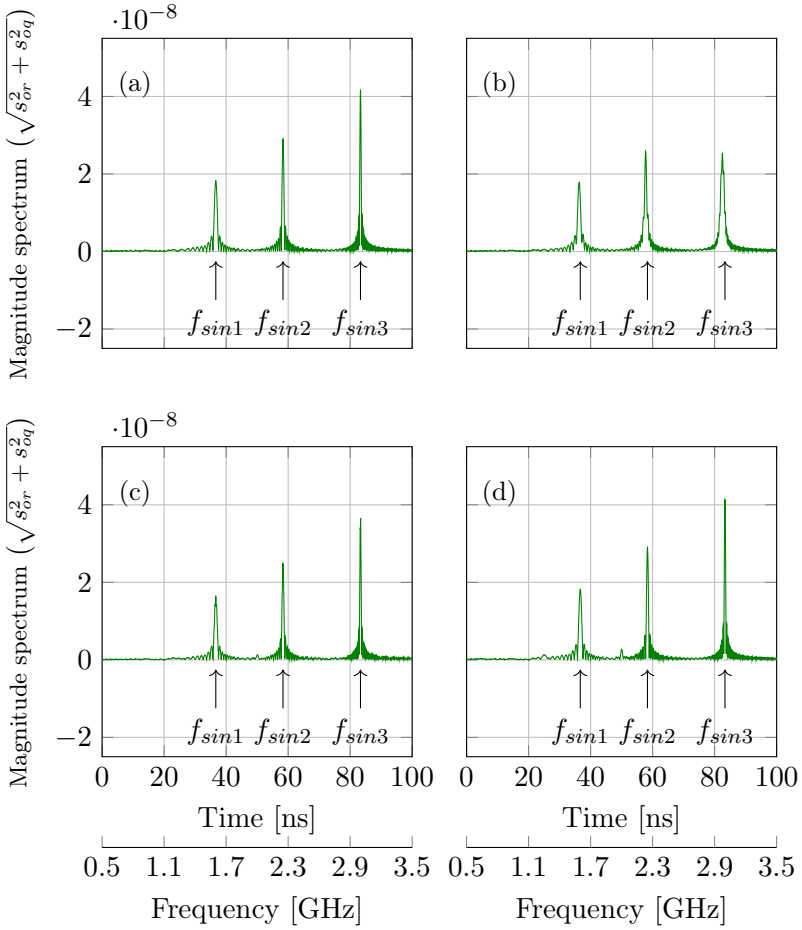

Figure 3.11 – Magnitude spectrum: (a) of ideal system, (b) when the k parameter of the chirp signal and the filter impulse response has a mismatch of 2 %, (c) for a 10 % magnitude imbalance between the real and imaginary parts of the complex sinusoid and chirp signals, (d) for a 10° phase imbalance between the real and imaginary parts of the complex sinusoid and chirp signals.

it is significant enough to hide frequency components occurring at the extremes of the spectrum.

3.5 Equalizing Spectrum Amplitude and Resolution

To compensate for the variation in pulse amplitude over time, it has been suggested in [3] to use a variable gain amplifier (VGA) with a ramp control voltage, with slope equal to the negative slope of the linear rate of change of the chirp.

As shown in Fig. 3.12, another way to simultaneously compensate for variations in pulses width and amplitude, stems from the observation that an ACTS designed considering a down-chirp for the chirp carrier and the phaser impulse response, generates a reverse spectrum - i.e., a spectrum where the high frequencies are at the beginning of the sweep interval (T), while the lower frequencies are at its end. Therefore, if this spectrum is reversed through a time reversal technique, as explained in [74], and summed to the adequately delayed spectrum outputted by another ACTS, realized considering an up-chirp for the chirp carrier and phaser impulse response,

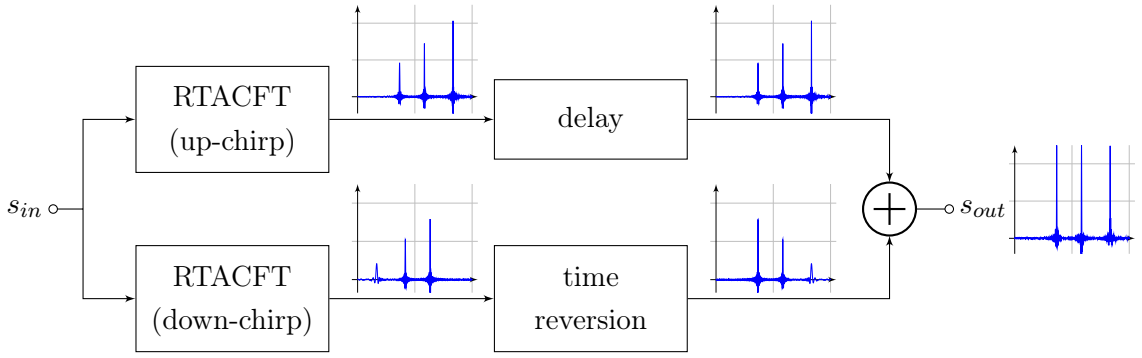

Figure 3.12 – Scheme to compensate for the variation in dispersion and amplitude of the pulses over time, with simulation results showing just the real part of the resulting spectrum for a three-tone sinusoid input signal.

the resulting spectrum would be equalized in amplitude to that of a frequency component at $t = T$. Consequently, the frequency resolution would also be equalized to that of a component at $t = \frac{T}{2}$.

Considering the example parameters given in Section 3.3, it was verified empirically that the system of Fig. 3.12 could resolve spectral components that are 20 MHz apart. If the sweep time is increased by three orders of magnitude, to 100 µs, the system resolution is enhanced by the same order of magnitude, being able to discriminate frequency components 20 kHz apart. Likewise, pulses amplitudes also increase in three orders of magnitude.

Fig. 3.13 presents the HWHM and the FWHM of the magnitude spectrum for the scheme presented in Fig. 3.12.

3.6 Conclusion

In this chapter, the MCM configuration has been discussed through the angle of limitations when making a physical implementation. Many previous works simplified the MCM configuration to implement only the real part of the complex filter and signals. This simplification leads not only to the loss of the information about the phase spectrum but also to a degradation of the magnitude spectrum with the appearance of parasitic lobes, increasing the risk of false detection of frequency components. These shortcomings motivated the proposal, in this chapter, of a two-paths architecture, realizing the real and imaginary parts of complex signals, leading to an accurate spectrum representation. This architecture is more complex than the simplified ones presented in the literature, but despite its complexity and unavoidable mismatches, it promises an increased accuracy in the spectrum representation.

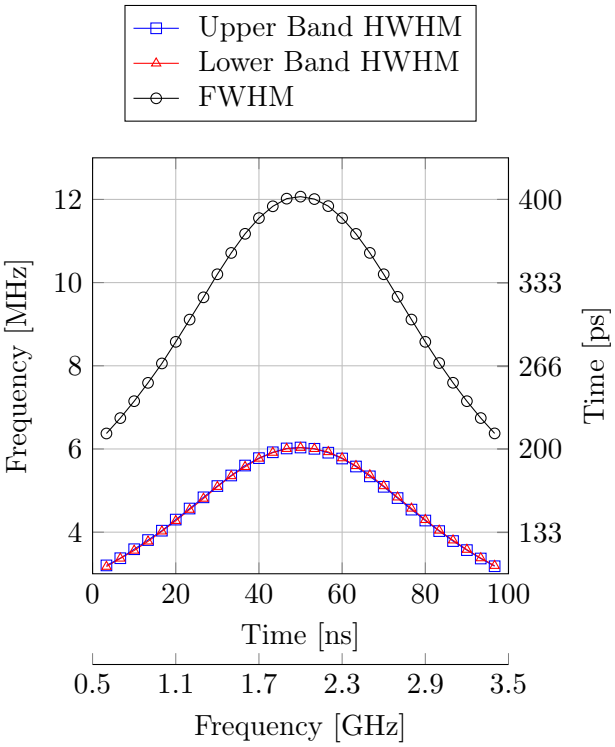

Figure 3.13 – Half width at half maximum (HWHM) and full width at half maximum (FWHM) of the magnitude spectrum for the improved RTACFT system.

Chapter 4

Filters with Engineered Group Delay or Phase - Part I: Minimum Phase Filters

4.1 Engineered Group Delay Filters in the State of the Art

Filters with engineered group delay enable operations as stretching, compression, and reversion of electronic signals in the time domain [74] and thus are essential building blocs on analog signal processing (ASP). These filters are employed in a big range of systems and applications, like compressive receivers [31–33], radars [7, 9, 75], chirp transform spectrometers (CTSs) [52, 54, 57, 58], real-time wideband spectrum analysis [3, 41, 46], real-time spectrum sniffing [4], pulse-position modulation [76], tunable delay lines [77], to cite some. In particular, filters with linear group delay (quadratic phase) are required for realizing the architecture of the real-time analog chirp Fourier transformer (RTACFT) proposed in Chapter 3 (cf. Sections A.4 and 3.2).

The design of wideband filters with engineered group delay—also known as phasers [2, 78], chirp filters [19, 23, 25], dispersive filters [12, 79], or dispersive delay lines (DDLs) [34, 45]—is the core problem in analog signal processing [2, 80]. From this chapter on, the thesis will focus on the study of filters with linear group delay (quadratic phase). However, this study will be generalized to develop design methods for filters with arbitrary group delay (and phase). This way, ASP applications requiring filters with engineered group delay can also benefit from this work.

Filters requiring a specific group delay characteristic can be obtained by optimization [81] or direct manipulation of the poles and zeros of the transfer function [82]. In the optimization approach, obtaining a result that meets the specifications cannot be guaranteed, and the design process does not give much insight into the trade-offs involved. On the other hand, direct manipulating the poles and zeros of the transfer function to get the desired filter response is laborious and requires experience. Other methods for the design of filters with engineered group delay for different microwave technologies have been mentioned in [2]. However, these techniques focus on non integrated planar and guided wave technologies.

The current state of the art in the design of filters with engineered group delay for implementation in integrated technologies is the work of Bo Xiang et al. [37–39, 44, 45], and of Salvucci et al. [34]. Bo Xiang succeeded to implement and demonstrate three different versions of an integrated distributed amplifier-based transversal filter. Such filters present roughly linear group

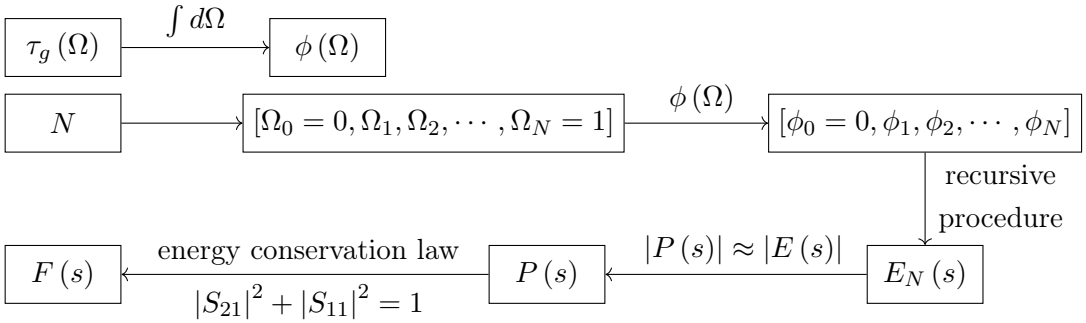

Figure 4.1 – Flowgraph of the procedure to synthesize the lossless lowpass prototype filter polynomials $E(s)$, $P(s)$ and $F(s)$, starting from a specified phase ϕ or group delay τ_g and filter order N.

delays obtained through complicated design procedures [38, 39, 44, 45], or explore the subbands of the filter where the group delay is approximately linear [37]. The solutions still suffer from poorly behaved responses in magnitude and group delay. Bo Xiang's implementations illustrate the complexity of current engineered group delay integrated filter architectures and design techniques.

More recently, Salvucci et al. [34] designed another distributed amplifier-based transversal filter in gallium nitride (GaN) monolithic microwave integrated circuit (MMIC) technology using dual composite right-left handed (D-CRLH) transmission lines. Salvucci's simulations show a flat magnitude response and a group delay response that, although not linear throughout all the filter passband, can be considered piecewise linear if the passband is divided into subbands.

The present chapter focuses on the design of wideband filters with an arbitrary group delay (or phase) specification and their synthesis on doubly terminated ladder networks. The passive ladder networks are known to present low sensitivity to component value variation and can be readily converted into an active structure (e.g., OTA-C filters).

4.2 Design and Synthesis Procedures

4.2.1 Generation of Filter Polynomials

In filter theory, it is common to represent the forward transmission coefficient (S_{21}) and the input reflection coefficient (S_{11}) of a lossless passive network as the ratio of polynomials [82, Sec. 3.2.1]

$$S_{21} = \frac{P(s)}{E(s)} \tag{4.1a}$$

$$S_{11} = \frac{F(s)}{E(s)}, \tag{4.1b}$$

where $E(s)$ must be a Hurwitz polynomial, i.e., a polynomial with all its roots lying in the left half-plane.

The first step in the design of filters consists of finding the polynomials in (4.1) for the lossless lowpass prototype filter. For this, the present work uses the method described in [80].

The flowgraph of the procedure used to synthesize the prototype filter polynomials is shown in Fig. 4.1 and is described below.

The procedure starts with the phase specification of the prototype filter, $\phi(\Omega)$, where Ω is a normalized frequency, with $\Omega = 1$ being the cutoff frequency of the lowpass prototype filter. Since the designer is generally more concerned with the filter group delay, $\phi(\Omega)$ can be obtained by integrating the group delay specification of the prototype filter, $\tau_g(\Omega)$.

Once the filter order N is defined, a set of $N+1$ frequency values in the interval $[0,1]$ is created, preferably, with frequencies equally spaced in the interval. The extreme values of the interval are required to be in the set. Subsequently, a set of phase values are calculated from this set of frequencies and the phase specification.

The denominator polynomial, $E(s)$, is obtained through the recursive procedure given by

$$E_n(s) = \begin{cases} 1, & n = 0 \\ s + \alpha_0, & n = 1 \\ \alpha_{n-1} E_{n-1}(s) + \left(s^2 + \Omega_{n-1}^2\right) E_{n-2}(s), & n \geqslant 2 \end{cases}, \tag{4.2}$$

where

$$\alpha_i = \begin{cases} \dfrac{\Omega_1}{\tan\phi_1}, & i = 0 \\ \cfrac{\Omega_{i+1}^2 - \Omega_i^2}{\alpha_{i-1} - \cfrac{\Omega_{i+1}^2 - \Omega_{i-1}^2}{\alpha_{i-2} - \cfrac{\Omega_{i+1}^2 - \Omega_{i-2}^2}{\ddots \cfrac{}{\alpha_0 - \cfrac{\Omega_{i+1}}{\tan\phi_{i+1}}}}}}, & i \geq 1 \end{cases}. \tag{4.3}$$

As a magnitude of one (i.e., 0 dB) is generally desired in the filter passband, the transfer function numerator polynomial, $P(s)$, is determined by the following procedure: first, the polynomial $E(s)\big|_{s=j\Omega}$, where $s = j\Omega$ is the complex frequency, is approximated by a truncated Chebyshev expansion through [83]

$$P(j\Omega) \approx \sum_{i=0}^{M} c_i T_i(\Omega), \tag{4.4}$$

where M is the desired order of the $P(s)$ polynomial and should be less than or equal to the filter order N (i.e., the order of the $E(s)$ polynomial), T_i is the Chebyshev polynomial of the first kind of order i, and c_i is given by

$$c_i = \begin{cases} \dfrac{1}{\pi} \displaystyle\int_{-1}^{1} \frac{\sqrt{E(j\Omega)\,E(-j\Omega)}\,T_i(\Omega)}{\sqrt{1-\Omega^2}} d\Omega, & i = 0 \\ \dfrac{2}{\pi} \displaystyle\int_{-1}^{1} \frac{\sqrt{E(j\Omega)\,E(-j\Omega)}\,T_i(\Omega)}{\sqrt{1-\Omega^2}} d\Omega, & i > 0 \end{cases} \tag{4.5}$$

Then, the resulting polynomial is normalized according to

$$P_{norm.}(j\Omega) = \frac{P(j\Omega)}{\max\limits_{-1 \leqslant \Omega \leqslant 1} \left\{ \dfrac{P(j\Omega)}{|E(j\Omega)|} \right\}}, \tag{4.6}$$

where $\max_{-1\leqslant x\leqslant 1}\{f(x)\}$ returns the maximum value of $f(x)$ in the interval $-1 \leqslant x \leqslant 1$, so that $|S_{21}| \leqslant 1$. The $P(s)$ polynomial is obtained by evaluating (4.6) for $\Omega = \frac{s}{j}$, i.e.,

$$P(s) = P_{norm.}(j\Omega)\Big|_{\Omega=\frac{s}{j}}. \tag{4.7}$$

The last polynomial, $F(s)$, the numerator of the input reflection coefficient function, is determined through the energy conservation law, that can be rewritten as

$$F(s)F(-s) = E(s)E(-s) - [P(s)]^2. \tag{4.8}$$

Since $F(s)F(-s)$ has $2N$ roots, which are symmetrically distributed about the imaginary axis or lie in pairs in the imaginary axis, the $F(s)$ polynomial is formed by taking all the roots in the left half-plane and one of the roots of each pair laying in the imaginary axis.

4.2.2 Synthesis of Filter Networks

The second step in the design of filters consists in synthesizing the filter network from the generated polynomials. The authors in [80] use the coupling matrix technique to synthesize the filter in a waveguide cross-coupled microwave structure.

This technique is targeted to the synthesis of microwave filters and is only capable of generating bandpass coupling filter topologies of, generally, narrow bandwidth, since coupling elements are commonly assumed to be frequency invariant admittance or impedance inverters.

Another option is to use the classical circuit synthesis approach. In this approach, an electrical network can be synthesized from the [ABCD] (or "chain") matrix representation of the filter [82, Ch. 7]. In the specific case of lumped element ladder networks, the values of the components of the network can be found by expanding S_{11} in a continued fraction [84, Sec. 2.5].

After the synthesis of the lowpass prototype filter, the resulting network can be transformed into another class of filter (e.g., highpass, bandpass, bandstop) and scaled in impedance and frequency [84, pp. 32-41], without being subjected to any bandwidth restriction.

4.3 Design and Synthesis Example

A fourth-order filter presenting a positive slope group delay is synthesized through a doubly terminated ladder network to illustrate the design and synthesis procedures. The synthesis of such structure is appealing as it is well known that it presents low sensitivity to components values variation [85, Sec. 3.3.8]. Another particular advantage of ladder networks is that they are generally used as a starting point for the synthesis of active networks.

A group delay swing of one second over the passband of the lowpass prototype filter (i.e., $0 \leqslant \Omega \leqslant 1$) was specified. The expressions for the transfer function and the input impedance of the prototype filter obtained using the algorithm shown in Fig. 4.1 and explained in Section 4.2.1 are presented in (4.9), while Figs. 4.2a and 4.2c show two tantamount networks that were synthesized by expanding (4.9b) into a continued fraction [84, Sec. 2.5]. The frequency response and group delay of the equivalent lowpass prototype networks of Figs. 4.2a and 4.2c are shown in Fig. 4.3,

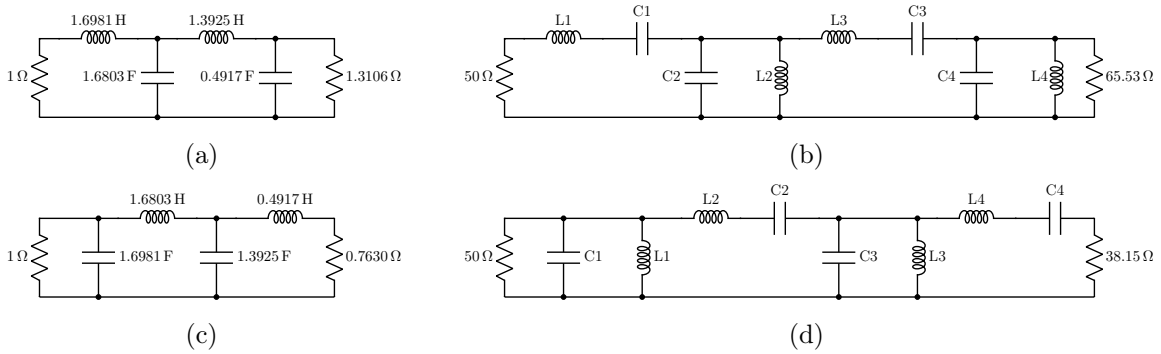

Figure 4.2 – Synthesized networks: (a) lowpass prototype starting with a series inductor, (b) resulting network from the bandpass transformation and scaling of Fig. 4.2a to an impedance of 50 ohms and a bandwidth of 500 MHz centered around 1 GHz (components values in Table 4.1), (c) lowpass prototype starting with a shunt capacitor, (d) the resulting network from the bandpass transformation and scaling of Fig. 4.2c to and impedance of 50 ohms and a bandwidth of 500 MHz centered around 1 GHz (components values in Table 4.1).

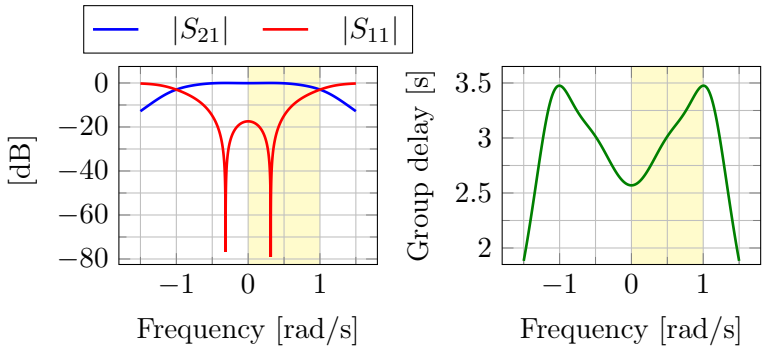

Figure 4.3 – Frequency response and group delay for the lowpass prototype networks, with the band of the filter presenting the specified group delay highlighted in yellow.

with the band of the filter presenting the desired group delay highlighted in yellow.

$$S_{21}(s) = \frac{0.89430}{s^4 + 2.1408s^3 + 3.1524s^2 + 2.3190s + 0.90249} \tag{4.9a}$$

$$S_{11}(s) = \frac{s^4 + 0.96301s^3 + 1.3245s^2 + 0.09532s + 0.12131}{s^4 + 2.1408s^3 + 3.1524s^2 + 2.3190s + 0.90249} \tag{4.9b}$$

Since a ladder structure can only realize transfer functions with transmission zeros in the $j\omega$-axis [85, p. 89], to be able to synthesize a ladder network, the order of the $P(s)$ polynomial was specified equal to zero in the algorithm. This resulted in a minimum phase transfer function. Due to the relation existing between the magnitude and phase of a causal system (i.e., Bode relations [86]), the lack of finite frequency transmission zeros prevents obtaining a flatter magnitude characteristic in the filter passband without changing the specified group delay.

An order of four has been chosen for the filter so that an almost linear group delay characteristic is obtained with a maximum attenuation of −3 dB in the passband (at the cutoff frequency). Increasing the filter order would increase the passband attenuation, with negligible improvement in the group delay characteristic.

Table 4.1 – Components values for the networks of Figs. 4.2b and 4.2d.

	Network of Fig. 4.2b	Network of Fig. 4.2d		Network of Fig. 4.2b	Network of Fig. 4.2d
C1	999.8 fF	10.81 pF	L1	27.03 nH	2.499 nH
C2	10.70 pF	1.010 pF	L2	2.526 nH	26.74 nH
C3	1.219 pF	8.865 pF	L3	22.16 nH	3.048 nH
C4	3.130 pF	3.453 pF	L4	8.632 nH	7.825 nH

Table 4.2 – Technology parameters values for the components of the network of Fig. 4.2d.

	Capacit.	Width		Internal diameter	No. of turns	Line width
C1	10.689 pF	73 µm	L1	143.335 µm	3	11.99 µm
C2	1.010 pF	22 µm	L2	137.310 µm	9	5.055 µm
C3	8.788 pF	66 µm	L3	162.965 µm	3	8.065 µm
C4	3.448 pF	41 µm	L4	163.000 µm	5	8.235 µm

Beyond the shown networks, several others can be obtained. For instance, it is common to replace the series inductors by shunt capacitors by surrounding it by admittance inverters, creating what is known as a direct-coupled-resonator filter [87], [84, Sec. 2.8], [82, Sec. 7.2]. Likewise, a shunt capacitor can be transformed into a series inductor through the use of impedance inverters. The diversity of networks that can be obtained allows finding a network that is better suited for implementation in a particular technology.

Applying a bandpass transformation to the lowpass prototype networks of Figs. 4.2a and 4.2c and scaling them in frequency and impedance to a bandwidth of 500 MHz centered around 1 GHz and and impedance of 50 Ω, the networks of Figs. 4.2b and 4.2d are obtained, respectively. The components values for both networks are listed in Table 4.1.

Considering the ideal component values in Table 4.1, the frequency response and the group delay for the bandpass networks of Figs. 4.2b and 4.2d are displayed in Fig. 4.4a with a continuous trace. The band of interest is highlighted in yellow. The same metrics are illustrated in Fig. 4.4b for a bandpass network with the same center frequency but a bandwidth of 200 MHz.

Fig. 4.4 shows an asymmetry in the group delay characteristics. This distortion is caused by the lowpass to bandpass transformation [88, 89]

$$\Omega \rightarrow \frac{\omega_c}{\omega_2 - \omega_1}\left(\frac{\omega}{\omega_c} - \frac{\omega_c}{\omega}\right), \tag{4.10}$$

where ω_c is the center frequency of the bandpass filter.

The group delay of the badpass filter is given by

$$\tau_g^{BP}(\omega) = -\frac{d\Theta(\Omega)}{d\omega} = -\frac{d\Theta(\Omega)}{d\Omega}\frac{d\Omega}{d\omega} = \tau_g^{LP}(\Omega)\Big|_{\Omega=\omega} f(\omega), \tag{4.11}$$

where $\Theta(\Omega) = \arg[H(j\Omega)]$ is the argument (or phase) of the transfer function, $\tau_g^{LP}(\Omega)\Big|_{\Omega=\omega}$ is

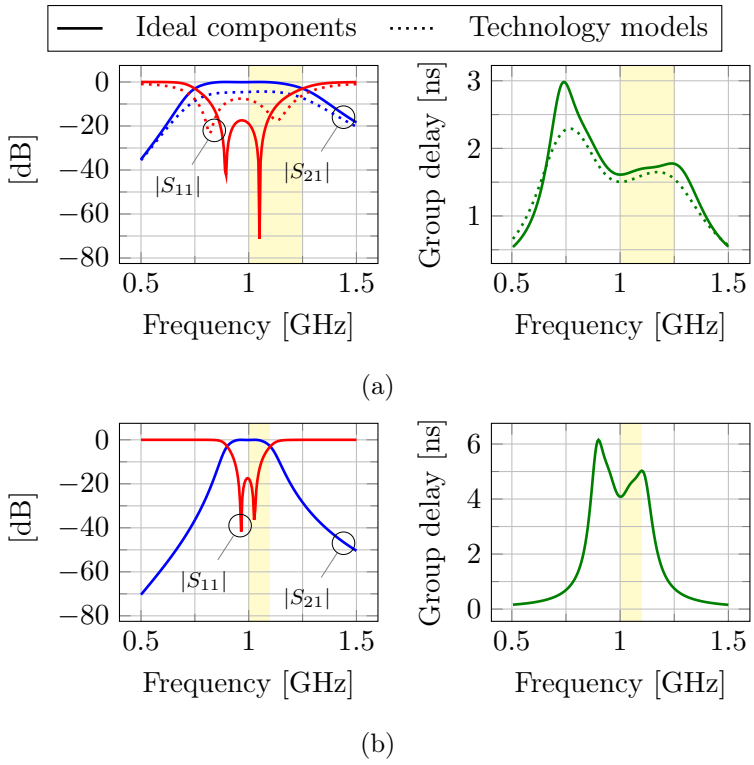

Figure 4.4 – Frequency response and group delay for: (a) the bandpass networks of Figs. 4.2b and 4.2d considering: ideal components (continuous trace) and technology models (dotted trace), (b) an equivalent bandpass network, but with a bandwidth of 200 MHz centered around 1 GHz (network not shown).

the transformed lowpass group delay characteristic, and

$$f(\omega) = \frac{d\Omega}{d\omega} = \frac{1}{\omega_2 - \omega_1}\left(1 + \frac{\omega_c^2}{\omega^2}\right) \tag{4.12}$$

is a distortion factor that distorts the bandpass group delay characteristic causing the asymmetry. The delay at frequencies below ω_c is emphasized, while the delay at frequencies above ω_c is deemphasized.

Another aspect that is illustrated in in Fig. 4.4 is the trade-off that exists between group delay swing and bandwidth [82, Sec. 3.8.2], showing that the group delay swing increases as the bandwidth decreases, and vice-versa. For analog signal processing, these effects imply a trade-off, as a wide group delay swing is generally desired.

The components of the circuit of Fig. 4.2d were sized for implementation in the ST BiCMOS9MW technology. The models *cmim3pM2* and *indsym_lamwM2* were used for, respectively, capacitors and inductors[1]. Table 4.2 lists the dimensioned parameter values for each component. The results of the nominal simulation of the scheme of Fig. 4.2d, considering the accurate models above, are superimposed to the ideal curves of Fig. 4.4a.

The attenuation in the passband of the simulated response of Fig. 4.4a is mainly due to the high series resistance associated with the inductor L_2. The rounding of the transfer function

[1]More information on these models are given in Appendix D

affects the group delay characteristic. Parasitics also affect matching and, consequently, the reflection coefficient response.

4.4 Conclusion

This chapter introduced a filter design method based on a recursive procedure that facilitates the design of filters with engineered group delay and the exploration of the design space to acquire better insights on trade-offs (like the trade-off between bandwidth and group delay swing). Based on this method, a passive fourth-order doubly-terminated bandpass ladder filter with linear group delay was designed and implemented in a BiCMOS 0.13 µm technology. The effect of group delay distortion caused by the lowpass to bandpass transformation was highlighted. Notwithstanding, the possibility of realizing passive or active networks and synthesizing different equivalent networks are attractive for finding a better-suited network for a particular technology or application (for instance, networks presenting smaller values of inductance or capacitance, or presenting only inductors or only capacitors).

Chapter 5

Filters with Engineered Group Delay or Phase - Part II: All-Pass Filters

This chapter complements the subject of Chapter 4 by consecrating itself to the study of all-pass filters with engineered group delay and their realization through constant-resistance lattice and bridged-T networks.

5.1 Design and Synthesis Procedures

5.1.1 Transfer Function Generation

The objective when designing an all-pass filter is to obtain the numerator and denominator polynomials of the filter transfer function, $E(s)$ and $P(s)$, respectively. The method explained here consists of generating the mentioned polynomials for an all-pass prototype filter and then frequency scaling the prototype filter transfer function. The procedure for generating the denominator polynomial was first proposed by Henk [90] and is illustrated in Fig. 5.1.

The designer starts by specifying the desired group delay function $\tau_g(\Omega)$ in the range $\Omega = 0$ to $\Omega = 1$, where Ω is a normalized frequency. The values 0 and 1 correspond to the limits of the operating band of the filter. The related phase function $\phi(\Omega)$ is obtained by integrating $\tau_g(\Omega)$ with respect to the normalized frequency. Then, a desired initial order N is specified for the filter. The prescribed filter order may be insufficient to generate the desired group delay characteristic. In this case, the designer can increase the prescribed order or modify the group delay specification.

The next step consists in creating a set of $N + 1$ normalized frequency values, where the

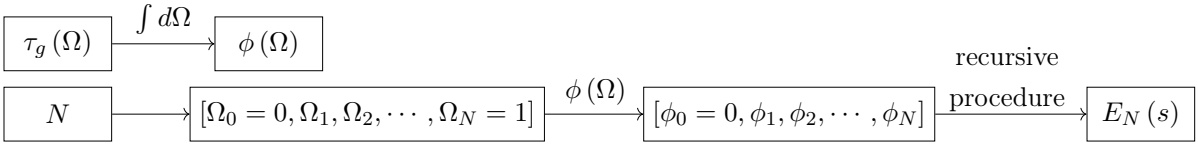

Figure 5.1 – Flowgraph of the procedure to generate the all-pass prototype filter polynomial $E(s)$, starting from a specified group delay function $\tau_g(\Omega)$, where Ω is a normalized frequency, and filter order N.

lowest frequency value should be 0 and the highest 1. From this set of normalized frequency values, another set is created by evaluating $\phi(\Omega)$ for all the normalized frequency values of the previous set.

The transfer function denominator polynomial, $E(s)$, is generated by a recursive procedure given by [80, 90]

$$E_n(s) = \begin{cases} 1, & n = 0 \\ s + \alpha_0, & n = 1 \\ \alpha_{n-1} E_{n-1}(s) + \left(s^2 + \Omega_{n-1}^2\right) E_{n-2}(s), & n \geq 2 \end{cases}, \tag{5.1}$$

where $0 \leqslant n \leqslant N$, and

$$\alpha_i = \begin{cases} \dfrac{\Omega_1}{\tan\phi_1}, & i = 0 \\ \cfrac{\Omega_{i+1}^2 - \Omega_i^2}{\alpha_{i-1} - \cfrac{\Omega_{i+1}^2 - \Omega_{i-1}^2}{\alpha_{i-2} - \cfrac{\Omega_{i+1}^2 - \Omega_{i-2}^2}{\ddots \cfrac{}{\alpha_0 - \cfrac{\Omega_{i+1}}{\tan\phi_{i+1}}}}}}, & i \geq 1 \end{cases}. \tag{5.2}$$

The numerator polynomial, $P(s)$, is then given by

$$P(s) = E(-s). \tag{5.3}$$

The transfer function of the all-pass prototype filter is then given by

$$H(s) = \frac{P(s)}{E(s)} = \frac{E(-s)}{E(s)}. \tag{5.4}$$

5.1.2 Network Synthesis Procedure

Electronic filters are generally built by combining simple network sections. Two types of networks are usually used to realize passive all-pass filters, the lattice, and the bridged-T networks. The lattice network, illustrated in Fig. 5.2, is a balanced network, while the bridged-T, shown in Fig. 5.3, is its unbalanced equivalent. Both networks are examples of constant-resistance networks. They are highly versatile since their characteristic impedance is independent of their transmission properties [91].

The values of the components of a first- or second-order lattice section can be found from the coefficients of its transfer function. Alternatively, it can also be found through the real and imaginary parts of the roots of its transfer function—here noted as, respectively, σ_i and ω_i [92].

- First-order section (A-section): $H(s) = \dfrac{c - s}{c + s}$

$$L_a = \frac{R}{c} = \frac{R}{\sigma_i}, \quad C_b = \frac{1}{Rc} = \frac{1}{R\sigma_i} \tag{5.5}$$

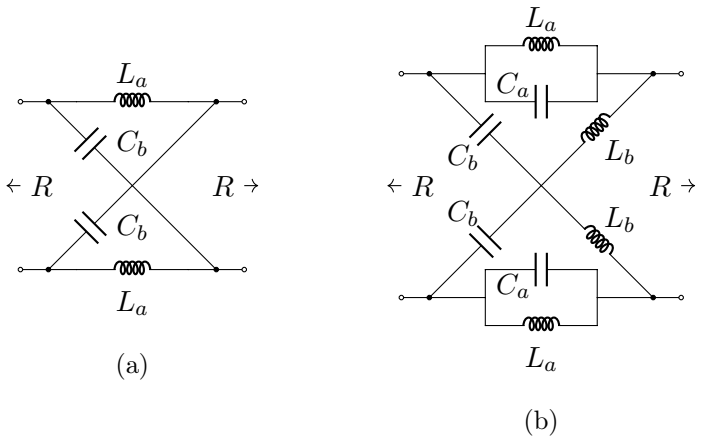

Figure 5.2 – Lattice networks: (a) first-order section, (b) second-order section.

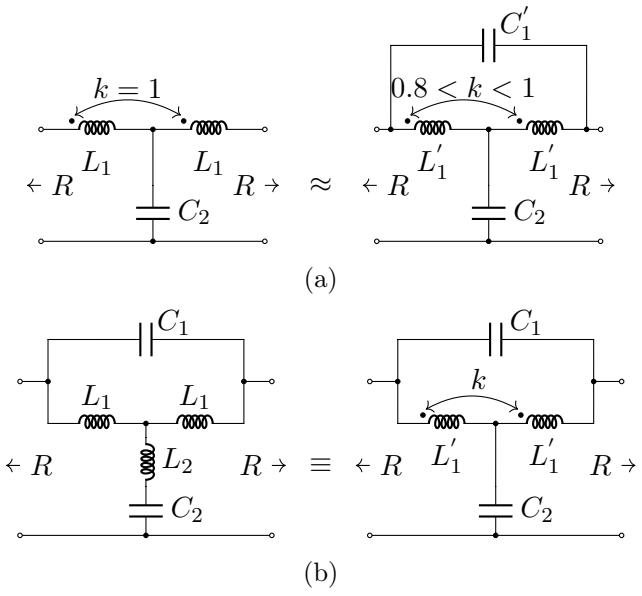

Figure 5.3 – Bridged-T networks: (a) first-order section, (b) second-order section.

- Second-order section (B-section): $H(s) = \dfrac{s^2 - as + b}{s^2 + as + b}$

$$\begin{aligned} L_a &= \frac{Ra}{b} = \frac{2R\sigma_i}{\sigma_i^2 + \omega_i^2}, \quad C_a = \frac{1}{Ra} = \frac{1}{2R\sigma_i} \\ C_b &= \frac{a}{Rb} = \frac{2\sigma_i}{R\left(\sigma_i^2 + \omega_i^2\right)}, \quad L_b = \frac{R}{a} = \frac{R}{2\sigma_i} \end{aligned} \tag{5.6}$$

The lattice network can be converted into a bridged-T network through the use of the following relations:

- First-order section:

$$L_1 = \frac{L_a}{2}, \quad C_2 = 2C_b \tag{5.7}$$

- Second-order section:

$$C_1 = \frac{C_a}{2}, \quad C_2 = 2C_b \tag{5.8}$$

– Without coupling between the coils ($k = 0$):

$$L_1 = L_a, \quad L_2 = \frac{L_b - L_a}{2} \tag{5.9}$$

– With magnetic coupling between coils:

$$L_1^{'} = \frac{L_a + L_b}{2}, \quad k = -\frac{L_b - L_a}{L_b + L_a} \tag{5.10}$$

In (5.9), a negative value for L_2 can arise if $L_b < L_a$. In this case, a magnetic coupling between the coils can be used to realize the section. In (5.10), a positive value for the coupling coefficient k means that the magnetic flows of both inductors combine. Otherwise, their magnetic flows are opposite.

In Fig. 5.3b, the position of the dots beside the inductors represents a positive value coupling coefficient, where the windings that form the inductors are wound in the same sense (clockwise-clockwise or counterclockwise-counterclockwise). By mirroring one of the inductors so that the dot appears on the other side, implies a change in the coupling coefficient signal, indicating that the inductors are now wound clockwise-counterclockwise to each other.

The first-order bridged-T section requires ideal coupling ($k = 1$), as shown in the left part of Fig. 5.3a. In a practical implementation, the second-order bridged-T section at the right part of Fig. 5.3a, with a coupling coefficient between 0.8 and 1, can be used to approximate a first-order section. The components values are given by [93]

$$C_1^{'} = \frac{C_a}{2}\frac{1-k}{1+k}, \quad L_1^{'} = \frac{L_a}{1+k}. \tag{5.11}$$

5.2 Design and Synthesis Examples

Different analog signal processing applications require filters with distinct group delay responses. For instance, a real-time Fourier transformer requires a linear response, while a spectrum sniffer requires a stepped response [2]. Aiming the realization of a real-time Fourier transform system, we present in this section two design examples: the first one of a lattice filter with a linear group delay of negative slope, and the second one of a bridge-T filter, also with a linear group delay, but of positive slope. In both examples, the specifications established for the prototype filters have the goal of maximizing the group delay swing and of approaching a perfect linear characteristic.

5.2.1 Lattice Network with Linear Group Delay of Negative Slope

We should start the design of the filter by prescribing a desired group delay characteristic. The general expression for the linear group delay of a prototype filter is given by

$$\tau_g(\Omega) = A\Omega + \tau_0, \tag{5.12}$$

where Ω is the normalized frequency, A is the angular coefficient (which reflects the magnitude of the slope and its orientation, positive or negative), and τ_0 is a constant term that should be suitably chosen so as to assure the realizability of the filter.

Table 5.1 – Poles and zeros of (5.14).

Section	Poles	Zeros
1	$-0.4808202 - j0.0282478$	$0.4808202 - j0.0282478$
	$-0.4808202 + j0.0282478$	$0.4808202 + j0.0282478$
2	$-0.5775816 - j0.5840440$	$0.5775816 - j0.5840440$
	$-0.5775816 + j0.5840440$	$0.5775816 + j0.5840440$

Since we were interested in a filter with a high magnitude negative slope group delay, we started by defining an order four for the filter and setting a value of -1 for the angular coefficient. Then, based on the procedures explained in Section 5.1.1, we experimented with several values for the constant term until we found a value that generated a stable (realizable) transfer function with a linear group delay characteristic. Accomplished this, we increased the magnitude of the angular coefficient and again searched for a value for the constant term that would allow us to generate a stable transfer function with a group delay characteristic as linear as possible. This iterative process was carried out until it was no longer possible to obtain a stable transfer function with a sufficiently linear group delay characteristic without having to increase the filter order. Finally, the expression obtained for the group delay of the prototype filter, and that was used in the filter design, was

$$\tau_g(\Omega) = -4\Omega + 6.09. \tag{5.13}$$

The transfer function of the all-pass prototype filter obtained through the above procedure is given by (5.14), and it can be factored into first- and second-order terms (the transfer function of each section of the filter).

$$\begin{aligned} S_{21}(s) &= \frac{P(s)}{E(s)} \\ &= \frac{s^4 - 2.1168s^3 + 2.0175s^2 - 0.91681s + 0.15652}{s^4 + 2.1168s^3 + 2.0175s^2 + 0.91681s + 0.15652} \\ &= \frac{s^2 - 0.96164s + 0.23199}{s^2 + 0.96164s + 0.23199} \cdot \frac{s^2 - 1.1552s + 0.67471}{s^2 + 1.1552s + 0.67471} \end{aligned} \tag{5.14}$$

The poles and zeros of the transfer function are given in Table 5.1 and are used to verify if the filter is stable (all poles must lie on the left half of the complex plane) and to determine the component values of the lattice network. Accordingly, Table 5.2 presents the values of the components of the prototype lattice filter obtained through (5.6), as well as the values for the components when this prototype network is scaled to a frequency of 3.5 GHz and an impedance of 50 ohms. Fig. 5.4a presents the filter schematic.

The group delay of each section of the lattice prototype filter is shown in Fig. 5.5, as well as the resultant group delay of the prototype filter. The pertinent frequency band is highlighted.

The scaled filter is implemented in STMicroelectronics BiCMOS9MW technology. The *cmim3p* metal-insulator-metal capacitor and the *indsym_lamw* planar inductor components of the technology were employed in the filter realization. The parameter values for the parameterized cells (PCells) are given in Table 5.3.

The forward transmission coefficient (S_{21}), the input reflection coefficient (S_{11}), and the group delay of the scaled filter are shown in Fig. 5.6. In the figure, the dotted line represents

Table 5.2 – Values of components for the prototype lattice filter and its respective scaled network to a frequency of 3.5 GHz and an impedance of 50 ohms.

	Prototype		**Scaled network**	
	Section 1	**Section 2**	**Section1**	**Section 2**
L_a	4.145 H	1.712 H	9.425 nH	3.893 nH
C_a	1.040 F	0.866 F	945.7 fF	787.3 fF
C_b	4.145 F	1.712 F	3.770 pF	1.557 pF
L_b	1.040 H	0.866 H	2.364 nH	1.968 nH

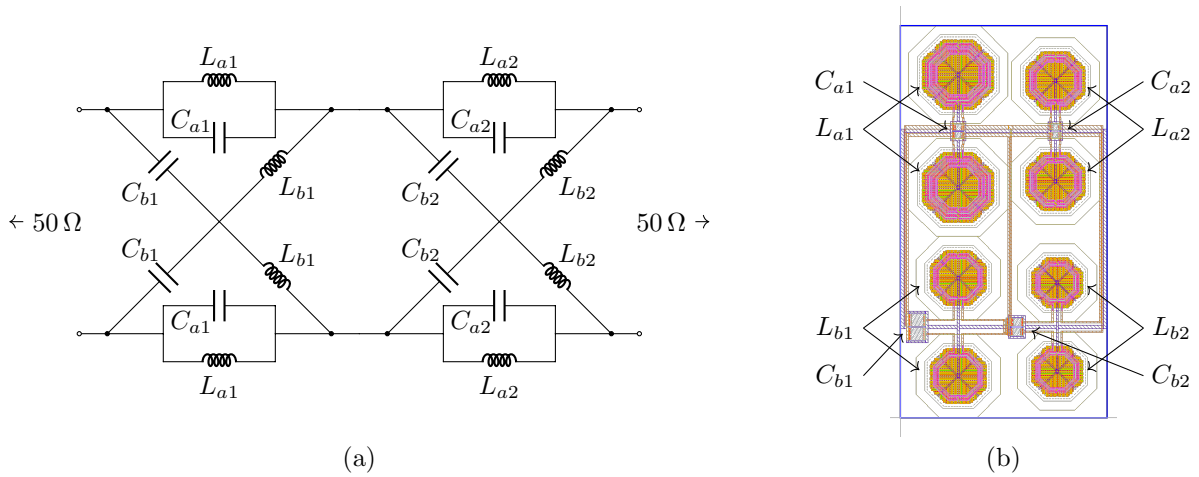

(a) (b)

Figure 5.4 – Lattice filter: (a) schematic (the values of components and PCell parameters are given in Tables 5.2 and 5.3, respectively), and (b) layout.

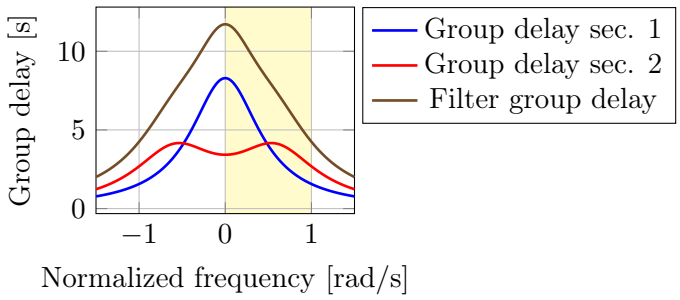

Figure 5.5 – Group delay of each all-pass section and the resultant prototype filter group delay characteristic, with the pertinent bandwidth highlighted.

Table 5.3 – Parameters values for the parameterized cells (PCells) used to realize the lattice filter.

	Internal diameter	**No. of turns**	**Metal width**		**Capacitance**	**Width**
			Section 1			
L_a	134.465 µm	6	5 µm	C_a	945.7 fF	21.5 µm
L_b	127.045 µm	3	5 µm	C_b	3.770 pF	43.123 µm
			Section 2			
L_a	123.57 µm	4	5 µm	C_a	787.3 fF	19.6 µm
L_b	108.935 µm	3	5 µm	C_b	1.557 pF	27.639 µm

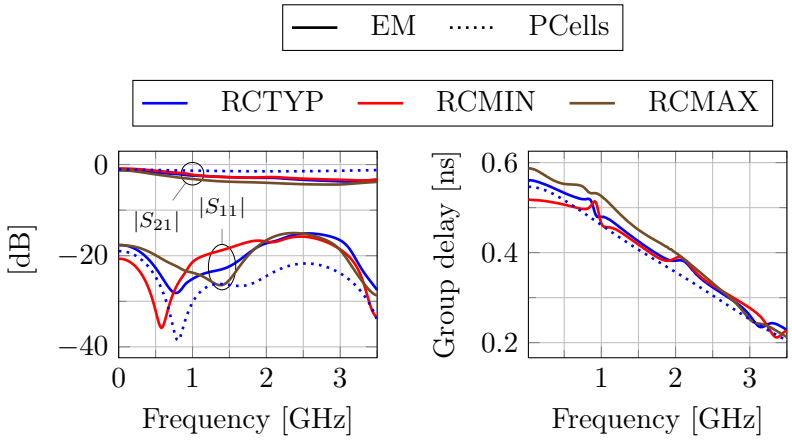

Figure 5.6 – Frequency response and group delay of the scaled lattice filter.

the simulation considering the components with modeled intrinsic parasitics, but not considering interconnect parasitics. The continuous lines are the result of a quasi-static electromagnetic (EM) simulations of the complete filter layout (post-layout), where the blue line (RCTYP) represents nominal conditions, and the red (RCMIN) and green (RCMAX) lines represent the best- and worst-case corners, respectively. The EM simulations were performed using the *Momentum* simulator of the *Keysight ADS 2019* EDA tool[94].

The filter presents a fairly linear group delay with a flat magnitude response. The maximum insertion loss is observed in the RCMAX corner and has a value of −4.38 dB at 2.9 GHz. The group delay swing ($\Delta\tau = \tau_{max} - \tau_{min}$) is higher than 300 ps for all corners, with the RCMIN corner presenting the smaller group delay slope, and the RCMAX presenting the biggest one. Since the characteristics for the group delays given by the EM simulations of the complete layout diverges from the perfect characteristic obtained in the SPICE simulation, it can be inferred from Fig. 5.6 that the imperfections in the linearity of the group delay are mainly due to interconnection parasitics.

To evaluate the deviation of the phase of the filter from its intended quadratic characteristic, we plot in Fig. 5.7a the absolute error (in degrees) of the phase to a second-order polynomial regression curve calculated from the quasi-static EM simulation data (200 points). Similarly, to

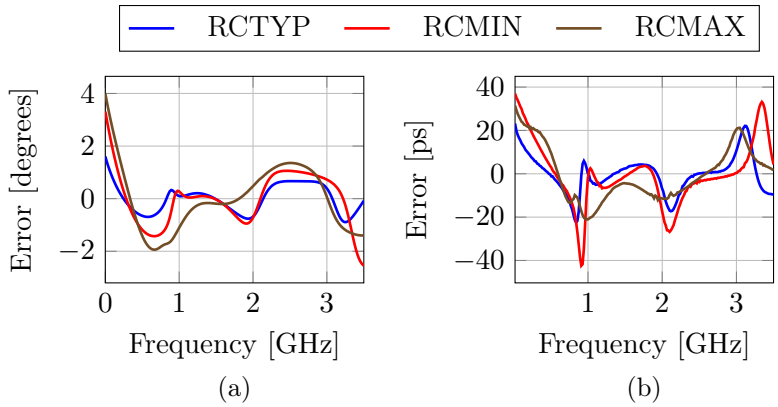

Figure 5.7 – (a) Error in the lattice filter phase with respect to a second order polynomial regression curve calculated from its quasi-static EM simulation curve (200 points) and (b) Error in the lattice filter group delay with respect to a linear regression line calculated from its quasi-static EM simulation curve (200 points).

evaluate the linearity of the group delay, we plot in Fig. 5.7b the absolute error (in picoseconds) of the group delay to a linear regression line calculated from the quasi-static EM simulation data (200 points). When working with linear phase filters, it is common to evaluate the flatness of the group delay through its relative error in percent. However, for a filter without a flat group delay, the relative error would be high in the band with a small delay, and small in the band with higher delay.

In Fig. 5.7, the peaks in the plots coincide with the visible imperfections in the characteristics of the group delays presented in Fig. 5.6. In the typical case (RCTYP), the phase error is smaller than one degree in practically the entire bandwidth, whereas, for the group delay, the error is smaller than twenty picoseconds, which represents around 6 % of the filter group delay swing.

As the filters have the property of being a constant-resistance network, they can be cascaded without the need for matching networks. The insertion loss and group delay of the resultant cascade will be equal to the accumulation of the insertion losses and group delays of the different filters that constitute it. To ensure proper power transfer and minimize signal reflection when cascading filters or connecting the filter to other circuits, it is imperative that the filter input and output impedances, respectively Z_{in} and Z_{out}, closely follow the reference impedance through all the passband, as in Fig. 5.8, where the deviation of the input and output impedances relative to the 50 ohms reference impedance is maintained within a range of ± 10 ohms along the major part of the passband at all corners.

Fig. 5.4 presents the lattice filter schematic and layout. The respective schematic components are indicated on the layout, and their values and PCell parameters are given in Tables 5.2 and 5.3, respectively. The layout dimensions are given in Table 5.8.

We summarize in Table 5.8 the major characteristics and performances in the state of the art of integrated filters with linear group delay. Except for the present work, all filters are composed of a cascade of distributed amplifier-based transversal filters. The distributed amplifiers (DAs) are composed of two filters interconnected by active devices. These two filters form the gate and drain lines of the DAs. A typical performance used to evaluate filters presenting linear group

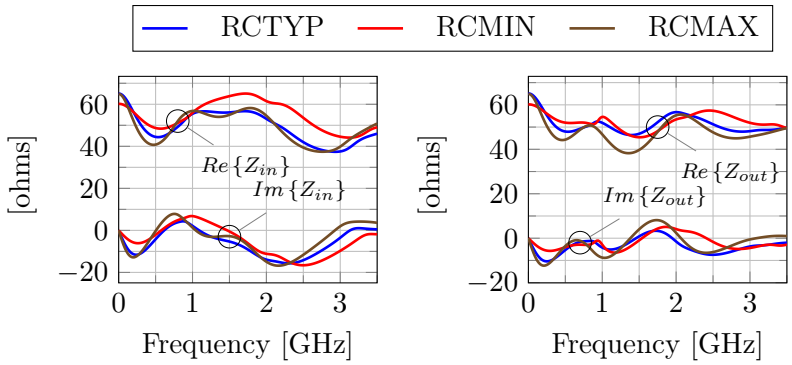

Figure 5.8 – Real and imaginary parts of the input and output impedances of the lattice filter in nominal conditions (RCTYP), and for the RCMIN and RCMAX corners.

delay is the time-bandwidth product (TBP or TBWP), consisting of the product of the filter group delay swing and bandwidth. As the filter group delay swing can be increased by increasing the filter order and/or by cascading filters, in an attempt to normalize and fairly compare the performance of the different filters, we divide its TBWP by the number of poles of the filter. From this, and thanks to the design method, it can be perceived that the designed lattice filter offers the higher TBWP per pole among all state of the art designs surveyed, while simultaneously presenting a flat magnitude response and fair group delay linearity.

5.2.2 Bridged-T Network with Linear Group Delay of Positive Slope

A second fourth-order all-pass filter was designed, but this time with a group delay presenting a positive slope. The group delay specification is the same as in Section 4.3 and is given by (5.15). Compared to (5.13), it is noticed that the present specification has a much smaller angular coefficient. This is because it is more difficult to obtain a perfectly linear characteristic for the group delay when it has a positive slope than when it has a negative slope. This fact had already been reported by Otto [12].

$$\tau_g(\Omega) = \Omega + 2.5 \tag{5.15}$$

For this specification, the filter transfer function obtained by applying the procedures of Section 5.1.1 is given by

$$\begin{aligned} S_{21}(s) &= \frac{P(s)}{E(s)} \\ &= \frac{s^4 - 2.1408s^3 + 3.1524s^2 - 2.3190s + 0.90249}{s^4 + 2.1408s^3 + 3.1524s^2 + 2.3190s + 0.90249} \\ &= \frac{s^2 - 0.88794s + 1.3912}{s^2 + 0.88794s + 1.3912} \cdot \frac{s^2 - 1.2529s + 0.64873}{s^2 + 1.2529s + 0.64873} \end{aligned} \tag{5.16}$$

with its poles and zeros given in Table 5.4.

Table 5.5 presents, in its upper part, the values of the components for a bridged-T prototype filter with no coupling between coils calculated through (5.8) and (5.9) and the respective values of components for the scaled prototype to a frequency of 3.5 GHz (the $\Omega = 1$ normalized frequency is mapped to a frequency of 3.5 GHz) and an impedance of 50 ohms. The bottom part of Table 5.5 displays the values of the components for a bridged-T prototype filter presenting coupling between

Table 5.4 – Poles and zeros of (5.16).

Section	Poles	Zeros
1	$-0.4439706 - j1.0927244$	$0.4439706 - j1.0927244$
	$-0.4439706 + j1.0927244$	$0.4439706 + j1.0927244$
2	$-0.6264393 - j0.5062667$	$0.6264393 - j0.5062667$
	$-0.6264393 + j0.5062667$	$0.6264393 + j0.5062667$

Table 5.5 – Values of components for: bridged-T prototype filters with and without coupling between coils; and their respective scaled networks (scaled to a frequency of 3.5 GHz and an impedance of 50 ohms).

	Bridged-T prototype		**Scaled bridged-T network**	
	Section 1	**Section 2**	**Section 1**	**Section 2**
Without coupling between coils ($k = 0$)				
C_1	0.563 F	0.399 F	512.1 fF	362.9 fF
L_1	0.638 H	1.931 H	1.451 nH	4.391 nH
L_2	0.244 H	−0.567 H	554.7 pH	−1.288 nH
C_2	1.277 F	3.863 F	1.161 pF	3.513 pF
With coupling between coils ($-1 \leq k \leq 1$ and $k \neq 0$)				
C_1	0.563 F	0.399 F	512.1 fF	362.9 fF
$L_1^{'}$	0.882 H	1.365 H	2.006 nH	3.103 nH
k	-0.277	0.415	-0.277	0.415
C_2	1.277 F	3.863 F	1.161 pF	3.513 pF

coils calculated with (5.8) and (5.10) and also the respective values of components for a bridged-T network scaled to the same frequency and impedance. For the filter that does not consider coupling between coils, section 2 of the filter presents a negative value for the inductance of L_2. That leads us to choose to implement this section through a network with a transformer (coupled inductors), which should exhibit a coupling factor of 0.415 between coils. Section 1 will be implemented through a network presenting no coupling between coils to avoid the burden of designing one more custom transformer. The filter was implemented using the same technology and PCells as the previous example, except for the custom transformer.

Fig. 5.9 plots the group delay of each section that composes the bridged-T prototype filter and the filter resulting group delay, highlighting the relevant operating band.

The transformer necessary to realize the section 2 of the bridged-T filter was designed using the *Coilsys* utility [95] of the *Keysight ADS 2019* EDA tool [94]. Its layout (cf. Fig. 5.11b) was then drawn in the *Cadence Virtuoso* platform [96], where an electromagnetic simulation was performed to reveal the same characteristics obtained with the *ADS* tool. The inductance (L), series resistance (Rs) and quality factor (Q) of the primary and secondary inductors of the transformer, as well as the mutual inductance (M) and the coupling coefficient (k) between the

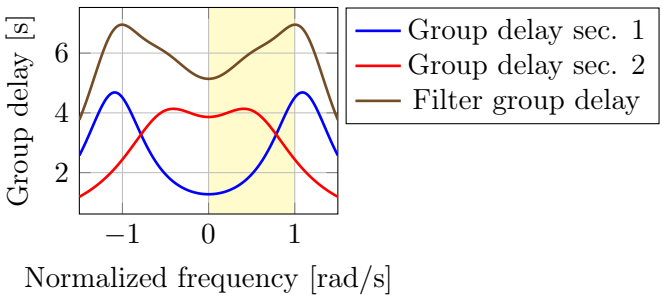

Figure 5.9 – Group delay of each all-pass section and the resultant characteristics of the prototype bridged-T filter group delay, with the pertinent bandwidth highlighted.

Table 5.6 – Designed transformer dimensions.

Line width	**Line space**	**Turns**	**Internal dimensions**
5 µm	40 µm	4	200/250 µm

inductors are shown in Fig. 5.10, and were obtained through the relations (5.17) - (5.21) [97–100], based on the data of the EM simulation of the testbench of Fig. 5.11a.

The self-resonant frequencies of the inductors are at about 7.9 GHz, too close to allow a constant inductance value, as can be verified in Fig. 5.10a. At the upper limit of the frequency band, the deviation in the inductance value from its ideal value of 3.103 nH is almost 13 %. The series resistance presented in Fig. 5.10b is significant, which results in a small quality factor (cf. Fig. 5.10c), despite the use of a thick metal line (3 µm) in parallel with the top aluminum cap available in the technology. The coupling coefficient deviates from its wanted value of 0.415 as the frequency increases, reaching a deviation of 15 % at the upper limit of the frequency band.

$$L_p = \frac{\mathrm{Im}\{Z_{11}\}}{2\pi f}, \quad L_s = \frac{\mathrm{Im}\{Z_{22}\}}{2\pi f} \tag{5.17}$$

$$Rs_p = \mathrm{Re}\{Z_{11}\}, \quad Rs_s = \mathrm{Re}\{Z_{22}\} \tag{5.18}$$

$$Q_p = \frac{\mathrm{Im}\{Z_{11}\}}{\mathrm{Re}\{Z_{11}\}}, \quad Q_s = \frac{\mathrm{Im}\{Z_{22}\}}{\mathrm{Re}\{Z_{22}\}} \tag{5.19}$$

$$M = \frac{\mathrm{Im}\{Z_{21}\}}{2\pi f} \tag{5.20}$$

$$k = -\frac{M}{\sqrt{L_p L_s}} = -\frac{\mathrm{Im}\{Z_{21}\}}{\sqrt{\mathrm{Im}\{Z_{11}\}\,\mathrm{Im}\{Z_{22}\}}} \tag{5.21}$$

A transformer with an interleaved structure and rectangular shape was implemented to ease the layout task. The dimensions of the designed transformer are given in Table 5.6.

The scaled bridged-T filter was implemented in the same technology using the same PCells used in the lattice example. The PCells parameter values are given in Table 5.7.

Fig. 5.12 presents the nominal quasi-static EM simulation as well as the RCMIN and RCMAX corners simulations for the forward transmission coefficient (S_{21}), the input reflection coefficient

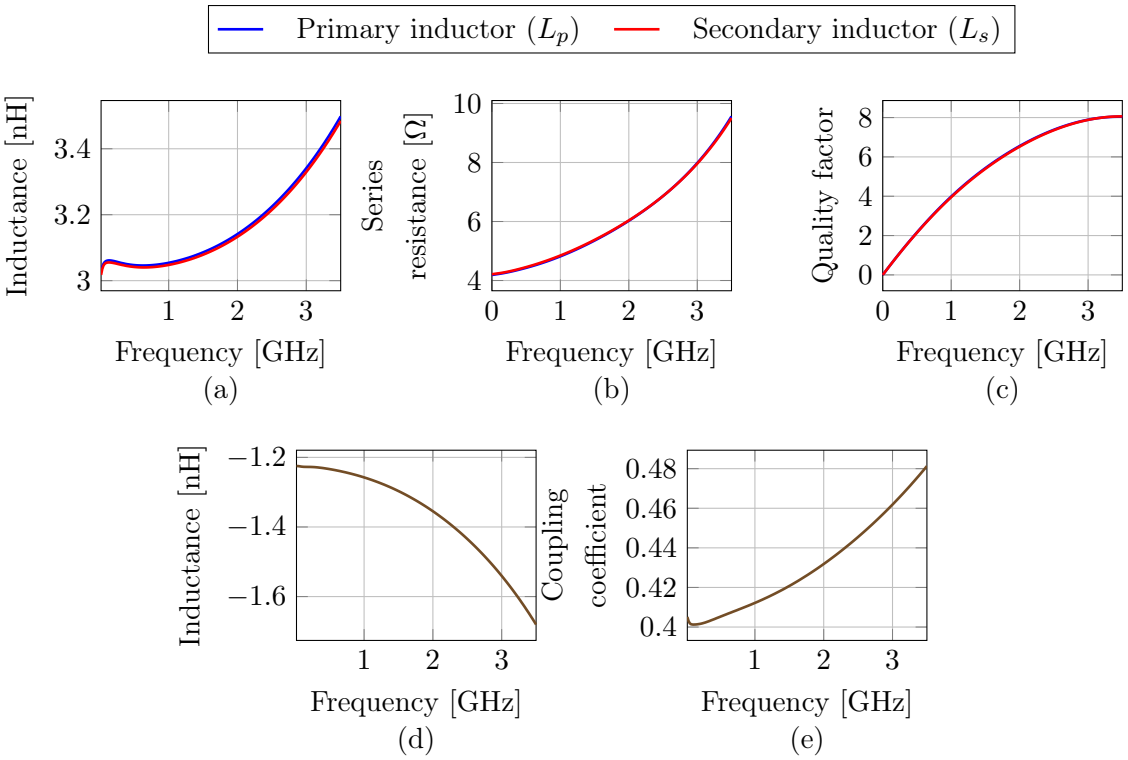

Figure 5.10 – Coupled inductors characteristics: (a) inductances, (b) series resistances, (c) quality factors, (d) mutual inductance, and (e) coupling coefficient.

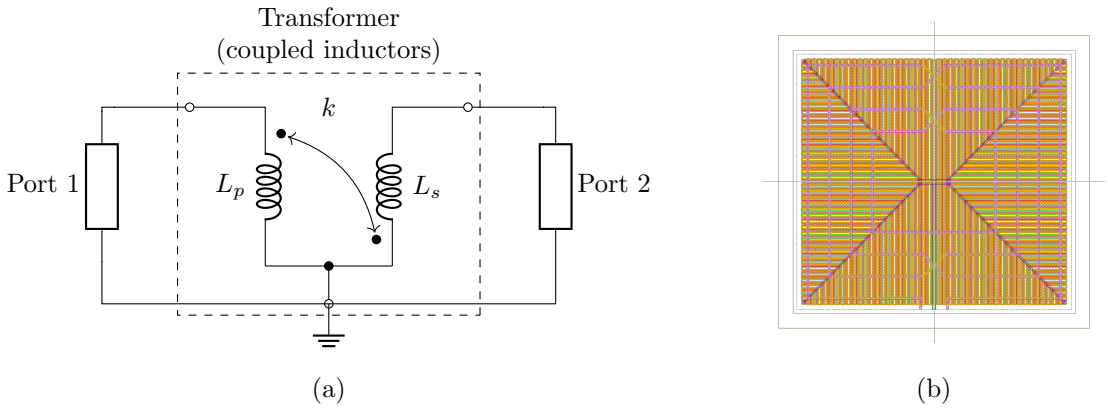

Figure 5.11 – Transformer: (a) transformer schematic and respective testbench for extracting the parameters exhibited in Fig. 5.10, (b) layout.

Table 5.7 – Parameters values of the components of the technology (PCells) for the bridged-T filter.

	Internal diameter	**No. of turns**	**Metal width**		**Capacitance**	**Width**
			Section 1			
L_1	84.145 µm	3	5 µm	C_1	512.1 fF	15.77 µm
L_2	69.945 µm	2	5 µm	C_2	1.161 pF	23.83 µm
			Section 2			
L_1'	refer to Table 5.6			C_1	362.9 fF	13.01 µm
				C_2	3.513 pF	40.3 µm

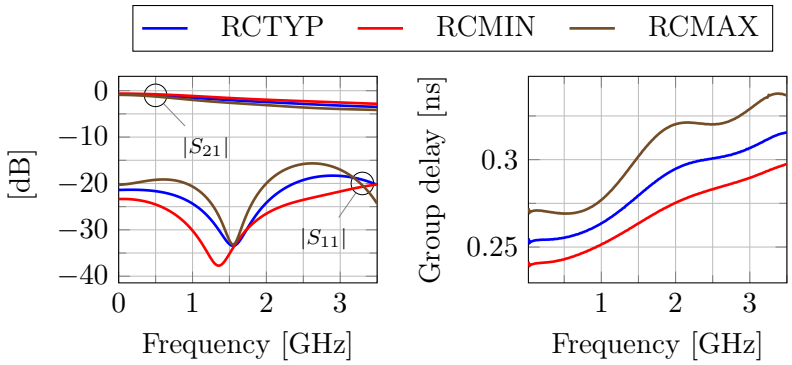

Figure 5.12 – Frequency response and group delay of the scaled bridged-T filter.

(S_{11}), and the group delay of the scaled bridged-T filter. As expected, the RCMIN corner presents the best frequency response and the most linear group delay as, in this case, the parasitics are minimized. The RCMAX corner displays the worst frequency response and group delay linearity, with the nominal RCTYP case in between the RCMIN and RCMAX performances. The insertion loss is better than −4.14 dB, observed at 3.5 GHz for the RCMAX corner, while the group delay swing is about 60 ps.

Fig. 5.13a plots, for the three corners (RCTYP, RCMIN, and RCMAX), the deviation (in degrees) of the phase of the filter from a second-order polynomial regression curve calculated from the quasi-static EM simulation data (200 points) representing the ideal quadratic phase characteristic. Fig. 5.13b, on its turn, plots the deviation (in picoseconds) of the group delay of the filter from a linear regression line calculated from the quasi-static EM simulation data (200 points) representing the idealized linear group delay. The phase deviation is smaller than 1.35 degrees for the RCMAX corner, and 0.5 degrees for the RCMIN corner, while the group delay deviates a maximum of 11.83 ps for the RCMAX corner and 3.38 ps for the RCMIN corner.

The real and imaginary parts of the input and output impedances of the bridged-T filter are plotted in Fig. 5.14. Similar to the lattice filter, the bridged-T filter input and output impedances are maintained within a range of about ±10 ohms around the reference impedance of 50 ohms for the major part of the passband at all corners. When cascading N filters, the group delay

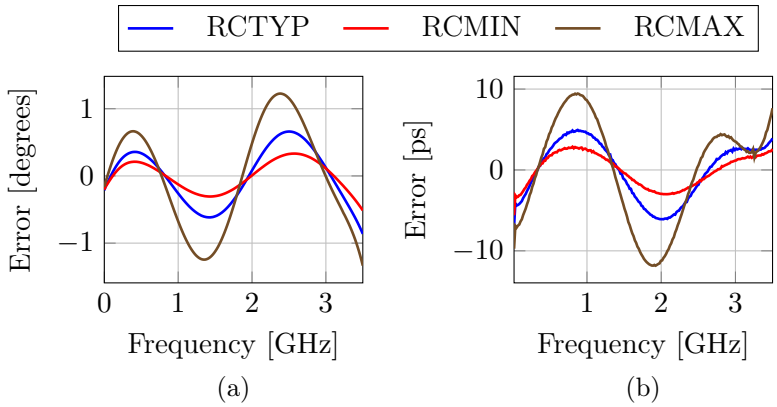

Figure 5.13 – (a) Error on the phase of the bridged-T filter related to a second-order polynomial regression curve calculated from its quasi-static EM simulation curve (200 points) and (b) Error on the group delay of the bridged-T filter related to a linear regression line calculated from its quasi-static EM simulation curve (200 points).

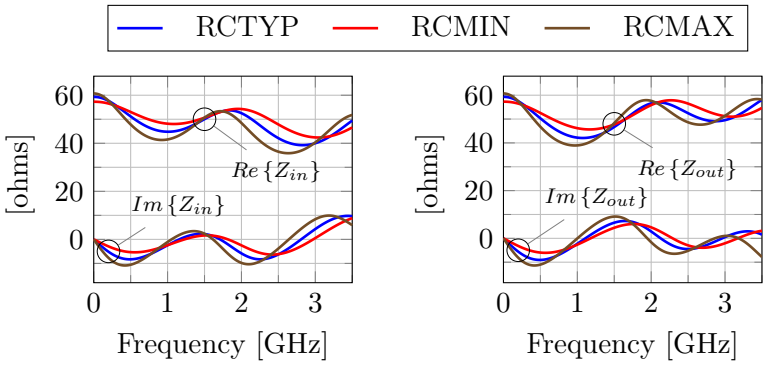

Figure 5.14 – Real and imaginary parts of the input and output impedances for the scaled bridged-T filter.

swing will be multiplied by N. As a side effect, the small mismatches between the cells may introduce non-linearities in the group delay characteristic. This problem must then be addressed in the layout.

Fig. 5.15 presents the bridged-T filter schematic and layout. The corresponding schematic components are indicated on the layout, and their values are given in Table 5.5, while the respective PCell technology parameters are presented in Table 5.7. The layout dimensions are given in Table 5.8.

In Table 5.8, that summarizes the principal characteristics and performances in the state of the art of integrated filters with linear group delay, we highlight that the designed lattice and bridged-T filters present, simultaneously, a fair group delay linearity with a flat magnitude response, besides being the first passive filters being reported.

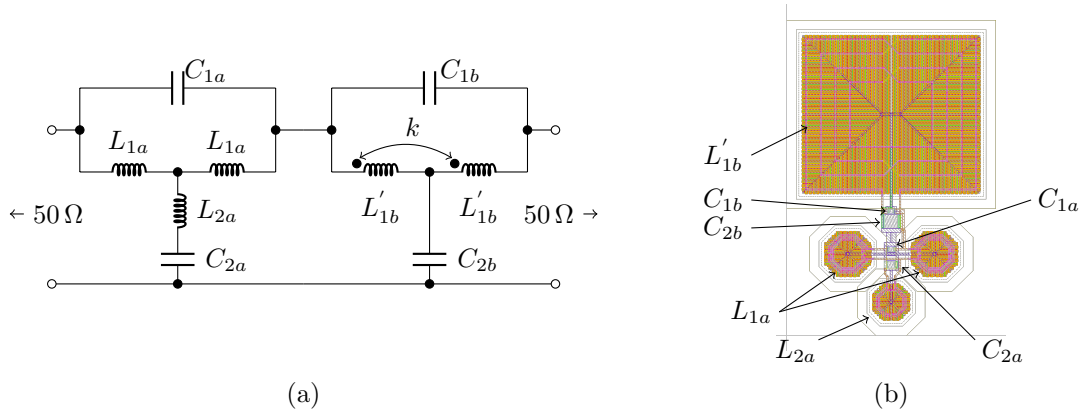

(a) (b)

Figure 5.15 – Bridged-T filter: (a) schematic (the values of components and PCell parameters are given in Tables 5.5 and 5.7, respectively), and (b) layout.

Table 5.8 – Comparison of state of the art integrated linear group delay filters.

	[37]	[38, 39]	[44]	[34]	**This work (lattice)**	**This work (bridged-T)**
Technology	0.13 µm CMOS	0.13 µm CMOS	0.13 µm CMOS	0.25 µm GaN MMIC	0.13 µm BiCMOS	
Area	7.05 mm^2	4.5 mm^2	16 mm^2	15.54 mm^2	0.92 mm^2 (without pads)	0.65 mm^2 (without pads)
Bandwidth	11–15 GHz	12–16 GHz	0.4–4 GHz	8–12 GHz	0–3.5 GHz	
Fractional bandwidth	31 %	29 %	164 %	40 %	200 %	
Group delay slope	positive	positive	negative	positive	negative	positive
Group delay swing	0.8 ns	1.5 ns	1.2 ns	0.6 ns	0.33 ns	60.6 ps
TBWP	3.2	6	5	2.4	1.155	0.212
Number of poles	30	30	44	40	4	4
TBWP/pole	0.107	0.200	0.114	0.060	0.289	0.053
Power consumption	active	active	750 mW	2.47 W	passive	passive
Group delay linearity	poor	poor	fair	poor	fair	fair
Gain flatness	poor	poor	poor	good	good	good

5.3 Active Filters

As previously mentioned, the method can be used as a basis for the creation of active filters. As an example, a balanced distributed amplifier based transversal filter was assembled based on the lattice filter designed in Section 5.2.1 and is shown in Fig. 5.16a. The assembled transversal filter is constituted by two instances of the designed lattice filter; one materializes the base line, while the other formes the collector line. Pseudo-differential pairs using the technology *npnvhs* high-speed bipolar transistor component were used as gain devices. The base and collector lines were biased to 0.8 V and 0.6 V, respectively, while the R_{ref} resistors were implemented through a 50 ohms *rpo1sab_rf* N+ salicided poly RF resistor component to match the constant resistance of the filter. Fig. 5.16b shows a similar filter but constructed with bridged-T sections and using generic gain devices, generally a common emitter or common source transistor.

Fig. 5.17 shows the frequency response of the assembled filter obtained through a SPICE simulation. Comparing with the dashed lines in Fig. 5.6, that represent the SPICE simulation of the passive filter, it can be seen that the active transversal filter presents a gain constrained between 4 dB and 6 dB, and the group delay presents ripple. The worsening in the linearity of

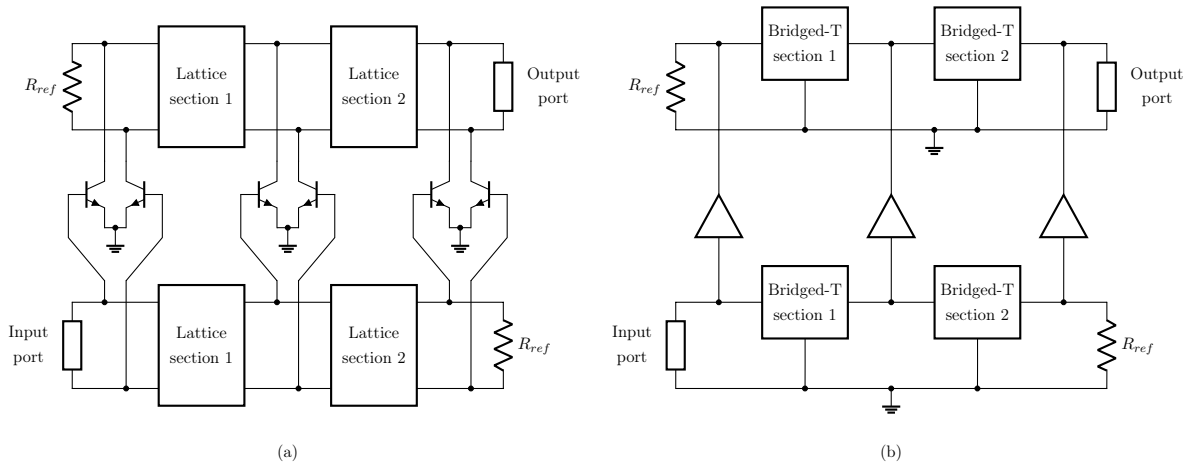

Figure 5.16 – Balanced distributed amplifier based transversal filter.

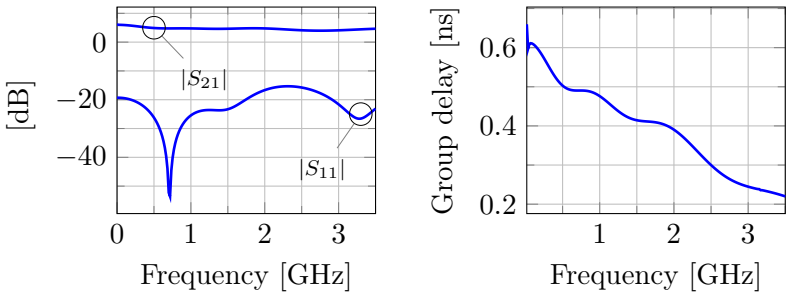

Figure 5.17 – Frequency response and group delay of the balanced distributed amplifier based transversal filter of Fig. 5.16a (SPICE simulation).

the group delay observed in the transversal filter characteristic is because the gain devices cause a bilateral coupling between the input and output networks [101] and add parasitics that were not taken on account in this simple assembling. A slight worsening in the reflection coefficient is also perceived due to the deterioration in the matching (between filter sections and between filter sections and terminating resistances) caused by the added parasitics. The parasitic should be evaluated and absorbed in the passive filter network to improve the performance of the filter.

5.4 Conclusion

This chapter presented a method for the design of all-pass filters with engineered group delay. The method is based on the generation of a transfer function for an all-pass prototype filter through a recursive procedure. From this transfer function, a suitable network can be synthesized. In this chapter, the method was used to design two constant-resistance all-pass filters with linear group delay, one with a negative slope group delay was synthesized through a balanced lattice network, and another with a positive slope group delay was synthesized through an unbalanced bridged-T network with coupled inductors. Both filters were implemented in the STMicroelectronics BiCMOS9MW 0.13 µm technology. Compared with state of the art in terms of integrated filters with linear group delay, the filters designed here presented better group delay linearity while

simultaneously maintaining a flat magnitude response. Lastly, it was shown that the designed filters could be used to assemble a transversal filter with a distributed amplifier structure.

Chapter 6

Conclusion

This thesis aimed to investigate systems capable of transforming ultra-wideband electronic signals from the time domain to the frequency domain. The ultimate goal is to facilitate the analysis and manipulation of these signals, thus contributing to meet the requirements of emerging applications that require processing power that exceeds the capacity of today's digital signal processing devices.

The work started by surveying the existing different analog systems capable of Fourier transforming ultra-wideband signals in real-time. Two categories of systems were identified: one that implements an analog version of the fast Fourier transform (FFT), and another that performs the finite Fourier transform (an analog version of the chirp Z-transform).

The architecture of an analog Fourier transformer suitable for real-time applications was developed based on this preliminary study. It can be described through two different but equivalent analytical models: a concise one, expressed in terms of complex exponentials, ideal for understanding the operating principle of the system; and a thorough one, given in terms of trigonometric functions, required for the physical implementation of the system. The models were derived in detail and allow the implementation of the various definitions of the (finite) Fourier transform.

The impact of errors inherent to practical systems was discussed, and the matching between the chirp filters and the chirp signals was confirmed to be the main concern for the correct operation of the transformer. Besides, an alternative scheme for the Fourier transformer was proposed to equalize the amplitude and resolution of the spectral components.

The proposed analog Fourier transformer architecture rely on filters with linear group delay to output a complex signal that is a time-domain representation of the input signal complex spectrum. At the transformer output, the two domains are mapped in one another through a linear relation given by the characteristic of chirp filters and signals used in the transformer.

The chirp filters form the core of the Fourier transformer and can also be used to generate the chirp signals needed in its operation. Because they are so important, much of this work has been devoted to the study of these unconventional filters, choosing to generalize the design method and diversify the network structures that can be synthesized to benefit other analog signal processing applications.

Methods for the design of different classes of filters (low-pass, band-pass, all-pass, etc.) and the synthesis of different network structures (ladder, lattice, bridged-T) were introduced. A

minimum-phase band-pass ladder filter with a positive slope linear group delay was designed in a 0.13 µm BiCMOS technology, but parasitic effects significantly impaired its characteristic. The same technology was used to implement two all-pass constant-resistance filters, a balanced lattice with a negative slope linear group delay, and an unbalanced bridged-T with a positive slope linear group delay. When compared to state of the art in integrated filters with linear group delay, these filters presented good linearity and a constant magnitude response through all the passband. The all-pass filters showed to be much more versatile than the ladder filter, since the formers can be easily cascaded to give rise to filters of higher-order and increased group delay slope.

6.1 Suggestions for Future Work

From the beginning, this thesis was concerned with introducing the architecture for a system that performs the finite Fourier transform and implementing it physically in an integrated circuit technology. Such a system, when analyzed using a high level of abstraction, may seem simple, but presents a complex structure that imposes a tough challenge to the designer wishing to implement it physically.

The present thesis advanced on the design of the basic block of this architecture, the chirp filter, a filter presenting a linear group delay. However, several difficulties still plague the designer wishing to implement the analog chirp Fourier transformer physically. Among them, the main ones concern the linearity of the group delay and the magnitude of the group delay swing. Chirp filters featuring extremely linear group delay characteristics have been previously reported, as well as SAW filters with group delay swing on the order of microseconds. However, none of these implementations were integrated. In an integrated realization, parasitics exert significant influence on the filter characteristic, making it difficult to obtain a linear group delay. Besides, integrated technologies are generally optimized to meet the requirements of low dispersion (flat group delay) in digital signal processing applications, which stands in opposition to the needs of analog signal processing.

Ways of improving the linearity of the group delay comprise laying out the filter structure in a way that the effect of some parasitics cancels out the effect of others, or to find a network structure more resilient to the influence of parasitics. This latter approach was explored in this thesis, where three different networks (ladder, lattice, and bridged-T) were used to implement chirp filters. A suggestion for future work would be to continue this exploration by implementing band-pass chirp filters through coupled (direct-coupled and multi-coupled) resonator structures. References [87, 102–108] discusses the design of direct-coupled resonator filters, while references [80, 109–113] refers to the design of multi-coupled (or cross-coupled) filters. It should be noted that coupled-resonator filters were initially limited to moderate bandwidth filters since the impedance and admittance inverters were generally considered frequency invariant [114]. By tanking on account the frequency-varying nature of the inverters, recent works have been able to synthesize wideband coupled-resonator filters successfully.

The design methods introduced in this thesis require specifying the group delay (or phase) characteristic of the prototype filter in its passband, that corresponds to the interval $[0, 1]$ of the normalized frequency domain. A recursive procedure is then employed to generate a phase

polynomial that constitutes the denominator polynomial of the filter transfer function. However, this recursive procedure is only capable of generating polynomials with real coefficients; this implies that the phase is an even function of frequency. As a consequence, when the low-pass prototype filter is converted into a band-pass filter, the upper half part of the passband of the band-pass filter will present the specified group delay characteristic, while the lower half part of the passband will present a mirrored characteristic. Besides that, the band-pass transformation will distort the group delay characteristic. To avoid these problems and use the full bandwidth of the band-pass filter, a solution would require that the phase be free from the constraint of being an odd function of frequency, which would imply that the coefficients of the transfer function could assume complex values [115]. The transfer function could be subsequently frequency translated[1] to the desired center frequency [17] and scaled in impedance and frequency. The resultant transfer function with complex coefficients could then be synthesized through cross-coupled networks. This solution would also double the group delay swing.

Regarding the exposed above, a suggestion would be to generalize the recursive procedure employed to generate the phase polynomial, that is a particular case of that given in [90], to enable the generation of polynomials with complex coefficients.

In Chapter 5, it was demonstrated that the lattice and bridged-T all-pass filters could be used as the basis for the creation of active (distributed amplifier-based) transversal filters. The frequency response obtained through SPICE simulation for a transversal filter based on the previously lattice all-pass filter was presented, but the filter was not further developed. The parasitics should be evaluated and absorbed by the filter components. By completing the development of this filter, it could be put together with the other passive filters designed in a top block, that could be sent to manufacturing. Measurements could then be made on the fabricated die to confirm the frequency and impulse responses of the filters.

As observed in [27], the amount of delay that devices based on electromagnetic waves can produce is much smaller than that based on acoustic waves. This difference is evident when comparing the filters designed in this thesis, based on LC components (i.e., inductors and capacitors), with that that employ SAW devices. However, it is proposed in [73] a loop scheme for increasing the group delay slope of a filter that eliminates the need for cascading multiple filters to achieve a significant group delay. An interesting experiment would be to use the previously mentioned distributed amplifier-based transversal filter to implement this scheme.

The above suggestions are all related with improvements in the design and realization of chirp filters and are intended to improve their characteristics and performances, such as improving the group delay linearity, increasing group delay swing and bandwidth, and reducing insertion loss. All suggestions contribute to facilitate and make possible the implementation of the proposed real-time analog chirp Fourier transformer (RTACFT) architecture. However, it was asserted in Section 3.4 that the mismatch between the characteristics of the chirp filters and chirp signals is the primary source of error in the proposed architecture. To mitigate this issue, it was proposed in [60] a control system to actively generate a chirp signal whose characteristics approach that of the chirp filter. The implementation of such a control system would greatly contribute to the physical realization of the proposed architecture and should be therefore considered.

[1] Frequency translate a transfer function with real coefficients results in a transfer function with complex coefficients.

6.2 Contributions

6.2.1 Articles Published in Conference Proceedings

- J. A. d. F. Ferreira, E. Avignon-Meseldzija, P. M. Ferreira, and P. Bénabès, "Design and synthesis of arbitrary group delay filters for integrated analog signal processing", in *Proc. 25th IEEE Int. Conf. Electron., Circuits and Syst.*, Bordeaux, France: IEEE, Dec. 2018, pp. 613–616, ISBN: 978-1-5386-9562-3. DOI: 10.1109/ICECS.2018.8617912

6.2.2 Journal Articles

- J. A. d. F. Ferreira, E. Avignon-Meseldzija, P. M. Ferreira, J. Sarrazin, and P. Bénabès, "Design of integrated all-pass filters with linear group delay for analog signal processing applications", *Int. J. Circ. Theor. Appl.*, (under major revision)

6.2.3 Other Articles Published in Conference Proceedings

- E. Avignon-Meseldzija, J. A. d. F. Ferreira, P. M. Ferreira, and P. Bénabès, "A compact active phaser with enhanced linearity of group delay for analog signal processing", in *14th Int. Conf. Advanced Technol., Syst. and Services in Telecommun.*, Niš, Serbia, 2019

Appendix A

Sinusoidal Complex Signals

A general sinusoidal complex signal can be expressed as

$$\begin{aligned} s(t) &= A(t)\, e^{j\phi(t)} = A(t)\left\{\cos\left[\phi(t)\right] + j\sin\left[\phi(t)\right]\right\} \\ &= A(t)\, e^{j\varphi(t)} = A(t)\left\{\cos\left[\varphi(t)\right] + j\sin\left[\varphi(t)\right]\right\}, \end{aligned} \tag{A.1}$$

where $A(t)$ is the amplitude of the signal, $\phi(t)$ is the instantaneous phase in radians, and $\varphi(t)$ the instantaneous phase in cycles. The instantaneous frequency of this signal is defined as the derivative (or rate of change) of its instantaneous phase, i.e.,

$$\omega(t) \triangleq \frac{d}{dt}\phi(t) \quad [\text{rad/s}] \tag{A.2}$$

$$f(t) \triangleq \frac{1}{2\pi}\frac{d}{dt}\varphi(t) \quad [\text{Hz}]. \tag{A.3}$$

A.1 Single-tone sinusoid

Knowing that the instantaneous frequency of a single-tone sinusoid is a constant value, and calling this value ω_0 when this frequency is expressed in radians per second, or f_0 when this frequency is expressed in hertz, the angle function can be found using (A.2) and (A.3).

$$\begin{aligned} \omega(t) = \omega_0 = \frac{d}{dt}\phi(t) \therefore \phi(t) &= \int_{-\infty}^{t} \omega(t)\, dt = \int_{-\infty}^{t} \omega_0\, dt \\ &\text{applying the integration by substitution method,} \\ &\text{making } t = \tau, \\ &= \int_{-\infty}^{t} \omega_0\, d\tau \\ &= \int_{-\infty}^{0} \omega_0\, d\tau + \int_{0}^{t} \omega_0\, d\tau \\ &= \phi_0 + \omega_0 t \quad [\text{rad}] \end{aligned} \tag{A.4}$$

$$
\begin{aligned}
f(t) = f_0 = \frac{1}{2\pi}\frac{d}{dt}\varphi(t) \therefore \varphi(t) &= 2\pi\int_{-\infty}^{t} f(t)\,dt = 2\pi\int_{-\infty}^{t} f_0\,dt \\
&\text{applying the integration by substitution method,} \\
&\text{making } t = \tau, \\
&= 2\pi\int_{-\infty}^{t} f_0\,d\tau \\
&= 2\pi\left(\int_{-\infty}^{0} f_0\,d\tau + \int_{0}^{t} f_0\,d\tau\right) \\
&= 2\pi(\varphi_0 + f_0 t) \quad \text{[cycles]}
\end{aligned}
\tag{A.5}
$$

At the above expressions, ϕ_0 and φ_0 are, respectively, the initial (at time $t = 0$) phase values in radians and cycles, also known as phase offsets.

Replacing the values of the obtained angle functions in (A.1), the analytical equations for the complex single tone sinusoid are obtained.

$$
\begin{aligned}
s(t) &= A(t)\,e^{j(\phi_0+\omega_0 t)} = A(t)\left[\cos(\phi_0+\omega_0 t) + j\sin(\phi_0+\omega_0 t)\right] \\
&= A(t)\,e^{j[2\pi(\varphi_0+f_0 t)]} = A(t)\left\{\cos\left[2\pi(\varphi_0+f_0 t)\right] + j\sin\left[2\pi(\varphi_0+f_0 t)\right]\right\}
\end{aligned}
\tag{A.6}
$$

A.2 Sinusoidal linear chirp

A chirp is a frequency modulated (FM) signal. When a frequency range is swept from a low to a high-frequency value, the signal is said to be an up-chirp. Conversely, if a frequency range is swept from a high to a low-frequency value, the signal is said to be a down-chirp.

By definition, a linear chirp has an instantaneous frequency that varies linearly with time. Thus, its angle function can be found using (A.2) and (A.3) through the subsequent development.

$$
\begin{aligned}
\omega(t) = \mu t + \omega_0 = \frac{d}{dt}\phi(t) \therefore \phi(t) &= \int_{-\infty}^{t} \omega(t)\,dt = \int_{-\infty}^{t} \mu t + \omega_0\,dt \\
&\text{applying the integration by substitution method,} \\
&\text{making } t = \tau, \\
&= \int_{-\infty}^{t} \mu\tau + \omega_0 d\tau \\
&= \int_{-\infty}^{0} \mu\tau + \omega_0 d\tau + \int_{0}^{t} \mu\tau + \omega_0 d\tau \\
&= \phi_0 + \frac{\mu}{2}t^2 + \omega_0 t \quad \text{[rad]}
\end{aligned}
\tag{A.7}
$$

$$
\begin{aligned}
f(t) = kt + f_0 = \frac{1}{2\pi}\frac{d}{dt}\varphi(t) \therefore \varphi(t) &= 2\pi\int_{-\infty}^{t} f(t)\,dt = 2\pi\int_{-\infty}^{t}(kt+f_0)\,dt \\
&\text{applying the integration by substitution method,} \\
&\text{making } t=\tau, \\
&= 2\pi\int_{-\infty}^{t} k\tau + f_0\,d\tau \\
&= 2\pi\left(\int_{-\infty}^{0} k\tau + f_0\,d\tau + \int_{0}^{t} k\tau + f_0\,d\tau\right) \\
&= 2\pi\left(\varphi_0 + \frac{k}{2}t^2 + f_0 t\right) \quad \text{[cycles]}
\end{aligned}
\tag{A.8}
$$

At the above expressions, μ and k are the rate of change of the frequency (or chirpiness) in rad/s^2 and cycles/s^2, respectively, and ω_0 and f_0 are the starting frequency (at time $t = 0$) in rad/s and Hz, respectively.

Due to the frequency variation produced by the time-varying instantaneous frequency function, chirp signals are considered frequency modulated signals.

In the same manner made for the single-tone sinusoid, replacing the value of the obtained angle function in (A.1), the analytical equation for the linear sinusoidal chirp is obtained.

$$
\begin{aligned}
s(t) &= A(t)\,e^{j\left(\phi_0+\frac{\mu}{2}t^2+\omega_0 t\right)} = A(t)\left[\cos\left(\phi_0+\frac{\mu}{2}t^2+\omega_0 t\right)+j\sin\left(\phi_0+\frac{\mu}{2}t^2+\omega_0 t\right)\right] \\
&= A(t)\,e^{j\left[2\pi\left(\varphi_0+\frac{k}{2}t^2+f_0 t\right)\right]} = A(t)\left\{\cos\left[2\pi\left(\varphi_0+\frac{k}{2}t^2+f_0 t\right)\right]\right. \\
&\qquad \left. +j\sin\left[2\pi\left(\varphi_0+\frac{k}{2}t^2+f_0 t\right)\right]\right\}
\end{aligned}
\tag{A.9}
$$

For a particular linear frequency sweep over a time T, starting at a frequency ω_0 or f_0, and ending in a frequency ω_1 or f_1, the rate of change of the frequency can be found through

$$
\omega(t) = \mu t + \omega_0 \therefore \mu = \frac{\omega(t)-\omega_0}{t} = \frac{\omega_1-\omega_0}{T} \quad \left[\text{rad/s}^2\right] \tag{A.10}
$$

$$
f(t) = kt + f_0 \therefore k = \frac{f(t)-f_0}{t} = \frac{f_1-f_0}{T} \quad \left[\text{cycles/s}^2\right] \tag{A.11}
$$

It is worth noting that several works (e.g., [3, 12, 26, 56]) use the exponential expressions of (A.12) and (A.13), that describe a baseband complex up-chirp, to define an up-chirp and a down-chirp, respectively. However, as can be noted by observing the relationships established by Euler's formula, (A.13) does not represent a down-chirp (cf. Fig. A.1). Actually, it just represents the complex conjugate of (A.12), and this means that imaginary parts of (A.12) and (A.13) have a phase difference of π radians (or 180 degrees). It is also impossible to represent a down-chirp with such expressions, as a positive finite frequency is required, represented by the linear term in the exponent, as in (A.9).

$$
e^{j\frac{\mu}{2}t^2} = \cos\left(\frac{\mu}{2}t^2\right) + j\sin\left(\frac{\mu}{2}t^2\right) \tag{A.12}
$$

$$
e^{-j\frac{\mu}{2}t^2} = \cos\left(\frac{\mu}{2}t^2\right) - j\sin\left(\frac{\mu}{2}t^2\right) \tag{A.13}
$$

Perhaps the confusion stems from the fact that (A.13) presents a quadratic phase with a negative concavity which, when derived to assess its instantaneous frequency, gives a straight line with a negative slope. However, evaluating this instantaneous frequency for positive instants of time results in negative values for the instantaneous frequency, which has no physical meaning. That is why in Fig. A.1, the absolute value of the instantaneous frequency is plotted, what is coherent.

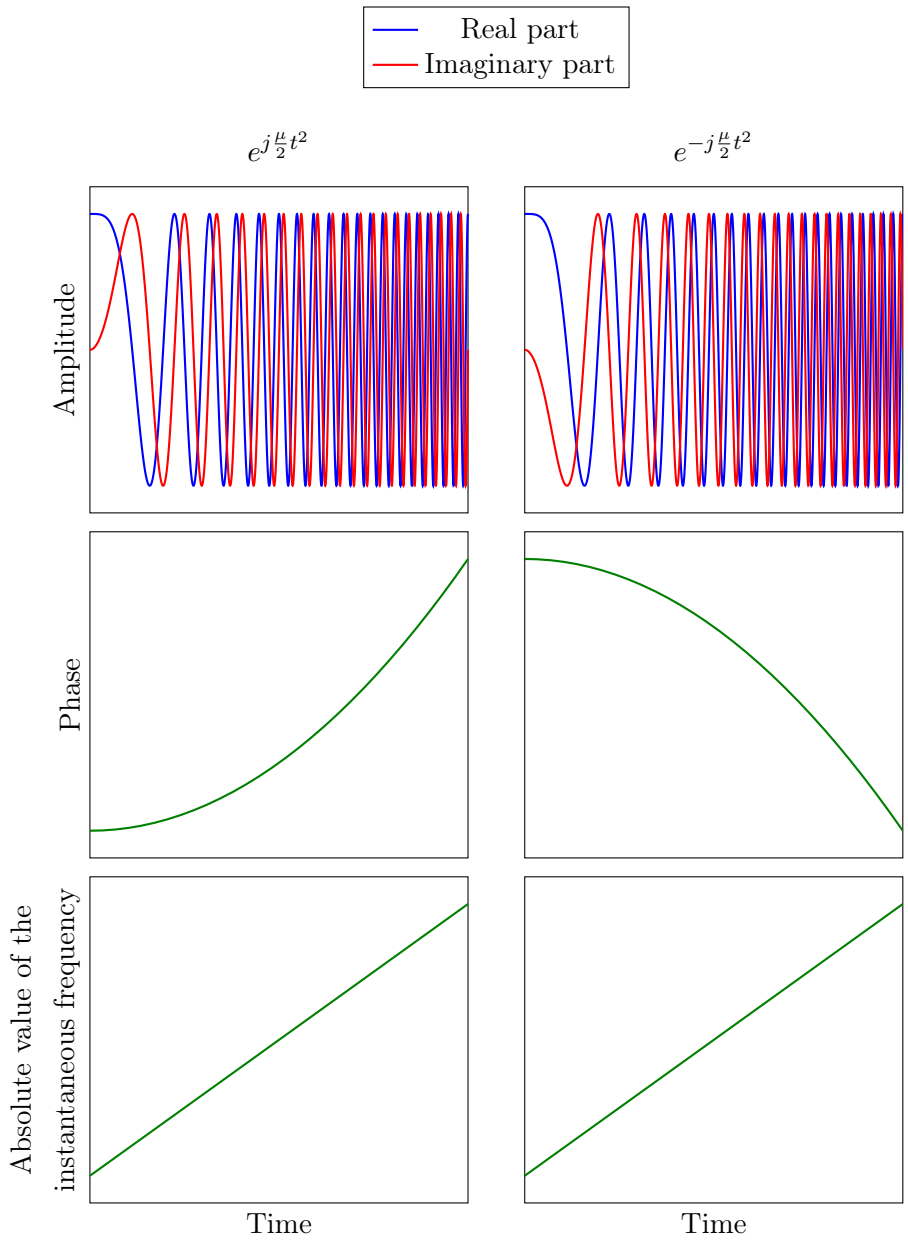

Figure A.1 – Waveforms for the linear sinusoidal complex up-chirp and its complex conjugate, and the absolute values of their instantaneous frequencies.

A.3 Generation of a chirp signal

As recalled above, Euler's relation establishes a relationship between a complex exponential and the cosine and sine functions. Thus, in practical terms, a complex signal can be represented by two real sinusoidal signals with a phase difference of ninety degrees.

A linear real chirp signal can be generated via a voltage controlled oscillator (VCO) or phase-locked loop (PLL), and a suitable (linear) control voltage [116]. At high frequencies, it can be challenging to generate the control voltage, while the PLL can present frequency stability problems. For the generation of high-frequency chirps, a linear delay versus frequency network[1] driven by a pulse modulated signal is preferred if it can operate at high frequencies. Another advantage of this implementation is that, in the case of applications that require matching between the chirp signal and the chirp filter, as in the case of compressive receivers, this match can be made optimum by using identical networks for the filter and the chirp generation [33].

The chirp signal can also be generated digitally by a digital signal processing (DSP) and a digital-to-analog converter (DAC), by employing direct digital synthesis (DDS) and varying the step in the numerically controlled oscillator. Nevertheless, this implementation demands intricate digital control electronics for the digital circuitry [117]. Another way to generate a chirp is through a yttrium iron garnet (YIG) oscillator [118].

A.4 Fourier transform of a linear sinusoidal chirp

A chirp—or frequency modulated (FM) signal—is a non-stationary signal, i.e., its spectral content changes with time. In general, the Fourier transform cannot be applied to analyze non-stationary signals. For such kind of signals, time-frequency analysis is generally employed to obtain, for example, a spectrogram. However, in the particular case of a constant amplitude linear chirp pulse, the Fourier transform can be applied to generate an analytical solution.

In the analysis that follows, the Fourier transform, as defined by (A.14), is used to obtain the frequency domain representation of a finite chirp (i.e., a chirp pulse). This chirp, defined by (A.15), has a duration T and an instantaneous frequency that varies linearly from a frequency f_1 to a frequency f_2. For convenience, the chirp is considered to have a constant unit amplitude.

$$\mathcal{F}\{f(t)\} = \int_{-\infty}^{\infty} f(t)\, e^{-j2\pi f t}\, dt \tag{A.14}$$

$$s_c(t) = [u(t) - u(t-T)]\, e^{j2\pi\left(\frac{k}{2}t^2 + f_1 t + \varphi\right)} = u(t)\, u(T-t)\, e^{j2\pi\left(\frac{k}{2}t^2 + f_1 t + \varphi\right)}, \tag{A.15}$$

where $u(t)$ is the unit step function, given by (A.16), and k is given by (A.17).

$$u(t) = \begin{cases} 0, & t < 0 \\ 1, & t \geqslant 0 \end{cases} \tag{A.16}$$

$$k = \frac{f_2 - f_1}{T}. \tag{A.17}$$

[1] A linear delay versus frequency network is a reciprocal device. This means that a $\frac{\sin(x)}{x}$ pulse can be fed through the network to produce a swept-frequency signal, or a linearly swept signal can produce a $\frac{\sin(x)}{x}$ pulse [7].

Evaluating (A.14) with (A.15):

$$\begin{aligned}\mathcal{F}\{s_c(t)\} &= \int_{-\infty}^{\infty} s_c(t)\, e^{-j2\pi ft}\, dt \\ &= \int_{-\infty}^{\infty} [u(t) - u(t-T)]\, e^{j2\pi\left(\frac{k}{2}t^2+f_1t+\varphi\right)} e^{-j2\pi ft}\, dt \\ &= \int_{-\infty}^{\infty} u(t)\, u(T-t)\, e^{j2\pi\left(\frac{k}{2}t^2+f_1t+\varphi\right)} e^{-j2\pi ft}\, dt \\ &= \int_{0}^{T} e^{j2\pi\left(\frac{k}{2}t^2+f_1t+\varphi\right)} e^{-j2\pi ft}\, dt \\ &= \int_{0}^{T} e^{j2\pi\left[\frac{k}{2}t^2+(f_1-f)t+\varphi\right]}\, dt.\end{aligned} \tag{A.18}$$

Completing the square,

$$\begin{aligned}\mathcal{F}\{s_c(t)\} &= \int_{0}^{T} e^{j2\pi\left\{\frac{k}{2}\left[t+\frac{1}{k}(f_1-f)\right]^2+\frac{1}{2}\left[2\varphi-\frac{1}{k}(f_1-f)^2\right]\right\}}\, dt \\ &= \int_{0}^{T} e^{j2\pi\left\{\frac{k}{2}\left[t+\frac{1}{k}(f_1-f)\right]^2\right\}} e^{j2\pi\left\{\frac{1}{2}\left[2\varphi-\frac{1}{k}(f_1-f)^2\right]\right\}}\, dt \\ &= e^{j2\pi\left\{\frac{1}{2}\left[2\varphi-\frac{1}{k}(f_1-f)^2\right]\right\}} \int_{0}^{T} e^{j2\pi\left\{\frac{k}{2}\left[t+\frac{1}{k}(f_1-f)\right]^2\right\}}\, dt.\end{aligned} \tag{A.19}$$

Changing variable,

$$\left[t+\frac{1}{k}(f_1-f)\right] = \frac{1}{\sqrt{2k}}x \tag{A.20}$$

$$dt = \frac{1}{\sqrt{2k}}dx \tag{A.21}$$

$$\begin{aligned}x &= \sqrt{2k}\left[t+\frac{1}{k}(f_1-f)\right] \\ &= \sqrt{2k}\left[\frac{kt+(f_1-f)}{k}\right] \\ &= \frac{\sqrt{2k}}{k}\left[kt+(f_1-f)\right] \\ &= \sqrt{\frac{2}{k}}\left[kt+(f_1-f)\right]\end{aligned} \tag{A.22}$$

Superior integration limit: $x_{sup} = \sqrt{\frac{2}{k}}\left[kT+(f_1-f)\right] = \sqrt{\frac{2}{k}}(f_2-f)$

Inferior integration limit: $x_{inf} = \sqrt{\frac{2}{k}}(f_1-f)$

$$\begin{aligned}\mathcal{F}\{s_c(t)\} &= e^{j2\pi\left\{\frac{1}{2}\left[2\varphi-\frac{1}{k}(f_1-f)^2\right]\right\}} \int_{\sqrt{\frac{2}{k}}(f_1-f)}^{\sqrt{\frac{2}{k}}(f_2-f)} e^{j2\pi\left\{\frac{k}{2}\left[\frac{1}{\sqrt{2k}}x\right]^2\right\}} \frac{1}{\sqrt{2k}}\, dx \\ &= \frac{1}{\sqrt{2k}} e^{j2\pi\left\{\frac{1}{2}\left[2\varphi-\frac{1}{k}(f_1-f)^2\right]\right\}} \int_{\sqrt{\frac{2}{k}}(f_1-f)}^{\sqrt{\frac{2}{k}}(f_2-f)} e^{j\frac{\pi}{2}x^2}\, dx.\end{aligned} \tag{A.23}$$

For an up-chirp, $k > 0$ and $x_{sup} \geqslant 0$ and $x_{inf} \leqslant 0$, as $f \leqslant f_2$ and $f \geqslant f_1$, respectively, enabling to rewrite the previous expression as

$$\begin{aligned}
\mathcal{F}\{s_c(t)\} &= \frac{1}{\sqrt{2k}} e^{j2\pi\left\{\frac{1}{2}\left[2\varphi - \frac{1}{k}(f_1-f)^2\right]\right\}} \left[\int_{\sqrt{\frac{2}{k}}(f_1-f)}^{0} e^{j\frac{\pi}{2}x^2}\, dx + \int_0^{\sqrt{\frac{2}{k}}(f_2-f)} e^{j\frac{\pi}{2}x^2}\, dx\right] \\
&= \frac{1}{\sqrt{2k}} e^{j2\pi\left\{\frac{1}{2}\left[2\varphi - \frac{1}{k}(f_1-f)^2\right]\right\}} \left[\int_0^{\sqrt{\frac{2}{k}}(f_2-f)} e^{j\frac{\pi}{2}x^2}\, dx - \int_0^{\sqrt{\frac{2}{k}}(f_1-f)} e^{j\frac{\pi}{2}x^2}\, dx\right] \\
&= \frac{1}{\sqrt{2k}} e^{j2\pi\left\{\frac{1}{2}\left[2\varphi - \frac{1}{k}(f_1-f)^2\right]\right\}} \left[Z\left(\sqrt{\frac{2}{k}}(f_2-f)\right) - Z\left(\sqrt{\frac{2}{k}}(f_1-f)\right)\right],
\end{aligned} \tag{A.24}$$

where[2]

$$Z(x) = C(x) + jS(x) = \int_0^x \cos\left(\frac{\pi}{2}\alpha^2\right)\, d\alpha + j\int_0^x \sin\left(\frac{\pi}{2}\alpha^2\right)\, d\alpha = \int_0^x e^{j\frac{\pi}{2}\alpha^2}\, d\alpha. \tag{A.25}$$

$$\begin{aligned}
\mathcal{F}\{s_c(t)\} &= \frac{1}{\sqrt{2k}} e^{j2\pi\left\{\frac{1}{2}\left[2\varphi - \frac{1}{k}(f_1-f)^2\right]\right\}} \left\{C\left(\sqrt{\frac{2}{k}}(f_2-f)\right) + jS\left(\sqrt{\frac{2}{k}}(f_2-f)\right)\right. \\
&\qquad \left. - \left[C\left(\sqrt{\frac{2}{k}}(f_1-f)\right) + jS\left(\sqrt{\frac{2}{k}}(f_1-f)\right)\right]\right\} \\
&= \frac{1}{\sqrt{2k}} e^{j2\pi\left\{\frac{1}{2}\left[2\varphi - \frac{1}{k}(f_1-f)^2\right]\right\}} \left\{C\left(\sqrt{\frac{2}{k}}(f_2-f)\right) - C\left(\sqrt{\frac{2}{k}}(f_1-f)\right)\right. \\
&\qquad \left. + j\left[S\left(\sqrt{\frac{2}{k}}(f_2-f)\right) - S\left(\sqrt{\frac{2}{k}}(f_1-f)\right)\right]\right\} \\
&= \frac{1}{\sqrt{2k}} e^{j2\pi\left\{\frac{1}{2}\left[2\varphi - \frac{1}{k}(f_1-f)^2\right]\right\}} \left\{C(x_{sup}) - C(x_{inf}) + j\left[S(x_{sup}) - S(x_{inf})\right]\right\} \\
&= \frac{1}{\sqrt{2k}} e^{j2\pi\left\{\frac{1}{2}\left[2\varphi - \frac{1}{k}(f_1-f)^2\right]\right\}} \\
&\qquad \sqrt{\left[C(x_{sup}) - C(x_{inf})\right]^2 + \left[S(x_{sup}) - S(x_{inf})\right]^2}\; e^{j\,\arctan\left[\frac{S(x_{sup}) - S\left(x_{inf}\right)}{C(x_{sup}) - C\left(x_{inf}\right)}\right]} \\
&= \frac{1}{\sqrt{2k}} \sqrt{\left[C(x_{sup}) - C(x_{inf})\right]^2 + \left[S(x_{sup}) - S(x_{inf})\right]^2} \\
&\qquad e^{j\left\{\pi\left[2\varphi - \frac{1}{k}(f_1-f)^2\right] + \arctan\left[\frac{S(x_{sup}) - S\left(x_{inf}\right)}{C(x_{sup}) - C\left(x_{inf}\right)}\right]\right\}}
\end{aligned} \tag{A.26}$$

[2] $Z(x)$ is named the complex Fresnel integral, while $C(x)$ and $S(x)$ are the real cosine and sine Fresnel integrals, respectively [119].

The above analytical expression, for the spectrum of a linear sinusoidal complex chirp, can be separated into three parts:

- the amplitude spectrum,

  $A(f) = \frac{1}{\sqrt{2k}} \sqrt{[C(x_{sup}) - C(x_{inf})]^2 + [S(x_{sup}) - S(x_{inf})]^2}$,

- a square-law phase term,

  $\Phi_1(f) = \pi \left[2\varphi - \frac{1}{k} (f_1 - f)^2 \right]$, and

- a residual phase term

  $\Phi_2(f) = \arctan \left[\frac{S(x_{sup}) - S(x_{inf})}{C(x_{sup}) - C(x_{inf})} \right]$

To illustrate the above results, we evaluate the transfer function of the linear sinusoidal complex chirp filter described in Section 3.3. Fig. A.2 plots the amplitude spectrum, the square law phase term, and the residual phase term of this filter, as well as its phase spectrum. The impulse response of the filter is expressed by (A.15), where the parameters f_1, f_2, and T are given by, 500 MHz, 3.5 GHz, and 100 ns, respectively.

The amplitude spectrum presents an approximately rectangular shape that approaches that of an ideal filter when the time-bandwidth product (TBWP) of the chirp increases. The value of the TBWP of a chirp is commonly associated with its spectrum shape [9, 75]. The referred filter presents a TBWP of 300, that represents a moderate value since SAW chirp filters with TBWP of several thousand have already been reported [56].

The residual phase presents an almost constant value of near 45 degrees (or $\frac{\pi}{4}$ radians) through all the frequency range swept by the chirp, starting to oscillate abruptly only outside this range. It can be verified, however, that for chirps with sufficiently high TBWP, the square law phase term dominates the residual phase term. This way, the chirp phase spectrum presents a quadratic characteristic in the frequency range swept by the chirp.

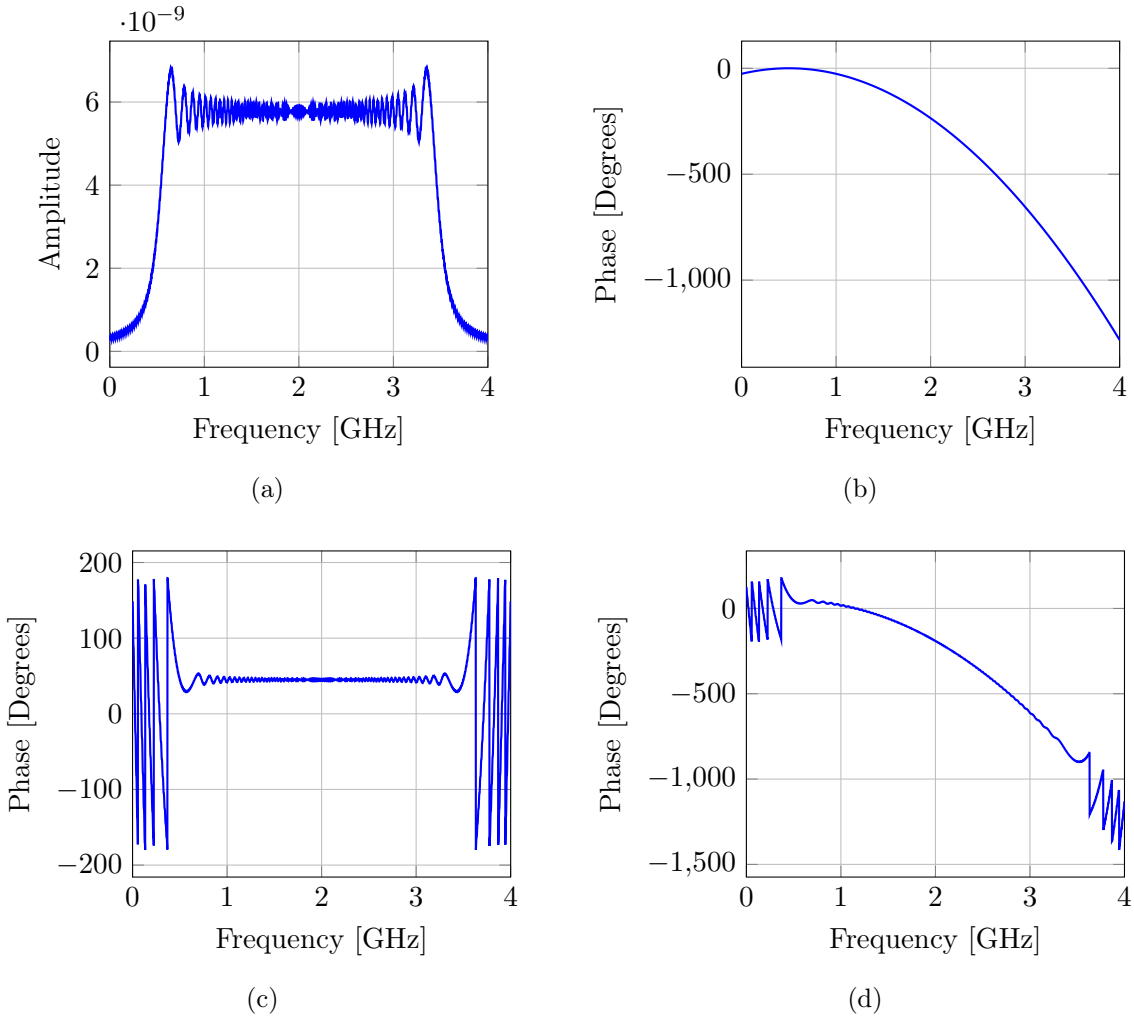

Figure A.2 – Linear sinusoidal chirp spectrum:(a) amplitude spectrum, (b) quadratic-law phase term, (c) residual phase term, (d) phase spectrum.

Appendix B

Detailed Derivation of the RTACFT System

Two models of the real-time analog chirp Fourier transformer (RTACFT) are detailed in this appendix. The first one, said to be of a high level of abstraction, is a compact version derived in terms of complex exponentials to ease the analysis of the system. The second one, said to be of a low level of abstraction, is derived in terms of real-valued functions, and is a prerequisite for a practical implementation of the system.

Both models are generalized so that all definitions of the Fourier transform, as defined in Appendix C, can be modeled.

B.1 High Abstraction Level Model

Fig. B.1 presents the block diagram for the RTACFT modeled in terms of complex-valued signals and a filter with a complex-valued impulse response. In the figure, $s_i(t)$ is the input signal to be Fourier transformed, $s_n(t)$ is a sinusoidal complex signal, $s_c(t)$ is a sinusoidal chirp complex signal, and $h(t)$ is the impulse response of the filter, that is equal to the complex conjugate of the chirp signal expression.

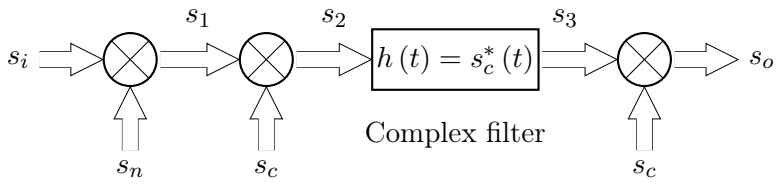

Figure B.1 – Block diagram of the RTACFT system in terms of complex-valued signals and a filter with a complex-valued impulse response.

B.1.1 Angular Frequency

In the derivation that follows, μ is the chirp rate of the filter in radians per second squared, ω_1 is both, the angular frequency of the complex sinusoid and the starting angular frequency of the chirp, ω_2 is the end angular frequency of the chirp, T is the amount of time that the chirp takes to sweep from its starting frequency to its end frequency (in seconds), and is equal to the

group delay swing ($\tau_{max} - \tau_{min}$) of the chirp filter, and ϕ is an arbitrary phase (in radians). For simplicity, all expressions are considered to have unitary amplitude.

$$s_n(t) = e^{\pm j(\omega_1 t + \phi)} \tag{B.1}$$

$$s_c(t) = e^{\mp j\left(\frac{\mu}{2}t^2 + \omega_1 t + \phi\right)}, \text{ where } \mu = \frac{\omega_2 - \omega_1}{T} \tag{B.2}$$

After the first multiplication,

$$\begin{aligned} s_1(t) &= s_i(t)\, s_n(t) \\ &= s_i(t)\, e^{\pm j(\omega_1 t + \phi)}. \end{aligned} \tag{B.3}$$

After the second multiplication,

$$\begin{aligned} s_2(t) = s_1(t)\, s_c(t) &= s_i(t)\, s_n(t)\, s_c(t) \\ &= s_i(t)\, e^{\pm j(\omega_1 t + \phi)} e^{\mp j\left(\frac{\mu}{2}t^2 + \omega_1 t + \phi\right)} \\ &= s_i(t)\, e^{\mp j\left(\frac{\mu}{2}t^2\right)}. \end{aligned} \tag{B.4}$$

The filter realizes a convolution in a finite time interval [120]. This is equivalent to multiplying both, the filter input signal, $s_2(t)$, and the filter impulse response, $h(t)$, by a unit step function, defined by

$$u(t) = \begin{cases} 1, & \text{if } t \geqslant 0 \\ 0, & \text{if } t < 0 \end{cases}. \tag{B.5}$$

Thus, the filter outputs

$$\begin{aligned} s_3(t) &= [s_2(t)\, u(t)] * [h(t)\, u(t)] \\ &= \int_{-\infty}^{\infty} s_2(\tau)\, u(\tau)\, h(t-\tau)\, u(t-\tau)\ d\tau \\ &= \int_0^t s_2(\tau)\, h(t-\tau)\ d\tau \\ &= \int_0^t s_i(\tau)\, e^{\mp j\left(\frac{\mu}{2}\tau^2\right)} e^{\pm j\left[\frac{\mu}{2}(t-\tau)^2 + \omega_1(t-\tau) + \phi\right]}\ d\tau \\ &= e^{\pm j\left(\frac{\mu}{2}t^2 + \omega_1 t + \phi\right)} \int_0^t s_i(\tau)\, e^{\mp j\omega(t)\tau}\ d\tau, \text{ where } \omega(t) = \mu t + \omega_1. \end{aligned} \tag{B.6}$$

After the third multiplication, the system outputs

$$\begin{aligned} s_o(t) &= s_3(t)\, s_c(t) \\ &= \left[e^{\pm j\left(\frac{\mu}{2}t^2 + \omega_1 t + \phi\right)} \int_0^t s_i(\tau)\, e^{\mp j\omega(t)\tau}\ d\tau\right] e^{\mp j\left(\frac{\mu}{2}t^2 + \omega_1 t + \phi\right)} \\ &= \int_0^t s_i(\tau)\, e^{\mp j\omega(t)\tau}\ d\tau, \text{ where } \omega(t) = \mu t + \omega_1. \end{aligned} \tag{B.7}$$

B.1.2 Ordinary Frequency

In the derivation that follows, k is the chirp rate of the filter in cycles per second squared, f_1 is both, the ordinary frequency of the complex sinusoid and the starting ordinary frequency of the chirp, f_2 is the end ordinary frequency of the chirp, T is the amount of time that the chirp

takes to sweep from its starting frequency to its end frequency (in seconds), and is equal to the group delay swing ($\tau_{max} - \tau_{min}$) of the chirp filter, and φ is an arbitrary phase (in cycles). For simplicity, all expressions are considered to have unitary amplitude.

$$s_n(t) = e^{\pm j2\pi(f_1 t+\varphi)} \tag{B.8}$$

$$s_c(t) = e^{\mp j2\pi\left(\frac{k}{2}t^2+f_1 t+\varphi\right)}, \text{ where } k = \frac{f_2 - f_1}{T} \tag{B.9}$$

After the first multiplication,

$$\begin{aligned} s_1(t) &= s_i(t)\, s_n(t) \\ &= s_i(t)\, e^{\pm j2\pi(f_1 t+\varphi)}. \end{aligned} \tag{B.10}$$

After the second multiplication,

$$\begin{aligned} s_2(t) = s_1(t)\, s_c(t) &= s_i(t)\, s_n(t)\, s_c(t) \\ &= s_i(t)\, e^{\pm j2\pi(f_1 t+\varphi)} e^{\mp j2\pi\left(\frac{k}{2}t^2+f_1 t+\varphi\right)} \\ &= s_i(t)\, e^{\mp j2\pi\left(\frac{k}{2}t^2\right)}. \end{aligned} \tag{B.11}$$

The filter realizes a convolution in a finite time interval [120]. This is equivalent to multiplying both, the filter input signal, $s_2(t)$, and the filter impulse response, $h(t)$, by a unit step function, defined by

$$u(t) = \begin{cases} 1, & \text{if } t \geqslant 0 \\ 0, & \text{if } t < 0 \end{cases}. \tag{B.12}$$

Thus, the filter outputs

$$\begin{aligned} s_3(t) &= [s_2(t)\, u(t)] * [h(t)\, u(t)] \\ &= \int_{-\infty}^{\infty} s_2(\tau)\, u(\tau)\, h(t-\tau)\, u(t-\tau)\ d\tau \\ &= \int_0^t s_2(\tau)\, h(t-\tau)\ d\tau \\ &= \int_0^t s_i(\tau)\, e^{\mp j2\pi\left(\frac{k}{2}\tau^2\right)} e^{\pm j2\pi\left[\frac{k}{2}(t-\tau)^2+f_1(t-\tau)+\varphi\right]}\ d\tau \\ &= e^{\pm j\left(\frac{k}{2}t^2+f_1 t+\varphi\right)} \int_0^t s_i(\tau)\, e^{\mp j2\pi f(t)\tau}\ d\tau, \text{ where } f(t) = kt + f_1. \end{aligned} \tag{B.13}$$

After the third multiplication, the system outputs

$$\begin{aligned} s_o(t) &= s_3(t)\, s_c(t) \\ &= \left[e^{\pm j\left(\frac{k}{2}t^2+f_1 t+\varphi\right)} \int_0^t s_i(\tau)\, e^{\mp j2\pi f(t)\tau}\ d\tau\right] e^{\mp j2\pi\left(\frac{k}{2}t^2+f_1 t+\varphi\right)} \\ &= \int_0^t s_i(\tau)\, e^{\mp j2\pi f(t)\tau}\ d\tau, \text{ where } f(t) = kt + f_1. \end{aligned} \tag{B.14}$$

B.2 Low Abstraction Level Model

Fig. B.2 presents the block diagram of the RTACFT modeled in terms of real-valued signals and filters with real-valued impulse responses. In the figure, $\mathrm{Re}\{\bullet\}$ and $\mathrm{Im}\{\bullet\}$ are the real and imaginary parts of $\bullet$, respectively, $s_i(t)$ is a real input signal to be Fourier transformed, $s_n(t)$ is a sinusoidal complex signal, $s_c(t)$ is a sinusoidal chirp complex signal, and $h_r(t)$ and $h_q(t)$ are, respectively, the impulse responses of real filters that are equal to the real and imaginary parts of the complex conjugate of the chirp signal expression.

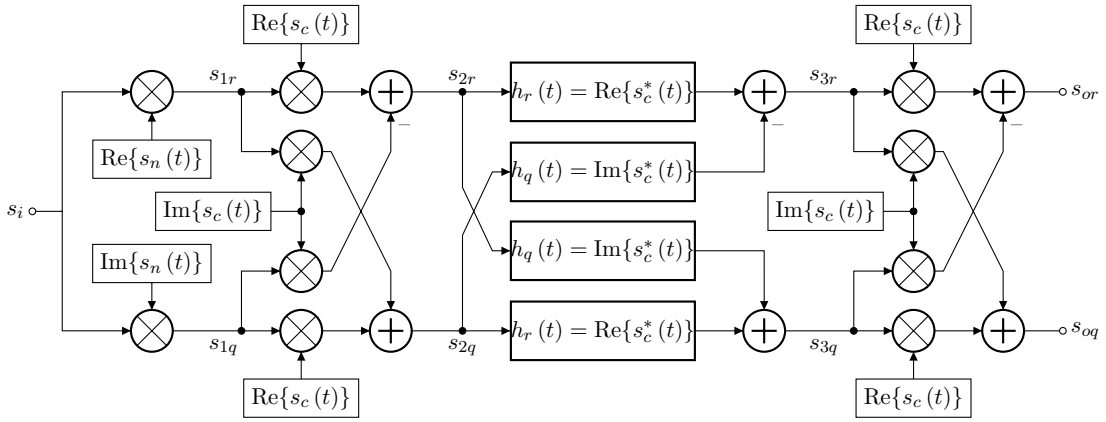

Figure B.2 – Block diagram of the RTACFT system in terms of real-valued signals and filters with real-valued impulse responses.

B.2.1 Angular Frequency

In the derivation that follows, μ is the chirp rate of the filter in radians per second squared, ω_1 is both, the angular frequency of the complex sinusoid and the starting angular frequency of the chirp, ω_2 is the end angular frequency of the chirp, T is the amount of time that the chirp takes to sweep from its starting frequency to its end frequency (in seconds), and is equal to the group delay swing ($\tau_{max} - \tau_{min}$) of the chirp filter, and ϕ is an arbitrary phase (in radians). For simplicity, all expressions are considered to have unitary amplitude.

$$s_n(t) = e^{\pm j(\omega_1 t + \phi)} \tag{B.15}$$

$$s_c(t) = e^{\mp j\left(\frac{\mu}{2}t^2 + \omega_1 t + \phi\right)}, \text{ where } \mu = \frac{\omega_2 - \omega_1}{T} \tag{B.16}$$

After the first (real-by-complex) multimplication,

$$s_{1r}(t) = s_i(t)\,\mathrm{Re}\{s_n(t)\} = s_i(t)\cos(\omega_1 t + \phi). \tag{B.17}$$

$$s_{1q}(t) = s_i(t)\,\mathrm{Im}\{s_n(t)\} = \pm s_i(t)\sin(\omega_1 t + \phi). \tag{B.18}$$

After the second (complex-by-complex) multiplication,

$$\begin{aligned}
s_{2r}(t) &= s_{1r}(t)\,\mathrm{Re}\{s_c(t)\} - s_{1q}(t)\,\mathrm{Im}\{s_c(t)\} \\
&= s_i(t)\cos(\omega_1 t+\phi)\cos\left(\frac{\mu}{2}t^2+\omega_1 t+\phi\right) \\
&\quad -\left[\pm s_i(t)\sin(\omega_1 t+\phi)\right]\left[\mp\sin\left(\frac{\mu}{2}t^2+\omega_1 t+\phi\right)\right] \\
&= s_i(t)\cos(\omega_1 t+\phi)\cos\left(\frac{\mu}{2}t^2+\omega_1 t+\phi\right) \\
&\quad +s_i(t)\sin(\omega_1 t+\phi)\sin\left(\frac{\mu}{2}t^2+\omega_1 t+\phi\right) \\
&= s_i(t)\left[\cos(\omega_1 t+\phi)\cos\left(\frac{\mu}{2}t^2+\omega_1 t+\phi\right)\right. \\
&\quad \left.+\sin(\omega_1 t+\phi)\sin\left(\frac{\mu}{2}t^2+\omega_1 t+\phi\right)\right]
\end{aligned} \tag{B.19}$$

Applying the following trigonometric identities:

$$\cos(\alpha)\cos(\beta) = \frac{1}{2}\cos(\alpha-\beta)+\frac{1}{2}\cos(\alpha+\beta) \tag{B.20}$$

$$\sin(\alpha)\sin(\beta) = \frac{1}{2}\cos(\alpha-\beta)-\frac{1}{2}\cos(\alpha+\beta) \tag{B.21}$$

$$\begin{aligned}
s_{2r}(t) &= s_i(t)\left\{\frac{1}{2}\cos\left[(\omega_1 t+\phi)-\left(\frac{\mu}{2}t^2+\omega_1 t+\phi\right)\right]\right. \\
&\qquad \cancel{+\frac{1}{2}\cos\left[(\omega_1 t+\phi)+\left(\frac{\mu}{2}t^2+\omega_1 t+\phi\right)\right]} \\
&\qquad +\frac{1}{2}\cos\left[(\omega_1 t+\phi)-\left(\frac{\mu}{2}t^2+\omega_1 t+\phi\right)\right] \\
&\qquad \left.\cancel{-\frac{1}{2}\cos\left[(\omega_1 t+\phi)+\left(\frac{\mu}{2}t^2+\omega_1 t+\phi\right)\right]}\right\} \\
&= s_i(t)\cos\left[(\omega_1 t+\phi)-\left(\frac{\mu}{2}t^2+\omega_1 t+\phi\right)\right] \\
&= s_i(t)\cos\left(\frac{\mu}{2}t^2\right).
\end{aligned} \tag{B.22}$$

$$\begin{aligned}
s_{2q}(t) &= s_{1q}(t)\,\mathrm{Re}\{s_c(t)\} + s_{1r}(t)\,\mathrm{Im}\{s_c(t)\} \\
&= \pm s_i(t)\sin(\omega_1 t+\phi)\cos\left(\frac{\mu}{2}t^2+\omega_1 t+\phi\right) \\
&\quad \mp s_i(t)\cos(\omega_1 t+\phi)\sin\left(\frac{\mu}{2}t^2+\omega_1 t+\phi\right) \\
&= s_i(t)\left[\pm\sin(\omega_1 t+\phi)\cos\left(\frac{\mu}{2}t^2+\omega_1 t+\phi\right)\right. \\
&\quad \left.\mp\cos(\omega_1 t+\phi)\sin\left(\frac{\mu}{2}t^2+\omega_1 t+\phi\right)\right]
\end{aligned} \tag{B.23}$$

Applying the following trigonometric identities:

$$\sin(\alpha)\cos(\beta) = \frac{1}{2}\sin(\alpha+\beta)+\frac{1}{2}\sin(\alpha-\beta) \tag{B.24}$$

$$\cos(\alpha)\sin(\beta) = \frac{1}{2}\sin(\alpha+\beta)-\frac{1}{2}\sin(\alpha-\beta) \tag{B.25}$$

$$
\begin{aligned}
s_{2q}(t) = s_i(t) \Bigg\{ & \cancel{\pm\frac{1}{2}\sin\left[(\omega_1 t+\phi)+\left(\frac{\mu}{2}t^2+\omega_1 t+\phi\right)\right]} \\
& \pm\frac{1}{2}\sin\left[(\omega_1 t+\phi)-\left(\frac{\mu}{2}t^2+\omega_1 t+\phi\right)\right] \\
& \cancel{\mp\frac{1}{2}\sin\left[(\omega_1 t+\phi)+\left(\frac{\mu}{2}t^2+\omega_1 t+\phi\right)\right]} \\
& \pm\frac{1}{2}\sin\left[(\omega_1 t+\phi)-\left(\frac{\mu}{2}t^2+\omega_1 t+\phi\right)\right] \Bigg\} \\
= & \pm s_i(t)\sin\left[(\omega_1 t+\phi)-\left(\frac{\mu}{2}t^2+\omega_1 t+\phi\right)\right] \\
= & \mp s_i(t)\sin\left(\frac{\mu}{2}t^2\right).
\end{aligned}
\tag{B.26}
$$

Each real filter realizes a convolution in a finite time interval [120]. This is equivalent to multiplying both, the filter input signal, $s_{2r}(t)$ or $s_{2q}(t)$, and the filter impulse response, $h_r(t)$ or $h_q(t)$, by a unit step function, defined by

$$
u(t) = \begin{cases} 1, & \text{if } t \geqslant 0 \\ 0, & \text{if } t < 0 \end{cases}. \tag{B.27}
$$

Thus, the outputs of the filters are

$$
\begin{aligned}
s_{3r}(t) &= [s_{2r}(t)\,u(t)] * [h_r(t)\,u(t)] - [s_{2q}(t)\,u(t)] * [h_q(t)\,u(t)] \\
&= \int_{-\infty}^{\infty} s_{2r}(\tau)\,u(\tau)\,h_r(t-\tau)\,u(t-\tau)\;d\tau \\
&\quad - \int_{-\infty}^{\infty} s_{2q}(\tau)\,u(\tau)\,h_q(t-\tau)\,u(t-\tau)\;d\tau \\
&= \int_0^t s_{2r}(\tau)\,h_r(t-\tau)\;d\tau - \int_0^t s_{2q}(\tau)\,h_q(t-\tau)\;d\tau \\
&= \int_0^t s_{2r}(\tau)\,h_r(t-\tau) - s_{2q}(\tau)\,h_q(t-\tau)\;d\tau \\
&= \int_0^t s_{2r}(\tau)\,\mathrm{Re}\{s_c^*(t-\tau)\} - s_{2q}(\tau)\,\mathrm{Im}\{s_c^*(t-\tau)\}\;d\tau \\
&= \int_0^t s_i(\tau)\cos\left(\frac{\mu}{2}\tau^2\right)\cos\left[\frac{\mu}{2}(t-\tau)^2+\omega_1(t-\tau)+\phi\right] \\
&\quad - \left[\mp s_i(\tau)\sin\left(\frac{\mu}{2}\tau^2\right)\right]\sin\left\{\pm\left[\frac{\mu}{2}(t-\tau)^2+\omega_1(t-\tau)+\phi\right]\right\}\;d\tau \\
&= \int_0^t s_i(\tau)\cos\left(\frac{\mu}{2}\tau^2\right)\cos\left[\frac{\mu}{2}(t-\tau)^2+\omega_1(t-\tau)+\phi\right] \\
&\quad + s_i(\tau)\sin\left(\frac{\mu}{2}\tau^2\right)\sin\left[\frac{\mu}{2}(t-\tau)^2+\omega_1(t-\tau)+\phi\right]\;d\tau
\end{aligned}
\tag{B.28}
$$

Applying the following trigonometric identities:

$$
\cos(\alpha)\cos(\beta) = \frac{1}{2}\cos(\alpha-\beta) + \frac{1}{2}\cos(\alpha+\beta) \tag{B.29}
$$

$$
\sin(\alpha)\sin(\beta) = \frac{1}{2}\cos(\alpha-\beta) - \frac{1}{2}\cos(\alpha+\beta) \tag{B.30}
$$

$$
\begin{aligned}
s_{3r}(t) = & \int_0^t \frac{1}{2} s_i(\tau) \cos\left\{\left(\frac{\mu}{2}\tau^2\right) - \left[\frac{\mu}{2}(t-\tau)^2 + \omega_1(t-\tau) + \phi\right]\right\} \\
& \cancel{+\frac{1}{2} s_i(\tau) \cos\left\{\left(\frac{\mu}{2}\tau^2\right) + \left[\frac{\mu}{2}(t-\tau)^2 + \omega_1(t-\tau) + \phi\right]\right\}} \\
& + \frac{1}{2} s_i(\tau) \cos\left\{\left(\frac{\mu}{2}\tau^2\right) - \left[\frac{\mu}{2}(t-\tau)^2 + \omega_1(t-\tau) + \phi\right]\right\} \\
& \cancel{-\frac{1}{2} s_i(\tau) \cos\left\{\left(\frac{\mu}{2}\tau^2\right) + \left[\frac{\mu}{2}(t-\tau)^2 + \omega_1(t-\tau) + \phi\right]\right\}} \, d\tau \\
= & \int_0^t s_i(\tau) \cos\left(\frac{\mu}{2}\tau^2\right) - 2\pi\left[\frac{\mu}{2}(t-\tau)^2 + \omega_1(t-\tau) + \phi\right] \, d\tau \\
= & \int_0^t s_i(\tau) \cos\left[\frac{\mu}{2}\tau^2 - \frac{\mu}{2}(t-\tau)^2 - \omega_1(t-\tau) - \phi\right] \, d\tau \\
= & \int_0^t s_i(\tau) \cos\left(\cancel{\frac{\mu}{2}\tau^2} - \frac{\mu}{2}t^2 + \mu t\tau - \cancel{\frac{\mu}{2}\tau^2} - \omega_1 t + \omega_1\tau - \phi\right) \, d\tau \\
= & \int_0^t s_i(\tau) \cos\left[(\mu t + \omega_1)\tau - \left(\frac{\mu}{2}t^2 + \omega_1 t + \phi\right)\right] \, d\tau
\end{aligned}
\tag{B.31}
$$

Applying the following trigonometric identity:

$$
\cos(\alpha \pm \beta) = \cos(\alpha)\cos(\beta) \mp \sin(\alpha)\sin(\beta) \tag{B.32}
$$

$$
\begin{aligned}
s_{3r}(t) = & \int_0^t s_i(\tau) \Big\{\cos\left[(\mu t + \omega_1)\tau\right] \cos\left(\frac{\mu}{2}t^2 + \omega_1 t + \phi\right) \\
& \qquad + \sin\left[(\mu t + \omega_1)\tau\right] \sin\left(\frac{\mu}{2}t^2 + \omega_1 t + \phi\right)\Big\} \, d\tau \\
= & \cos\left(\frac{\mu}{2}t^2 + \omega_1 t + \phi\right) \int_0^t s_i(\tau) \cos\left[(\mu t + \omega_1)\tau\right] \, d\tau \\
& + \sin\left(\frac{\mu}{2}t^2 + \omega_1 t + \phi\right) \int_0^t s_i(\tau) \sin\left[(\mu t + \omega_1)\tau\right] \, d\tau.
\end{aligned}
\tag{B.33}
$$

$$
\begin{aligned}
s_{3q}(t) &= [s_{2q}(t)\,u(t)] * [h_r(t)\,u(t)] + [s_{2r}(t)\,u(t)] * [h_q(t)\,u(t)] \\
&= \int_{-\infty}^{\infty} s_{2q}(\tau)\,u(\tau)\,h_r(t-\tau)\,u(t-\tau)\;d\tau \\
&\quad + \int_{-\infty}^{\infty} s_{2r}(\tau)\,u(\tau)\,h_q(t-\tau)\,u(t-\tau)\;d\tau \\
&= \int_0^t s_{2q}(\tau)\,h_r(t-\tau)\;d\tau + \int_0^t s_{2r}(\tau)\,h_q(t-\tau)\;d\tau \\
&= \int_0^t s_{2q}(\tau)\,h_r(t-\tau) + s_{2r}(\tau)\,h_q(t-\tau)\;d\tau \\
&= \int_0^t s_{2q}(\tau)\,\mathrm{Re}\{s_c^*(t-\tau)\} + s_{2r}(\tau)\,\mathrm{Im}\{s_c^*(t-\tau)\}\;d\tau \\
&= \int_0^t \mp s_i(\tau)\sin\left(\frac{\mu}{2}\tau^2\right)\cos\left[\frac{\mu}{2}(t-\tau)^2+\omega_1(t-\tau)+\phi\right] \\
&\qquad + s_i(\tau)\cos\left(\frac{\mu}{2}\tau^2\right)\sin\left\{\pm\left[\frac{\mu}{2}(t-\tau)^2+\omega_1(t-\tau)+\phi\right]\right\}\;d\tau \\
&= \int_0^t \mp s_i(\tau)\sin\left(\frac{\mu}{2}\tau^2\right)\cos\left[\frac{\mu}{2}(t-\tau)^2+\omega_1(t-\tau)+\phi\right] \\
&\qquad \pm s_i(\tau)\cos\left(\frac{\mu}{2}\tau^2\right)\sin\left[\frac{\mu}{2}(t-\tau)^2+\omega_1(t-\tau)+\phi\right]\;d\tau
\end{aligned}
\tag{B.34}
$$

Applying the following trigonometric identities:

$$\sin(\alpha)\cos(\beta) = \frac{1}{2}\sin(\alpha+\beta) + \frac{1}{2}\sin(\alpha-\beta) \tag{B.35}$$

$$\cos(\alpha)\sin(\beta) = \frac{1}{2}\sin(\alpha+\beta) - \frac{1}{2}\sin(\alpha-\beta) \tag{B.36}$$

$$
\begin{aligned}
s_{3q}(t) = \int_0^t & \cancel{\mp\frac{1}{2}s_i(\tau)\sin\left\{\left(\frac{\mu}{2}\tau^2\right)+\left[\frac{\mu}{2}(t-\tau)^2+\omega_1(t-\tau)+\phi\right]\right\}} \\
& \mp\frac{1}{2}s_i(\tau)\sin\left\{\left(\frac{\mu}{2}\tau^2\right)-\left[\frac{\mu}{2}(t-\tau)^2+\omega_1(t-\tau)+\phi\right]\right\} \\
& \cancel{\pm\frac{1}{2}s_i(\tau)\sin\left\{\left(\frac{\mu}{2}\tau^2\right)+\left[\frac{\mu}{2}(t-\tau)^2+\omega_1(t-\tau)+\phi\right]\right\}} \\
& \mp\frac{1}{2}s_i(\tau)\sin\left\{\left(\frac{\mu}{2}\tau^2\right)-\left[\frac{\mu}{2}(t-\tau)^2+\omega_1(t-\tau)+\phi\right]\right\}\;d\tau \\
= \mp & \int_0^t s_i(\tau)\sin\left\{\left(\frac{\mu}{2}\tau^2\right)-\left[\frac{\mu}{2}(t-\tau)^2+\omega_1(t-\tau)+\phi\right]\right\}\;d\tau \\
= \mp & \int_0^t s_i(\tau)\sin\left[\frac{\mu}{2}\tau^2-\frac{\mu}{2}(t-\tau)^2-\omega_1(t-\tau)-\phi\right]\;d\tau \\
= \mp & \int_0^t s_i(\tau)\sin\left(\cancel{\frac{\mu}{2}\tau^2}-\frac{\mu}{2}t^2+\mu t\tau\cancel{-\frac{\mu}{2}\tau^2}-\omega_1 t+\omega_1\tau-\phi\right)\;d\tau \\
= \mp & \int_0^t s_i(\tau)\sin\left[(\mu t+\omega_1)\tau-\left(\frac{\mu}{2}t^2+\omega_1 t+\phi\right)\right]\;d\tau
\end{aligned}
\tag{B.37}
$$

Applying the following trigonometric identity:

$$\sin(\alpha\pm\beta) = \sin(\alpha)\cos(\beta)\pm\cos(\alpha)\sin(\beta) \tag{B.38}$$

$$
\begin{aligned}
s_{3q}(t) &= \mp \int_0^t s_i(\tau) \Big\{ \sin\left[(\mu t + \omega_1)\tau\right] \cos\left(\frac{\mu}{2}t^2 + \omega_1 t + \phi\right) \\
&\qquad - \cos\left[(\mu t + \omega_1)\tau\right] \sin\left(\frac{\mu}{2}t^2 + \omega_1 t + \phi\right) \Big\} \; d\tau \\
&= \mp \cos\left(\frac{\mu}{2}t^2 + \omega_1 t + \phi\right) \int_0^t s_i(\tau) \sin\left[(\mu t + \omega_1)\tau\right] \; d\tau \\
&\quad \pm \sin\left(\frac{\mu}{2}t^2 + \omega_1 t + \phi\right) \int_0^t s_i(\tau) \cos\left[(\mu t + \omega_1)\tau\right] \; d\tau.
\end{aligned}
\tag{B.39}
$$

After the third multiplication, the system outputs

$$
\begin{aligned}
s_{or}(t) &= s_{3r}(t)\,\mathrm{Re}\{s_c(t)\} - s_{3q}(t)\,\mathrm{Im}\{s_c(t)\} \\
&= \Big\{ \cos\left(\frac{\mu}{2}t^2 + \omega_1 t + \phi\right) \int_0^t s_i(\tau) \cos\left[(\mu t + \omega_1)\tau\right] \; d\tau \\
&\quad + \sin\left(\frac{\mu}{2}t^2 + \omega_1 t + \phi\right) \int_0^t s_i(\tau) \sin\left[(\mu t + \omega_1)\tau\right] \; d\tau \Big\} \\
&\quad \cos\left(\frac{\mu}{2}t^2 + \omega_1 t + \phi\right) \\
&\quad - \Big\{ \mp \cos\left(\frac{\mu}{2}t^2 + \omega_1 t + \phi\right) \int_0^t s_i(\tau) \sin\left[(\mu t + \omega_1)\tau\right] \; d\tau \\
&\quad \pm \sin\left(\frac{\mu}{2}t^2 + \omega_1 t + \phi\right) \int_0^t s_i(\tau) \cos\left[(\mu t + \omega_1)\tau\right] \; d\tau \Big\} \\
&\quad \sin\left[\mp\left(\frac{\mu}{2}t^2 + \omega_1 t + \phi\right)\right] \\
&= \Big\{ \cos\left(\frac{\mu}{2}t^2 + \omega_1 t + \phi\right) \int_0^t s_i(\tau) \cos\left[(\mu t + \omega_1)\tau\right] \; d\tau \\
&\quad + \sin\left(\frac{\mu}{2}t^2 + \omega_1 t + \phi\right) \int_0^t s_i(\tau) \sin\left[(\mu t + \omega_1)\tau\right] \; d\tau \Big\} \\
&\quad \cos\left(\frac{\mu}{2}t^2 + \omega_1 t + \phi\right) \\
&\quad \pm \Big\{ \mp \cos\left(\frac{\mu}{2}t^2 + \omega_1 t + \phi\right) \int_0^t s_i(\tau) \sin\left[(\mu t + \omega_1)\tau\right] \; d\tau \\
&\quad \pm \sin\left(\frac{\mu}{2}t^2 + \omega_1 t + \phi\right) \int_0^t s_i(\tau) \cos\left[(\mu t + \omega_1)\tau\right] \; d\tau \Big\} \\
&\quad \sin\left(\frac{\mu}{2}t^2 + \omega_1 t + \phi\right) \\
&= \Big\{ \cos\left(\frac{\mu}{2}t^2 + \omega_1 t + \phi\right) \int_0^t s_i(\tau) \cos\left[(\mu t + \omega_1)\tau\right] \; d\tau \\
&\quad + \sin\left(\frac{\mu}{2}t^2 + \omega_1 t + \phi\right) \int_0^t s_i(\tau) \sin\left[(\mu t + \omega_1)\tau\right] \; d\tau \Big\} \\
&\quad \cos\left(\frac{\mu}{2}t^2 + \omega_1 t + \phi\right) \\
&\quad - \Big\{ \cos\left(\frac{\mu}{2}t^2 + \omega_1 t + \phi\right) \int_0^t s_i(\tau) \sin\left[(\mu t + \omega_1)\tau\right] \; d\tau \\
&\quad + \sin\left(\frac{\mu}{2}t^2 + \omega_1 t + \phi\right) \int_0^t s_i(\tau) \cos\left[(\mu t + \omega_1)\tau\right] \; d\tau \Big\} \\
&\quad \sin\left(\frac{\mu}{2}t^2 + \omega_1 t + \phi\right)
\end{aligned}
\tag{B.40}
$$

Applying the following trigonometric identity:

$$\sin(\alpha)\cos(\alpha) = \frac{1}{2}\sin(2\alpha) \tag{B.41}$$

$$\begin{aligned}
s_{or}(t) &= \cos^2\left(\frac{\mu}{2}t^2 + \omega_1 t + \phi\right)\int_0^t s_i(\tau)\cos\left[(\mu t + \omega_1)\tau\right]\,d\tau \\
&\quad + \frac{1}{2}\sin\left[2\left(\frac{\mu}{2}t^2 + \omega_1 t + \phi\right)\right]\int_0^t s_i(\tau)\sin\left[(\mu t + \omega_1)\tau\right]\,d\tau \\
&\quad - \frac{1}{2}\sin\left[2\left(\frac{\mu}{2}t^2 + \omega_1 t + \phi\right)\right]\int_0^t s_i(\tau)\sin\left[(\mu t + \omega_1)\tau\right]\,d\tau \\
&\quad + \sin^2\left(\frac{\mu}{2}t^2 + \omega_1 t + \phi\right)\int_0^t s_i(\tau)\cos\left[(\mu t + \omega_1)\tau\right]\,d\tau \\
&= \left\{\cos^2\left(\frac{\mu}{2}t^2 + \omega_1 t + \phi\right) + \sin^2\left(\frac{\mu}{2}t^2 + \omega_1 t + \phi\right)\right\}^1 \\
&\quad \int_0^t s_i(\tau)\cos\left[(\mu t + \omega_1)\tau\right]\,d\tau \\
&= \int_0^t s_i(\tau)\cos\left[(\mu t + \omega_1)\tau\right]\,d\tau.
\end{aligned} \tag{B.42}$$

$$\begin{aligned}
s_{oq}(t) &= s_{3q}(t)\,\mathrm{Re}\{s_c(t)\} + s_{3r}(t)\,\mathrm{Im}\{s_c(t)\} \\
&= \left\{\mp\cos\left(\frac{\mu}{2}t^2 + \omega_1 t + \phi\right)\int_0^t s_i(\tau)\sin\left[(\mu t + \omega_1)\tau\right]\,d\tau\right. \\
&\quad \left.\pm\sin\left(\frac{\mu}{2}t^2 + \omega_1 t + \phi\right)\int_0^t s_i(\tau)\cos\left[(\mu t + \omega_1)\tau\right]\,d\tau\right\} \\
&\quad \cos\left(\frac{\mu}{2}t^2 + \omega_1 t + \phi\right) \\
&\quad + \left\{\cos\left(\frac{\mu}{2}t^2 + \omega_1 t + \phi\right)\int_0^t s_i(\tau)\cos\left[(\mu t + \omega_1)\tau\right]\,d\tau\right. \\
&\quad \left.+\sin\left(\frac{\mu}{2}t^2 + \omega_1 t + \phi\right)\int_0^t s_i(\tau)\sin\left[(\mu t + \omega_1)\tau\right]\,d\tau\right\} \\
&\quad \sin\left[\mp\left(\frac{\mu}{2}t^2 + \omega_1 t + \varphi\right)\right] \\
&= \left\{\mp\cos\left(\frac{\mu}{2}t^2 + \omega_1 t + \phi\right)\int_0^t s_i(\tau)\sin\left[(\mu t + \omega_1)\tau\right]\,d\tau\right. \\
&\quad \left.\pm\sin\left(\frac{\mu}{2}t^2 + \omega_1 t + \phi\right)\int_0^t s_i(\tau)\cos\left[(kt + \omega_1)\tau\right]\,d\tau\right\} \\
&\quad \cos\left(\frac{\mu}{2}t^2 + \omega_1 t + \phi\right) \\
&\quad \mp\left\{\cos\left(\frac{\mu}{2}t^2 + \omega_1 t + \phi\right)\int_0^t s_i(\tau)\cos\left[(\mu t + \omega_1)\tau\right]\,d\tau\right. \\
&\quad \left.+\sin\left(\frac{\mu}{2}t^2 + \omega_1 t + \phi\right)\int_0^t s_i(\tau)\sin\left[(\mu t + \omega_1)\tau\right]\,d\tau\right\} \\
&\quad \sin\left(\frac{\mu}{2}t^2 + \omega_1 t + \phi\right)
\end{aligned} \tag{B.43}$$

Applying the following trigonometric identity:

$$\sin(\alpha)\cos(\alpha) = \frac{1}{2}\sin(2\alpha) \tag{B.44}$$

$$\begin{aligned}
s_{oq}(t) &= \mp\cos^2\left(\frac{\mu}{2}t^2 + \omega_1 t + \phi\right)\int_0^t s_i(\tau)\sin\left[(\mu t + \omega_1)\tau\right]\,d\tau \\
&\quad \cancel{\pm\frac{1}{2}\sin\left[2\left(\frac{\mu}{2}t^2 + \omega_1 t + \phi\right)\right]\int_0^t s_i(\tau)\cos\left[(\mu t + \omega_1)\tau\right]\,d\tau} \\
&\quad \cancel{\mp\frac{1}{2}\sin\left[2\left(\frac{\mu}{2}t^2 + \omega_1 t + \phi\right)\right]\int_0^t s_i(\tau)\cos\left[(\mu t + \omega_1)\tau\right]\,d\tau} \\
&\quad \mp\sin^2\left(\frac{\mu}{2}t^2 + \omega_1 t + \phi\right)\int_0^t s_i(\tau)\sin\left[(\mu t + \omega_1)\tau\right]\,d\tau \\
&= \mp\left\{\cancel{\cos^2\left(\frac{\mu}{2}t^2 + \omega_1 t + \phi\right) + \sin^2\left[\left(\frac{\mu}{2}t^2 + \omega_1 t + \phi\right)\right]}\right\}^1 \\
&\quad \int_0^t s_i(\tau)\sin\left[(\mu t + \omega_1)\tau\right]\,d\tau \\
&= \mp\int_0^t s_i(\tau)\sin\left[(\mu t + \omega_1)\tau\right]\,d\tau.
\end{aligned} \tag{B.45}$$

B.2.2 Ordinary Frequency

In the derivation that follows, k is the chirp rate of the filter in cycles per second squared, f_1 is both, the ordinary frequency of the complex sinusoid and the starting ordinary frequency of the chirp, f_2 is the end ordinary frequency of the chirp, T is the amount of time that the chirp takes to sweep from its starting frequency to its end frequency (in seconds), and is equal to the group delay swing ($\tau_{max} - \tau_{min}$) of the chirp filter, and φ is an arbitrary phase (in cycles). For simplicity, all expressions are considered to have unitary amplitude.

$$s_n(t) = e^{\pm j2\pi(f_1 t + \varphi)} \tag{B.46}$$

$$s_c(t) = e^{\mp j2\pi\left(\frac{k}{2}t^2 + f_1 t + \varphi\right)}, \text{ where } k = \frac{f_2 - f_1}{T} \tag{B.47}$$

After the first (real-by-complex) multiplication,

$$s_{1r}(t) = s_i(t)\,\mathrm{Re}\{s_n(t)\} = s_i(t)\cos\left[2\pi(f_1 t + \varphi)\right]. \tag{B.48}$$

$$s_{1q}(t) = s_i(t)\,\mathrm{Im}\{s_n(t)\} = \pm s_i(t)\sin\left[2\pi(f_1 t + \varphi)\right]. \tag{B.49}$$

After the second (complex-by-complex) multiplication,

$$\begin{aligned}
s_{2r}(t) &= s_{1r}(t)\,\mathrm{Re}\{s_c(t)\} - s_{1q}(t)\,\mathrm{Im}\{s_c(t)\} \\
&= s_i(t)\cos\left[2\pi\left(f_1 t+\varphi\right)\right]\cos\left[2\pi\left(\frac{k}{2}t^2+f_1 t+\varphi\right)\right] \\
&\quad -\left\{\pm s_i(t)\sin\left[2\pi\left(f_1 t+\varphi\right)\right]\right\}\left\{\mp\sin\left[2\pi\left(\frac{k}{2}t^2+f_1 t+\varphi\right)\right]\right\} \\
&= s_i(t)\cos\left[2\pi\left(f_1 t+\varphi\right)\right]\cos\left[2\pi\left(\frac{k}{2}t^2+f_1 t+\varphi\right)\right] \\
&\quad +s_i(t)\sin\left[2\pi\left(f_1 t+\varphi\right)\right]\sin\left[2\pi\left(\frac{k}{2}t^2+f_1 t+\varphi\right)\right] \\
&= s_i(t)\left\{\cos\left[2\pi\left(f_1 t+\varphi\right)\right]\cos\left[2\pi\left(\frac{k}{2}t^2+f_1 t+\varphi\right)\right]\right. \\
&\qquad \left.+\sin\left[2\pi\left(f_1 t+\varphi\right)\right]\sin\left[2\pi\left(\frac{k}{2}t^2+f_1 t+\varphi\right)\right]\right\}
\end{aligned} \tag{B.50}$$

Applying the following trigonometric identities:

$$\cos(\alpha)\cos(\beta) = \frac{1}{2}\cos(\alpha-\beta)+\frac{1}{2}\cos(\alpha+\beta) \tag{B.51}$$

$$\sin(\alpha)\sin(\beta) = \frac{1}{2}\cos(\alpha-\beta)-\frac{1}{2}\cos(\alpha+\beta) \tag{B.52}$$

$$\begin{aligned}
s_{2r}(t) = s_i(t)\Bigg\{&\frac{1}{2}\cos\left[2\pi\left(f_1 t+\varphi\right)-2\pi\left(\frac{k}{2}t^2+f_1 t+\varphi\right)\right] \\
&\cancel{+\frac{1}{2}\cos\left[2\pi\left(f_1 t+\varphi\right)+2\pi\left(\frac{k}{2}t^2+f_1 t+\varphi\right)\right]} \\
&+\frac{1}{2}\cos\left[2\pi\left(f_1 t+\varphi\right)-2\pi\left(\frac{k}{2}t^2+f_1 t+\varphi\right)\right] \\
&\cancel{-\frac{1}{2}\cos\left[2\pi\left(f_1 t+\varphi\right)+2\pi\left(\frac{k}{2}t^2+f_1 t+\varphi\right)\right]}\Bigg\} \\
= s_i(t)&\cos\left[2\pi\left(f_1 t+\varphi\right)-2\pi\left(\frac{k}{2}t^2+f_1 t+\varphi\right)\right] \\
= s_i(t)&\cos\left[2\pi\left(\frac{k}{2}t^2\right)\right].
\end{aligned} \tag{B.53}$$

$$\begin{aligned}
s_{2q}(t) &= s_{1q}(t)\,\mathrm{Re}\{s_c(t)\} + s_{1r}(t)\,\mathrm{Im}\{s_c(t)\} \\
&= \pm s_i(t)\sin\left[2\pi\left(f_1 t+\varphi\right)\right]\cos\left[2\pi\left(\frac{k}{2}t^2+f_1 t+\varphi\right)\right] \\
&\quad \mp s_i(t)\cos\left[2\pi\left(f_1 t+\varphi\right)\right]\sin\left[2\pi\left(\frac{k}{2}t^2+f_1 t+\varphi\right)\right] \\
&= s_i(t)\left\{\pm\sin\left[2\pi\left(f_1 t+\varphi\right)\right]\cos\left[2\pi\left(\frac{k}{2}t^2+f_1 t+\varphi\right)\right]\right. \\
&\qquad \left.\mp\cos\left[2\pi\left(f_1 t+\varphi\right)\right]\sin\left[2\pi\left(\frac{k}{2}t^2+f_1 t+\varphi\right)\right]\right\}
\end{aligned} \tag{B.54}$$

Applying the following trigonometric identities:

$$\sin(\alpha)\cos(\beta) = \frac{1}{2}\sin(\alpha+\beta)+\frac{1}{2}\sin(\alpha-\beta) \tag{B.55}$$

$$\cos(\alpha)\sin(\beta) = \frac{1}{2}\sin(\alpha+\beta)-\frac{1}{2}\sin(\alpha-\beta) \tag{B.56}$$

$$
\begin{aligned}
s_{2q}(t) = s_i(t) \Bigg\{ & \cancel{\pm\frac{1}{2}\sin\left[2\pi\left(f_1 t+\varphi\right)+2\pi\left(\frac{k}{2}t^2+f_1 t+\varphi\right)\right]} \\
& \pm\frac{1}{2}\sin\left[2\pi\left(f_1 t+\varphi\right)-2\pi\left(\frac{k}{2}t^2+f_1 t+\varphi\right)\right] \\
& \cancel{\mp\frac{1}{2}\sin\left[2\pi\left(f_1 t+\varphi\right)+2\pi\left(\frac{k}{2}t^2+f_1 t+\varphi\right)\right]} \\
& \pm\frac{1}{2}\sin\left[2\pi\left(f_1 t+\varphi\right)-2\pi\left(\frac{k}{2}t^2+f_1 t+\varphi\right)\right]\Bigg\} \\
= {} & \pm s_i(t)\sin\left[2\pi\left(f_1 t+\varphi\right)-2\pi\left(\frac{k}{2}t^2+f_1 t+\varphi\right)\right] \\
= {} & \mp s_i(t)\sin\left[2\pi\left(\frac{k}{2}t^2\right)\right].
\end{aligned}
\tag{B.57}
$$

Each real filter realize a convolution in a finite time interval [120]. This is equivalent to multiplying both, the filter input signal, $s_{2r}(t)$ or $s_{2q}(t)$, and the filter impulse response, $h_r(t)$ or $h_q(t)$, by a unit step function, defined by

$$
u(t) = \begin{cases} 1, & \text{if } t \geqslant 0 \\ 0, & \text{if } t < 0 \end{cases}. \tag{B.58}
$$

Thus, the outputs of the filters are

$$
\begin{aligned}
s_{3r}(t) &= \left[s_{2r}(t)\,u(t)\right] * \left[h_r(t)\,u(t)\right] - \left[s_{2q}(t)\,u(t)\right] * \left[h_q(t)\,u(t)\right] \\
&= \int_{-\infty}^{\infty} s_{2r}(\tau)\,u(\tau)\,h_r(t-\tau)\,u(t-\tau)\;d\tau \\
&\quad - \int_{-\infty}^{\infty} s_{2q}(\tau)\,u(\tau)\,h_q(t-\tau)\,u(t-\tau)\;d\tau \\
&= \int_0^t s_{2r}(\tau)\,h_r(t-\tau)\;d\tau - \int_0^t s_{2q}(\tau)\,h_q(t-\tau)\;d\tau \\
&= \int_0^t s_{2r}(\tau)\,h_r(t-\tau) - s_{2q}(\tau)\,h_q(t-\tau)\;d\tau \\
&= \int_0^t s_{2r}(\tau)\,\mathrm{Re}\{s_c^*(t-\tau)\} - s_{2q}(\tau)\,\mathrm{Im}\{s_c^*(t-\tau)\}\;d\tau \\
&= \int_0^t s_i(\tau)\cos\left[2\pi\left(\frac{k}{2}\tau^2\right)\right]\cos\left\{2\pi\left[\frac{k}{2}(t-\tau)^2+f_1(t-\tau)+\varphi\right]\right\} \\
&\qquad - \left\{\mp s_i(\tau)\sin\left[2\pi\left(\frac{k}{2}\tau^2\right)\right]\right\}\sin\left\{\pm 2\pi\left[\frac{k}{2}(t-\tau)^2+f_1(t-\tau)+\varphi\right]\right\}\;d\tau \\
&= \int_0^t s_i(\tau)\cos\left[2\pi\left(\frac{k}{2}\tau^2\right)\right]\cos\left\{2\pi\left[\frac{k}{2}(t-\tau)^2+f_1(t-\tau)+\varphi\right]\right\} \\
&\qquad + s_i(\tau)\sin\left[2\pi\left(\frac{k}{2}\tau^2\right)\right]\sin\left\{2\pi\left[\frac{k}{2}(t-\tau)^2+f_1(t-\tau)+\varphi\right]\right\}\;d\tau
\end{aligned}
\tag{B.59}
$$

Applying the following trigonometric identities:

$$
\cos(\alpha)\cos(\beta) = \frac{1}{2}\cos(\alpha-\beta) + \frac{1}{2}\cos(\alpha+\beta) \tag{B.60}
$$

$$
\sin(\alpha)\sin(\beta) = \frac{1}{2}\cos(\alpha-\beta) - \frac{1}{2}\cos(\alpha+\beta) \tag{B.61}
$$

$$
\begin{aligned}
s_{3r}(t) = \int_0^t & \frac{1}{2} s_i(\tau) \cos\left\{2\pi\left(\frac{k}{2}\tau^2\right) - 2\pi\left[\frac{k}{2}(t-\tau)^2 + f_1(t-\tau) + \varphi\right]\right\} \\
& \cancel{+\frac{1}{2} s_i(\tau) \cos\left\{2\pi\left(\frac{k}{2}\tau^2\right) + 2\pi\left[\frac{k}{2}(t-\tau)^2 + f_1(t-\tau) + \varphi\right]\right\}} \\
& + \frac{1}{2} s_i(\tau) \cos\left\{2\pi\left(\frac{k}{2}\tau^2\right) - 2\pi\left[\frac{k}{2}(t-\tau)^2 + f_1(t-\tau) + \varphi\right]\right\} \\
& \cancel{-\frac{1}{2} s_i(\tau) \cos\left\{2\pi\left(\frac{k}{2}\tau^2\right) + 2\pi\left[\frac{k}{2}(t-\tau)^2 + f_1(t-\tau) + \varphi\right]\right\}} \, d\tau \\
= \int_0^t & s_i(\tau) \cos\left\{2\pi\left(\frac{k}{2}\tau^2\right) - 2\pi\left[\frac{k}{2}(t-\tau)^2 + f_1(t-\tau) + \varphi\right]\right\} \, d\tau \\
= \int_0^t & s_i(\tau) \cos\left\{2\pi\left[\frac{k}{2}\tau^2 - \frac{k}{2}(t-\tau)^2 - f_1(t-\tau) - \varphi\right]\right\} \, d\tau \\
= \int_0^t & s_i(\tau) \cos\left[2\pi\left(\cancel{\frac{k}{2}\tau^2} - \frac{k}{2}t^2 + kt\tau - \cancel{\frac{k}{2}\tau^2} - f_1 t + f_1\tau - \varphi\right)\right] \, d\tau \\
= \int_0^t & s_i(\tau) \cos\left[2\pi(kt + f_1)\tau - 2\pi\left(\frac{k}{2}t^2 + f_1 t + \varphi\right)\right] \, d\tau
\end{aligned}
\tag{B.62}
$$

Applying the following trigonometric identity:

$$
\cos(\alpha \pm \beta) = \cos(\alpha)\cos(\beta) \mp \sin(\alpha)\sin(\beta) \tag{B.63}
$$

$$
\begin{aligned}
s_{3r}(t) = \int_0^t & s_i(\tau) \left\{\cos\left[2\pi(kt + f_1)\tau\right] \cos\left[2\pi\left(\frac{k}{2}t^2 + f_1 t + \varphi\right)\right]\right. \\
& \left. + \sin\left[2\pi(kt + f_1)\tau\right] \sin\left[2\pi\left(\frac{k}{2}t^2 + f_1 t + \varphi\right)\right]\right\} \, d\tau \\
= \cos & \left[2\pi\left(\frac{k}{2}t^2 + f_1 t + \varphi\right)\right] \int_0^t s_i(\tau) \cos\left[2\pi(kt + f_1)\tau\right] \, d\tau \\
& + \sin\left[2\pi\left(\frac{k}{2}t^2 + f_1 t + \varphi\right)\right] \int_0^t s_i(\tau) \sin\left[2\pi(kt + f_1)\tau\right] \, d\tau.
\end{aligned}
\tag{B.64}
$$

$$
\begin{aligned}
s_{3q}(t) &= [s_{2q}(t)\,u(t)] * [h_r(t)\,u(t)] + [s_{2r}(t)\,u(t)] * [h_q(t)\,u(t)] \\
&= \int_{-\infty}^{\infty} s_{2q}(\tau)\,u(\tau)\,h_r(t-\tau)\,u(t-\tau)\;\,d\tau \\
&\quad + \int_{-\infty}^{\infty} s_{2r}(\tau)\,u(\tau)\,h_q(t-\tau)\,u(t-\tau)\;\,d\tau \\
&= \int_0^t s_{2q}(\tau)\,h_r(t-\tau)\;\,d\tau + \int_0^t s_{2r}(\tau)\,h_q(t-\tau)\;\,d\tau \\
&= \int_0^t s_{2q}(\tau)\,h_r(t-\tau) + s_{2r}(\tau)\,h_q(t-\tau)\;\,d\tau \\
&= \int_0^t s_{2q}(\tau)\,\mathrm{Re}\{s_c^*(t-\tau)\} + s_{2r}(\tau)\,\mathrm{Im}\{s_c^*(t-\tau)\}\;d\tau \\
&= \int_0^t \mp s_i(\tau)\sin\left[2\pi\left(\frac{k}{2}\tau^2\right)\right]\cos\left\{2\pi\left[\frac{k}{2}(t-\tau)^2 + f_1(t-\tau) + \varphi\right]\right\} \\
&\qquad + s_i(\tau)\cos\left[2\pi\left(\frac{k}{2}\tau^2\right)\right]\sin\left\{\pm 2\pi\left[\frac{k}{2}(t-\tau)^2 + f_1(t-\tau) + \varphi\right]\right\}\;d\tau \\
&= \int_0^t \mp s_i(\tau)\sin\left[2\pi\left(\frac{k}{2}\tau^2\right)\right]\cos\left\{2\pi\left[\frac{k}{2}(t-\tau)^2 + f_1(t-\tau) + \varphi\right]\right\} \\
&\qquad \pm s_i(\tau)\cos\left[2\pi\left(\frac{k}{2}\tau^2\right)\right]\sin\left\{2\pi\left[\frac{k}{2}(t-\tau)^2 + f_1(t-\tau) + \varphi\right]\right\}\;d\tau
\end{aligned}
\tag{B.65}
$$

Applying the following trigonometric identities:

$$\sin(\alpha)\cos(\beta) = \frac{1}{2}\sin(\alpha+\beta) + \frac{1}{2}\sin(\alpha-\beta) \tag{B.66}$$

$$\cos(\alpha)\sin(\beta) = \frac{1}{2}\sin(\alpha+\beta) - \frac{1}{2}\sin(\alpha-\beta) \tag{B.67}$$

$$
\begin{aligned}
s_{3q}(t) = \int_0^t & \cancel{\mp\frac{1}{2}s_i(\tau)\sin\left\{2\pi\left(\frac{k}{2}\tau^2\right) + 2\pi\left[\frac{k}{2}(t-\tau)^2 + f_1(t-\tau) + \varphi\right]\right\}} \\
& \mp\frac{1}{2}s_i(\tau)\sin\left\{2\pi\left(\frac{k}{2}\tau^2\right) - 2\pi\left[\frac{k}{2}(t-\tau)^2 + f_1(t-\tau) + \varphi\right]\right\} \\
& \cancel{\pm\frac{1}{2}s_i(\tau)\sin\left\{2\pi\left(\frac{k}{2}\tau^2\right) + 2\pi\left[\frac{k}{2}(t-\tau)^2 + f_1(t-\tau) + \varphi\right]\right\}} \\
& \mp\frac{1}{2}s_i(\tau)\sin\left\{2\pi\left(\frac{k}{2}\tau^2\right) - 2\pi\left[\frac{k}{2}(t-\tau)^2 + f_1(t-\tau) + \varphi\right]\right\}\;d\tau \\
= \mp \int_0^t & s_i(\tau)\sin\left\{2\pi\left(\frac{k}{2}\tau^2\right) - 2\pi\left[\frac{k}{2}(t-\tau)^2 + f_1(t-\tau) + \varphi\right]\right\}\;d\tau \\
= \mp \int_0^t & s_i(\tau)\sin\left\{2\pi\left[\frac{k}{2}\tau^2 - \frac{k}{2}(t-\tau)^2 - f_1(t-\tau) - \varphi\right]\right\}\;d\tau \\
= \mp \int_0^t & s_i(\tau)\sin\left[2\pi\left(\cancel{\frac{k}{2}\tau^2} - \frac{k}{2}t^2 + kt\tau - \cancel{\frac{k}{2}\tau^2} - f_1 t + f_1\tau - \varphi\right)\right]\;d\tau \\
= \mp \int_0^t & s_i(\tau)\sin\left[2\pi(kt+f_1)\tau - 2\pi\left(\frac{k}{2}t^2 + f_1 t + \varphi\right)\right]\;d\tau
\end{aligned}
\tag{B.68}
$$

Applying the following trigonometric identity:

$$\sin(\alpha \pm \beta) = \sin(\alpha)\cos(\beta) \pm \cos(\alpha)\sin(\beta) \tag{B.69}$$

$$
\begin{aligned}
s_{3q}(t) &= \mp \int_0^t s_i(\tau) \left\{ \sin\left[2\pi (kt + f_1)\tau\right] \cos\left[2\pi \left(\frac{k}{2}t^2 + f_1 t + \varphi\right)\right] \right. \\
&\qquad \left. - \cos\left[2\pi (kt + f_1)\tau\right] \sin\left[2\pi \left(\frac{k}{2}t^2 + f_1 t + \varphi\right)\right] \right\} \, d\tau \\
&= \mp \cos\left[2\pi \left(\frac{k}{2}t^2 + f_1 t + \varphi\right)\right] \int_0^t s_i(\tau) \sin\left[2\pi (kt + f_1)\tau\right] \, d\tau \\
&\quad \pm \sin\left[2\pi \left(\frac{k}{2}t^2 + f_1 t + \varphi\right)\right] \int_0^t s_i(\tau) \cos\left[2\pi (kt + f_1)\tau\right] \, d\tau.
\end{aligned}
\tag{B.70}
$$

After the third multiplication, the system outputs

$$
\begin{aligned}
s_{or}(t) &= s_{3r}(t) \operatorname{Re}\{s_c(t)\} - s_{3q}(t) \operatorname{Im}\{s_c(t)\} \\
&= \left\{ \cos\left[2\pi \left(\frac{k}{2}t^2 + f_1 t + \varphi\right)\right] \int_0^t s_i(\tau) \cos\left[2\pi (kt + f_1)\tau\right] \, d\tau \right. \\
&\quad \left. + \sin\left[2\pi \left(\frac{k}{2}t^2 + f_1 t + \varphi\right)\right] \int_0^t s_i(\tau) \sin\left[2\pi (kt + f_1)\tau\right] \, d\tau \right\} \\
&\quad \cos\left[2\pi \left(\frac{k}{2}t^2 + f_1 t + \varphi\right)\right] \\
&\quad - \left\{ \mp \cos\left[2\pi \left(\frac{k}{2}t^2 + f_1 t + \varphi\right)\right] \int_0^t s_i(\tau) \sin\left[2\pi (kt + f_1)\tau\right] \, d\tau \right. \\
&\quad \left. \pm \sin\left[2\pi \left(\frac{k}{2}t^2 + f_1 t + \varphi\right)\right] \int_0^t s_i(\tau) \cos\left[2\pi (kt + f_1)\tau\right] \, d\tau \right\} \\
&\quad \sin\left[\mp 2\pi \left(\frac{k}{2}t^2 + f_1 t + \varphi\right)\right] \\
&= \left\{ \cos\left[2\pi \left(\frac{k}{2}t^2 + f_1 t + \varphi\right)\right] \int_0^t s_i(\tau) \cos\left[2\pi (kt + f_1)\tau\right] \, d\tau \right. \\
&\quad \left. + \sin\left[2\pi \left(\frac{k}{2}t^2 + f_1 t + \varphi\right)\right] \int_0^t s_i(\tau) \sin\left[2\pi (kt + f_1)\tau\right] \, d\tau \right\} \\
&\quad \cos\left[2\pi \left(\frac{k}{2}t^2 + f_1 t + \varphi\right)\right] \\
&\quad \pm \left\{ \mp \cos\left[2\pi \left(\frac{k}{2}t^2 + f_1 t + \varphi\right)\right] \int_0^t s_i(\tau) \sin\left[2\pi (kt + f_1)\tau\right] \, d\tau \right. \\
&\quad \left. \pm \sin\left[2\pi \left(\frac{k}{2}t^2 + f_1 t + \varphi\right)\right] \int_0^t s_i(\tau) \cos\left[2\pi (kt + f_1)\tau\right] \, d\tau \right\} \\
&\quad \sin\left[2\pi \left(\frac{k}{2}t^2 + f_1 t + \varphi\right)\right]
\end{aligned}
\tag{B.71}
$$

$$
\begin{aligned}
s_{or}(t) = & \left\{ \cos\left[2\pi\left(\frac{k}{2}t^2 + f_1 t + \varphi\right)\right] \int_0^t s_i(\tau) \cos\left[2\pi\left(kt + f_1\right)\tau\right]\ d\tau \right. \\
& \left. + \sin\left[2\pi\left(\frac{k}{2}t^2 + f_1 t + \varphi\right)\right] \int_0^t s_i(\tau) \sin\left[2\pi\left(kt + f_1\right)\tau\right]\ d\tau \right\} \\
& \cos\left[2\pi\left(\frac{k}{2}t^2 + f_1 t + \varphi\right)\right] \\
& - \left\{ \cos\left[2\pi\left(\frac{k}{2}t^2 + f_1 t + \varphi\right)\right] \int_0^t s_i(\tau) \sin\left[2\pi\left(kt + f_1\right)\tau\right]\ d\tau \right. \\
& \left. + \sin\left[2\pi\left(\frac{k}{2}t^2 + f_1 t + \varphi\right)\right] \int_0^t s_i(\tau) \cos\left[2\pi\left(kt + f_1\right)\tau\right]\ d\tau \right\} \\
& \sin\left[2\pi\left(\frac{k}{2}t^2 + f_1 t + \varphi\right)\right]
\end{aligned}
\tag{B.72}
$$

Applying the following trigonometric identity:

$$
\sin(\alpha)\cos(\alpha) = \frac{1}{2}\sin(2\alpha) \tag{B.73}
$$

$$
\begin{aligned}
s_{or}(t) = & \cos^2\left[2\pi\left(\frac{k}{2}t^2 + f_1 t + \varphi\right)\right] \int_0^t s_i(\tau) \cos\left[2\pi\left(kt + f_1\right)\tau\right]\ d\tau \\
& + \frac{1}{2}\sin\left[4\pi\left(\frac{k}{2}t^2 + f_1 t + \varphi\right)\right] \int_0^t s_i(\tau) \sin\left[2\pi\left(kt + f_1\right)\tau\right]\ d\tau \\
& - \frac{1}{2}\sin\left[4\pi\left(\frac{k}{2}t^2 + f_1 t + \varphi\right)\right] \int_0^t s_i(\tau) \sin\left[2\pi\left(kt + f_1\right)\tau\right]\ d\tau \\
& + \sin^2\left[2\pi\left(\frac{k}{2}t^2 + f_1 t + \varphi\right)\right] \int_0^t s_i(\tau) \cos\left[2\pi\left(kt + f_1\right)\tau\right]\ d\tau \\
= & \left\{ \cos^2\left[2\pi\left(\frac{k}{2}t^2 + f_1 t + \varphi\right)\right] + \sin^2\left[2\pi\left(\frac{k}{2}t^2 + f_1 t + \varphi\right)\right] \right\}^1 \\
& \int_0^t s_i(\tau) \cos\left[2\pi\left(kt + f_1\right)\tau\right]\ d\tau \\
= & \int_0^t s_i(\tau) \cos\left[2\pi\left(kt + f_1\right)\tau\right]\ d\tau.
\end{aligned}
\tag{B.74}
$$

$$
\begin{aligned}
s_{oq}(t) &= s_{3q}(t)\,\mathrm{Re}\{s_c(t)\} + s_{3r}(t)\,\mathrm{Im}\{s_c(t)\} \\
&= \left\{ \mp\cos\left[2\pi\left(\frac{k}{2}t^2 + f_1 t + \varphi\right)\right] \int_0^t s_i(\tau)\sin\left[2\pi\left(kt + f_1\right)\tau\right]\, d\tau \right. \\
&\quad \left. \pm\sin\left[2\pi\left(\frac{k}{2}t^2 + f_1 t + \varphi\right)\right] \int_0^t s_i(\tau)\cos\left[2\pi\left(kt + f_1\right)\tau\right]\, d\tau \right\} \\
&\quad \cos\left[2\pi\left(\frac{k}{2}t^2 + f_1 t + \varphi\right)\right] \\
&\quad + \left\{ \cos\left[2\pi\left(\frac{k}{2}t^2 + f_1 t + \varphi\right)\right] \int_0^t s_i(\tau)\cos\left[2\pi\left(kt + f_1\right)\tau\right]\, d\tau \right. \\
&\quad \left. + \sin\left[2\pi\left(\frac{k}{2}t^2 + f_1 t + \varphi\right)\right] \int_0^t s_i(\tau)\sin\left[2\pi\left(kt + f_1\right)\tau\right]\, d\tau \right\} \\
&\quad \sin\left[\mp 2\pi\left(\frac{k}{2}t^2 + f_1 t + \varphi\right)\right] \\
&= \left\{ \mp\cos\left[2\pi\left(\frac{k}{2}t^2 + f_1 t + \varphi\right)\right] \int_0^t s_i(\tau)\sin\left[2\pi\left(kt + f_1\right)\tau\right]\, d\tau \right. \\
&\quad \left. \pm\sin\left[2\pi\left(\frac{k}{2}t^2 + f_1 t + \varphi\right)\right] \int_0^t s_i(\tau)\cos\left[2\pi\left(kt + f_1\right)\tau\right]\, d\tau \right\} \\
&\quad \cos\left[2\pi\left(\frac{k}{2}t^2 + f_1 t + \varphi\right)\right] \\
&\quad \mp \left\{ \cos\left[2\pi\left(\frac{k}{2}t^2 + f_1 t + \varphi\right)\right] \int_0^t s_i(\tau)\cos\left[2\pi\left(kt + f_1\right)\tau\right]\, d\tau \right. \\
&\quad \left. + \sin\left[2\pi\left(\frac{k}{2}t^2 + f_1 t + \varphi\right)\right] \int_0^t s_i(\tau)\sin\left[2\pi\left(kt + f_1\right)\tau\right]\, d\tau \right\} \\
&\quad \sin\left[2\pi\left(\frac{k}{2}t^2 + f_1 t + \varphi\right)\right]
\end{aligned}
\tag{B.75}
$$

Applying the following trigonometric identity:

$$
\sin(\alpha)\cos(\alpha) = \frac{1}{2}\sin(2\alpha) \tag{B.76}
$$

$$
\begin{aligned}
s_{oq}(t) &= \mp \cos^2\left[2\pi\left(\frac{k}{2}t^2 + f_1 t + \varphi\right)\right] \int_0^t s_i(\tau)\sin\left[2\pi\left(kt + f_1\right)\tau\right]\, d\tau \\
&\quad \cancel{\pm \frac{1}{2}\sin\left[4\pi\left(\frac{k}{2}t^2 + f_1 t + \varphi\right)\right] \int_0^t s_i(\tau)\cos\left[2\pi\left(kt + f_1\right)\tau\right]\, d\tau} \\
&\quad \cancel{\mp \frac{1}{2}\sin\left[4\pi\left(\frac{k}{2}t^2 + f_1 t + \varphi\right)\right] \int_0^t s_i(\tau)\cos\left[2\pi\left(kt + f_1\right)\tau\right]\, d\tau} \\
&\quad \mp \sin^2\left[2\pi\left(\frac{k}{2}t^2 + f_1 t + \varphi\right)\right] \int_0^t s_i(\tau)\sin\left[2\pi\left(kt + f_1\right)\tau\right]\, d\tau \\
&= \mp \left\{ \cancel{\cos^2\left[2\pi\left(\frac{k}{2}t^2 + f_1 t + \varphi\right)\right] + \sin^2\left[2\pi\left(\frac{k}{2}t^2 + f_1 t + \varphi\right)\right]} \right\}^1 \\
&\quad \int_0^t s_i(\tau)\sin\left[2\pi\left(kt + f_1\right)\tau\right]\, d\tau \\
&= \mp \int_0^t s_i(\tau)\sin\left[2\pi\left(kt + f_1\right)\tau\right]\, d\tau.
\end{aligned}
\tag{B.77}
$$

Appendix C

Definitions of the Fourier Transform

There exist several slightly different definitions for the Fourier transform, all of them can be summarized by the following expression [121–123]:

$$\mathcal{F}\{f(t)\} = \frac{1}{a}\int_{-\infty}^{\infty} f(t)\, e^{jb\xi t} dt \tag{C.1}$$

where the variables a and b can assume a set of values between the following: $\{a = 1, b = \pm 1\}$, $\{a = 1, b = \pm 2\pi\}$, $\left\{a = \sqrt{2\pi}, b = \pm 1\right\}$ and $\{a = 2\pi, b = \pm 1\}$. The variable ξ changes to f if $b = \pm 2\pi$ (ordinary or oscillation frequency Fourier transform), or to ω if $b = \pm 1$ (angular frequency Fourier transform).

Thus, eight different mathematical definitions for the Fourier transform exist, among which, the most common ones are those defined by the set of values given in Table C.1.

Table C.1 – Common Fourier transform definitions [123].

Set of valures	Transformation integral	Application domain
$\{a = 1, b = -2\pi\}$	$\int_{-\infty}^{\infty} f(t)\, e^{-j2\pi ft} dt$	signal processing
$\{a = 1, b = -1\}$	$\int_{-\infty}^{\infty} f(t)\, e^{-j\omega t} dt$	pure mathematics; systems engineering
$\{a = 2\pi, b = 1\}$	$\frac{1}{2\pi}\int_{-\infty}^{\infty} f(t)\, e^{j\omega t} dt$	classical physics
$\left\{a = \sqrt{2\pi}, b = 1\right\}$	$\frac{1}{\sqrt{2\pi}}\int_{-\infty}^{\infty} f(t)\, e^{j\omega t} dt$	modern physics

Appendix D

Component Models of the ST BiCMOS9MW Technology

D.1 Capacitor Model

The ST BiCMOS9MW technology offers four models for a $2\,\mathrm{fF}/\mu\mathrm{m}^2$ metal-insulator-metal (MIM) capacitor. The most accurate model (cmim3pM2) is a three-terminal component whose electrical model is shown in Fig. D.1. It models the substrate parasitic capacitance (C_{cp}), and the parasitic inductances and frequency dependent resistances of the top and bottom metal plates.

The main instance parameters are:

C Desired capacitance value

W Drawn width

MULT Number of identical devices in parallel

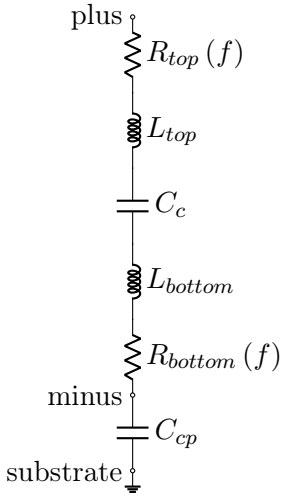

Figure D.1 – Electrical model of the MIM capacitor in the ST BiCMOS9MW technology.

D.2 Inductor Model

The ST BiCMOS9MW technology offers two kinds of inductors:

- Low value and High Q (LoHQ) inductor

  Inductance range: 0.1 nH to 0.6 nH

  Q factor range: 10 to 35

  Size: 50×50 µm^2 to 320×320 µm^2

- Low Area Multi-Width (LAMW) inductor

  Inductance range: 0.4 nH to 26 nH

  Q factor range: 10 to 25

  Size: 77×77 µm^2 to 412×412 µm^2

All inductors have a patterned ground shield (PGS) below it to isolate from substrate-coupled high-frequency interferences [124]. The electrical model of the more accurate inductor component is shown in Fig. D.2. The model takes into account the propagation, proximity, and skin effects [125]. Optionally, a middle point terminal can be used as a center tap.

The main instance parameters are:

- Coil width: 5 µm to 29.99 µm
- Internal diameter: 40 µm to 260 µm
- Number of turns (just for LAMW inductors): 2 to 9

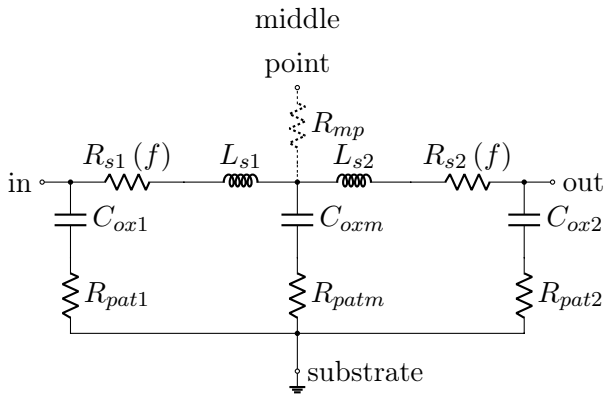

Figure D.2 – Electrical model of the inductors in the ST BiCMOS9MW technology.

Bibliography

[1] R. Withers and R. Ralston, "Superconductive analog signal processing devices", *Proc. IEEE*, vol. 77, no. 8, pp. 1247–1263, Aug. 1989. DOI: 10.1109/5.34123.

[2] C. Caloz, S. Gupta, Q. Zhang, and B. Nikfal, "Analog signal processing: A possible alternative or complement to dominantly digital radio schemes", *IEEE Microw. Mag.*, vol. 14, no. 6, pp. 87–103, Sep. 2013. DOI: 10.1109/MMM.2013.2269862.

[3] D. Gangopadhyay, A. Y. Chen, and D. J. Allstot, "Analog chirp Fourier transform for high-resolution real-time wideband RF spectrum analysis", in *2011 IEEE Int. Symp. Circuits and Syst.*, Rio de Janeiro, Brazil: IEEE, May 2011, pp. 2441–2444. DOI: 10.1109/ISCAS.2011.5938097.

[4] B. Nikfal, D. Badiere, M. Repeta, B. Deforge, S. Gupta, and C. Caloz, "Distortion-less real-time spectrum sniffing based on a stepped group-delay phaser", *IEEE Microw. Compon. Lett.*, vol. 22, no. 11, pp. 601–603, Nov. 2012. DOI: 10.1109/LMWC.2012.2219514.

[5] M. A. Jack, P. M. Grant, and J. H. Collins, "The theory, design, and applications of surface acoustic wave Fourier-transform processors", *Proc. IEEE*, vol. 68, no. 4, pp. 450–468, Apr. 1980. DOI: 10.1109/PROC.1980.11674.

[6] *ADC Performance Survey 1997-2019 (ISSCC & VLSI Symposium)*. [Online]. Available: https://web.stanford.edu/~murmann/adcsurvey.html (visited on 08/26/2019).

[7] D. Lancaster, ""Chirp"a new radar technique", *Electronics World*, pp. 42–43, 59, Jan. 1965.

[8] J. L. Hicks, Ed., *Navy Electricity and Electronics Training Series, Module 18 - Radar Principles*. Pensacola, FL, USA: Naval Education, Training Professional Development, and Technology Center, Sep. 1998.

[9] J. R. Klauder, A. C. Price, S. Darlington, and W. J. Albersheim, "The theory and design of chirp radars", *Bell Syst. Tech. J.*, vol. 39, no. 4, pp. 745–808, 1960. DOI: 10.1002/j.1538-7305.1960.tb03942.x.

[10] O. W. Otto, "Real-time Fourier transform with a surface-wave convolver", *Electronics Letters*, vol. 8, no. 25, pp. 623–624, Dec. 1972. DOI: 10.1049/el:19720451.

[11] S. Krishnamurthy, "Wireless passive surface acoustic wave (SAW) sensing system", en, Doctoral thesis, Western Michigan University, Kalamazoo, MI, USA, Aug. 2007. [Online]. Available: https://scholarworks.wmich.edu/dissertations/884/.

[12] O. W. Otto, "The chirp transform signal processor", in *1976 Ultrasonics Symp.*, Annapolis, MD, USA: IEEE, Oct. 1976, pp. 365–370. DOI: 10.1109/ULTSYM.1976.196699.

[13] M. A. Jack, G. F. Manes, P. M. Grant, C. Atzeni, L. Masotti, and J. H. Collins, "Real time network analysers based on SAW chirp transform processors", in *1976 Ultrasonics Symp. Proc.*, Annapolis, MD, USA: IEEE, Oct. 1976, pp. 376–381. DOI: 10.1109/ULTSYM.1976.196701.

[14] G. R. Nudd and O. W. Otto, "Real-time Fourier analysis of spread spectrum signals using surface-wave-implemented chirp-Z transformation", *IEEE Trans. Microw. Theory Techn.*, vol. 24, no. 1, pp. 54–56, Jan. 1976. DOI: 10.1109/TMTT.1976.1128768.

[15] L. Mertz, *Transformations in Optics*. New York, NY, USA: Wiley, 1965.

[16] C. Atzeni, G. Manes, and L. Masotti, "Programmable signal processing by analog chirp-transformation using SAW devices", in *1975 Ultrasonics Symp. Proc.*, Los Angeles, CA, USA: IEEE, Sep. 1975, pp. 371–376. DOI: 10.1109/ULTSYM.1975.196539.

[17] K. W. Martin, "Complex signal processing is not complex", *IEEE Trans. Circuits Syst. I, Reg. Papers*, vol. 51, no. 9, pp. 1823–1836, Sep. 2004. DOI: 10.1109/TCSI.2004.834522.

[18] J. M. Alsup, "Surface acoustic wave CZT processors", in *1974 Ultrasonics Symp. Proc.*, Milwaukee, WI, USA: IEEE, Nov. 1974, pp. 378–381. DOI: 10.1109/ULTSYM.1974.196358.

[19] M. A. Jack, P. M. Grant, and J. H. Collins, "Real time network analyser employing surface acoustic wave chirp filters", in *1975 Ultrasonics Symp. Proc.*, Los Angeles, CA, USA: IEEE, Sep. 1975, pp. 359–362. DOI: 10.1109/ULTSYM.1975.196537.

[20] P. M. Grant, M. A. Jack, and J. H. Collins, "Network analyser employing surface-acoustic-wave discrete Fourier-transform processor", *Electronics Letters*, vol. 11, no. 19, pp. 468–469, Sep. 1975. DOI: 10.1049/el:19750359.

[21] C. Atzeni, G. F. Manes, and L. Masotti, "Real-time network analyser using dual analogue chirp transform", *Electronics Letters*, vol. 12, no. 10, pp. 248–249, May 1976. DOI: 10.1049/el:19760191.

[22] K. Eng and O.-C. Yue, "Time compression multiplexing of multiple television signals in satellite channels using chirp transform processors", *IEEE Trans. Commun.*, vol. 29, no. 12, pp. 1832–1840, Dec. 1981. DOI: 10.1109/TCOM.1981.1094949.

[23] K. Y. Eng and B. G. Haskell, "Study of a time-compression technique for TV transmission using a chirp filter and envelope detection", *Bell Syst. Tech. J.*, vol. 60, no. 10, pp. 2373–2395, 1981. DOI: 10.1002/j.1538-7305.1981.tb00231.x.

[24] L. R. D'Addario, "Chirp transform spectrometers for millimeter spectroscopy", National Radio Astronomy Observatory, Charlottesville, VA, EUA, Tech. Rep. 274, Jan. 1988, p. 10.

[25] M. D. Shaw, N. D. J. Miller, A. P. Malarky, and D. H. Warne, "SAW chirp filter technology for satellite on-board processing applications", *Int. J. Satell. Commun.*, vol. 7, no. 4, pp. 263–282, Oct. 1989. DOI: 10.1002/sat.4600070405.

[26] P. M. Bakken and A. Rønnekleiv, "SAW-based chirp Fourier transform and its application to analogue on-board signal processing", *Int. J. Satell. Commun.*, vol. 7, no. 4, pp. 283–293, Oct. 1989. DOI: 10.1002/sat.4600070406.

[27] J. C. Sethares, "Magnetostatic wave devices and applications (invited)", *J. Appl. Phys.*, vol. 53, no. 3, pp. 2646–2651, Mar. 1982. DOI: 10.1063/1.330926.

[28] W. S. Ishak, "Magnetostatic wave technology: A review", *Proc. IEEE*, vol. 76, no. 2, pp. 171–187, Feb. 1988. DOI: 10.1109/5.4393.

[29] R. Withers, A. Anderson, J. Green, and S. Reible, "Superconductive delay-line technology and applications", *IEEE Trans. Magn.*, vol. 21, no. 2, pp. 186–192, Mar. 1985. DOI: 10.1109/TMAG.1985.1063647.

[30] R. S. Withers and S. A. Reible, "Superconductive chirp-transform spectrum analyzer", *IEEE Electron Device Lett.*, vol. 6, no. 6, pp. 261–263, Jun. 1985. DOI: 10.1109/EDL.1985.26119.

[31] W. G. Lyons, D. R. Arsenault, A. C. Anderson, T. C. L. G. Sollner, P. G. Murphy, M. M. Seaver, R. R. Boisvert, R. L. Slattery, and R. W. Ralston, "High temperature superconductive wideband compressive receivers", *IEEE Trans. Microw. Theory Techn.*, vol. 44, no. 7, pp. 1258–1278, Jul. 1996. DOI: 10.1109/22.508231.

[32] W. G. Lyons, D. R. Arsenault, C. L. Keast, D. C. Shaver, R. Berger, A. C. Anderson, P. G. Murphy, T. C. L. G. Sollner, and R. W. Ralston, "Wideband compressive receiver based on advanced superconductor and semiconductor circuits", *IEEE Trans. Appl. Supercond.*, vol. 7, no. 2, pp. 2462–2467, Jun. 1997. DOI: 10.1109/77.621738.

[33] S. Abielmona, S. Gupta, and C. Caloz, "Compressive receiver using a CRLH-based dispersive delay line for analog signal processing", *IEEE Trans. Microw. Theory Techn.*, vol. 57, no. 11, pp. 2617–2626, Nov. 2009. DOI: 10.1109/TMTT.2009.2031927.

[34] A. Salvucci, S. Colangeli, M. Palomba, G. Polli, and E. Limiti, "An active dispersive delay line in GaN MMIC technology for X-band applications", in *2016 21st Int. Conf. Microwave, Radar and Wireless Commun.*, Krakow, Poland: IEEE, May 2016, pp. 1–4. DOI: 10.1109/MIKON.2016.7492059.

[35] S. Gupta and C. Caloz, "Analog real-time Fourier transformer using a group delay engineered C-section all-pass network", in *2010 IEEE Antennas and Propagation Soc. Int. Symp.*, Toronto, ON, Canada: IEEE, Jul. 2010, pp. 1–4. DOI: 10.1109/APS.2010.5561143.

[36] ——, "Analog inverse Fourier transformer using group delay engineered C-section all-pass network", in *Conf. Proc. 40th Eur. Microwave Conf.*, Paris, France: IEEE, Sep. 2010, pp. 389–392. DOI: 10.23919/EUMC.2010.5616358.

[37] B. Xiang, A. Kopa, and A. B. Apsel, "A novel on-chip active dispersive delay line (DDL) for analog signal processing", *IEEE Microw. Compon. Lett.*, vol. 20, no. 10, pp. 584–586, Oct. 2010. DOI: 10.1109/LMWC.2010.2064761.

[38] B. Xiang, A. Kopa, Z. Fu, and A. B. Apsel, "An integrated Ku-band nanosecond time-stretching system using improved dispersive delay line (DDL)", in *Paper Dig. 2012 IEEE 12th Topical Meeting Silicon Monolithic Integrated Circuits in RF Syst.*, Santa Clara, CA, USA: IEEE, Jan. 2012, pp. 151–154. DOI: 10.1109/SiRF.2012.6160140.

[39] ——, "Theoretical analysis and practical considerations for the integrated time-stretching system using dispersive delay line (DDL)", *IEEE Trans. Microw. Theory Techn.*, vol. 60, no. 11, pp. 3449–3457, Nov. 2012. DOI: 10.1109/TMTT.2012.2215623.

[40] M. A. G. Laso, T. Lopetegi, M. J. Erro, M. Castillo, D. Benito, M. J. Garde, M. A. Muriel, M. Sorolla, and M. Guglielmi, "Real-time spectrum analysis in microstrip technology", in *2001 31st Eur. Microwave Conf.*, London, UK: IEEE, Sep. 2001, pp. 1–4. DOI: 10.1109/EUMA.2001.339009.

[41] M. A. G. Laso, T. Lopetegi, M. J. Erro, D. Benito, M. J. Garde, M. A. Muriel, M. Sorolla, and M. Guglielmi, "Real-time spectrum analysis in microstrip technology", *IEEE Trans. Microw. Theory Techn.*, vol. 51, no. 3, pp. 705–717, Mar. 2003. DOI: 10.1109/TMTT.2003.808741.

[42] J. D. Schwartz, J. Azaña, and D. V. Plant, "A fully electronic system for the time magnification of ultra-wideband signals", *IEEE Trans. Microw. Theory Techn.*, vol. 55, no. 2, pp. 327–334, Feb. 2007. DOI: 10.1109/TMTT.2006.890069.

[43] L. Ma, Y. Wu, Z. Zhuang, and Y. Liu, "A novel real-time Fourier and inverse Fourier transforming system based on non-uniform coupled-line phaser", *Int. J. Electron. Commun. (AEÜ)*, vol. 94, pp. 102–108, Sep. 2018. DOI: 10.1016/j.aeue.2018.07.001.

[44] B. Xiang, X. Wang, and A. B. Apsel, "On-chip demonstration of real time spectrum analysis (RTSA) using integrated dispersive delay line (IDDL)", in *2013 IEEE MTT-S Int. Microwave Symp. Dig.*, Seattle, WA, USA: IEEE, Jun. 2013, pp. 1–4. DOI: 10.1109/MWSYM.2013.6697467.

[45] ——, "A reconfigurable integrated dispersive delay line (RI-DDL) in 0.13-μm CMOS process", *IEEE Trans. Microw. Theory Techn.*, vol. 61, no. 7, pp. 2610–2619, Jul. 2013. DOI: 10.1109/TMTT.2013.2261088.

[46] J. Azaña and M. A. Muriel, "Real-time optical spectrum analysis based on the time-space duality in chirped fiber gratings", *IEEE J. Quantum Electron.*, vol. 36, no. 5, pp. 517–526, May 2000. DOI: 10.1109/3.842092.

[47] J. Zhang and J. Yao, "Broadband and precise microwave time reversal using a single linearly chirped fiber Bragg grating", in *Proc. 2014 Int. Topical Meeting Microwave Photonics and the 2014 9th Asia-Pacific Microwave Photonics Conf.*, Sendai, Japan: IEEE, Oct. 2014, pp. 57–60. DOI: 10.1109/MWP.2014.6994489.

[48] J. Zhang and J. Yao, "Broadband and precise microwave time reversal using a single linearly chirped fiber Bragg grating", *IEEE Trans. Microw. Theory Techn.*, vol. 63, no. 7, pp. 2166–2172, Jul. 2015. DOI: 10.1109/TMTT.2015.2432016.

[49] H. Linget, T. Chaneliere, J.-L. Le Gouet, A. Louchet-Chauvet, and L. Morvan, "Time-reversal of μs-long radiofrequency signals based on approximate temporal imaging", in *2013 IEEE Int. Topical Meeting Microwave Photonics Proc.*, Alexandria, VA, USA: IEEE, Oct. 2013, pp. 29–32. DOI: 10.1109/MWP.2013.6724011.

[50] P. Berger, M. Schwarz, S. Molin, D. Dolfi, L. Morvan, A. Louchet-Chauvet, T. Chanelière, and J.-L. Le Gouët, "20 GHz instantaneous bandwidth RF spectrum analyzer with high time-resolution", in *Proc. 2014 Int. Topical Meeting Microwave Photonics and 9th Asia-Pacific Microwave Photonics Conf.*, Sapporo, Japan: IEEE, Oct. 2014, pp. 331–334. DOI: 10.1109/MWP.2014.6994566.

[51] P. J. Hall, "A radio polarimeter-spectrometer", Doctoral thesis, University of Tasmania, Mar. 1985.

[52] P. Hartogh, "Present and future chirp transform spectrometers for microwave remote sensing", in *Proc. SPIE 3221, Sensors, Syst., and Next-Generation Satellites*, vol. 3221, London, UK: International Society for Optics and Photonics, Sep. 1997, pp. 328–339. DOI: 10.1117/12.298099.

[53] G. Chin, D. Buhl, and J. M. Florez, "Acousto-optic spectrometer for radio astronomy", in *NASA Conf. Publication 2138 - Heterodyne Syst. and Technol. - Part II*, W. T. Rhodes, Ed., Williamsburg, VA, USA, Mar. 1980, pp. 385–397.

[54] P. Hartogh and G. K. Hartmann, "A high-resolution chirp transform spectrometer for microwave measurements", *Meas. Sci. Technol.*, vol. 1, no. 7, pp. 592–595, 1990.

[55] K. Osterschek and P. Hartogh, "A fast, high resolution chirp transform spectrometer for atmospheric remote sensing from space", in *1991 Int. Geosci. and Remote Sensing Symp.*, vol. 2, Espoo, Finland: IEEE, Jun. 1991, pp. 979–982. DOI: 10.1109/IGARSS.1991.580283.

[56] X. Li, "Development of RAC devices fabricated using e-beam lithography for Chirp Transform Spectrometers", PhD thesis, Albert-Ludwigs-Universität Freiburg im Breisgau, Freiburg im Breisgau, 2010.

[57] P. Hartogh and C. Jarchow, "Millimeter wave detection of mesospheric ozone using a high resolution chirp transform spectrometer backend", in *1994 Int. Geosci. and Remote Sensing Symp.*, vol. 1, Pasadena, CA, USA: IEEE, Aug. 1994, pp. 3–5. DOI: 10.1109/IGARSS.1994.399040.

[58] G. Villanueva and P. Hartogh, "The high resolution chirp transform spectrometer for the SOFIA-GREAT instrument", *Exp. Astron.*, vol. 18, no. 1-3, pp. 77–91, Dec. 2004. DOI: 10.1007/s10686-005-9004-3.

[59] G. L. Villanueva Sozzi, "The high resolution spectrometer for SOFIA-GREAT instrumentation, atmospheric modeling and observations", PhD thesis, Albert-Ludwigs-Universität zu Freiburg, Freiburg, 2004.

[60] G. L. Villanueva, P. Hartogh, and L. M. Reindl, "A digital dispersive matching network for SAW devices in chirp transform spectrometers", *IEEE Trans. Microw. Theory Techn.*, vol. 54, no. 4, pp. 1415–1424, Jun. 2006. DOI: 10.1109/TMTT.2006.871244.

[61] S. Gulkis, M. Frerking, J. Crovisier, G. Beaudin, P. Hartogh, P. Encrenaz, T. Koch, C. Kahn, Y. Salinas, R. Nowicki, R. Irigoyen, M. Janssen, P. Stek, M. Hofstadter, M. Allen, C. Backus, L. Kamp, C. Jarchow, E. Steinmetz, A. Deschamps, J. Krieg, M. Gheudin, D. Bockelée-Morvan, N. Biver, T. Encrenaz, D. Despois, W. Ip, E. Lellouch, I. Mann,

D. Muhleman, H. Rauer, P. Schloerb, and T. Spilker, "MIRO: Microwave Instrument for Rosetta Orbiter", *Space Sci. Rev.*, vol. 128, no. 1-4, pp. 561–597, May 2007. DOI: 10.1007/s11214-006-9032-y.

[62] L. Paganini, "Power spectral density accuracy in chirp transform spectrometers", PhD thesis, Copernicus, Katlenburg-Lindau, 2008.

[63] F. Rivet, Y. Deval, J.-B. Begueret, D. Dallet, and D. Belot, "A disruptive software-defined radio receiver architecture based on sampled analog signal processing", in *Proc. 2007 IEEE Radio Frequency Integrated Circuits Symp.*, Honolulu, HI, USA: IEEE, Jun. 2007, pp. 197–200. DOI: 10.1109/RFIC.2007.380864.

[64] F. Rivet, Y. Deval, J.-B. Begueret, D. Dallet, P. Cathelin, and D. Belot, "A disruptive receiver architecture dedicated to software-defined radio", *IEEE Trans. Circuits Syst. II, Exp. Briefs*, vol. 55, no. 4, pp. 344–348, Apr. 2008. DOI: 10.1109/TCSII.2008.919512.

[65] ——, "The experimental demonstration of a SASP-based full software radio receiver", *IEEE J. Solid-State Circuits*, vol. 45, no. 5, pp. 979–988, May 2010. DOI: 10.1109/JSSC.2010.2041402.

[66] B. Sadhu, M. Sturm, B. M. Sadler, and R. Harjani, "A 5gs/s 12.2 pJ/conv. analog charge-domain FFT for a software defined radio receiver front-end in 65nm CMOS", in *2012 IEEE Radio Frequency Integrated Circuits (RFIC) Symp. Dig. Papers*, Montreal, QC, Canada: IEEE, Jun. 2012, pp. 39–42. DOI: 10.1109/RFIC.2012.6242227.

[67] ——, "Analysis and design of a 5 GS/s analog charge-domain FFT for an SDR front-end in 65 nm CMOS", *IEEE J. Solid-State Circuits*, vol. 48, no. 5, pp. 1199–1211, May 2013. DOI: 10.1109/JSSC.2013.2250457.

[68] H. Shin, R. K. Palani, A. Saha, F.-L. Yuan, D. Markovic, and R. Harjani, "An eight channel analog-FFT based 450ms/s hybrid filter bank ADC with improved SNDR for multi-band signals in 40nm CMOS", in *2015 IEEE Custom Integrated Circuits Conf.*, San Jose, CA, USA: IEEE, Sep. 2015, pp. 1–4. DOI: 10.1109/CICC.2015.7338459.

[69] H. Shin and R. Harjani, "Low-power wideband analog channelization filter bank using passive polyphase-FFT techniques", *IEEE J. Solid-State Circuits*, vol. 52, no. 7, pp. 1753–1767, Jul. 2017. DOI: 10.1109/JSSC.2017.2700792.

[70] D. Sundararajan, *Digital Signal Processing: Theory and Practice*. Singapore: World Scientific Publishing Co. Pte. Ltd., 2003, ISBN: 981-238-216-X.

[71] E. A. Morelli, "High accuracy evaluation of the finite Fourier transform using sampled data", NASA Langley Research Center, Hampton, VA, USA, Technical Memorandum NASA TM-110340, Jun. 1997, p. 38.

[72] P. Challener, "Design and realisation of practical wideband quadrature networks with linear phase-shift characteristics", en, *IEE Journal on Electronic Circuits and Systems*, vol. 2, no. 3, p. 65, 1978. DOI: 10.1049/ij-ecs.1978.0015. [Online]. Available: http://digital-library.theiet.org/content/journals/10.1049/ij-ecs.1978.0015 (visited on 04/06/2018).

[73] B. Nikfal, S. Gupta, and C. Caloz, "Increased group-delay slope loop system for enhanced-resolution analog signal processing", *IEEE Trans. Microw. Theory Techn.*, vol. 59, no. 6, pp. 1622–1628, Jun. 2011. DOI: 10.1109/TMTT.2011.2117436.

[74] W. J. Caputi, "Stretch: A time-transformation technique", *IEEE Trans. Aerosp. Electron. Syst.*, vol. AES-7, no. 2, pp. 269–278, Mar. 1971. DOI: 10.1109/TAES.1971.310366.

[75] C. E. Cook, "Pulse compression - key to more efficient radar transmission", *Proc. IRE*, vol. 48, no. 3, pp. 310–316, Mar. 1960. DOI: 10.1109/JRPROC.1960.287599.

[76] S. Gupta, B. Nikfal, and C. Caloz, "RFID system based on pulse-position modulation using group delay engineered microwave C-sections", in *2010 Asia-Pacific Microwave Conf. Proc.*, Yokohama, Japan: IEEE, Dec. 2010, pp. 203–206, ISBN: 978-1-902339-22-2.

[77] S. Abielmona, S. Gupta, and C. Caloz, "Experimental demonstration and characterization of a tunable CRLH delay line system for impulse/continuous wave", *IEEE Microw. Compon. Lett.*, vol. 17, no. 12, pp. 864–866, Dec. 2007. DOI: 10.1109/LMWC.2007.910492.

[78] S. Gupta, Q. Zhang, L. Zou, L. J. Jiang, and C. Caloz, "Generalized coupled-line all-pass phasers", en, *IEEE Trans. Microw. Theory Techn.*, vol. 63, no. 3, pp. 1007–1018, Mar. 2015. DOI: 10.1109/TMTT.2015.2397445. [Online]. Available: http://ieeexplore.ieee.org/document/7044609/ (visited on 03/21/2017).

[79] H. M. Gerard, W. R. Smith, W. R. Jones, and J. B. Harrington, "The design and applications of highly dispersive acoustic surface-wave filters", *IEEE Trans. Microw. Theory Techn.*, vol. 21, no. 4, pp. 176–186, Apr. 1973. DOI: 10.1109/TMTT.1973.1127968.

[80] Q. Zhang, D. L. Sounas, and C. Caloz, "Synthesis of cross-coupled reduced-order dispersive delay structures (DDSs) with arbitrary group delay and controlled magnitude", *IEEE Trans. Microw. Theory Techn.*, vol. 61, no. 3, pp. 1043–1052, Mar. 2013. DOI: 10.1109/TMTT.2013.2241785.

[81] S. Gupta, A. Parsa, E. Perret, R. V. Snyder, R. J. Wenzel, and C. Caloz, "Group-delay engineered noncommensurate transmission line all-pass network for analog signal processing", en, *IEEE Trans. Microw. Theory Techn.*, vol. 58, no. 9, pp. 2392–2407, Sep. 2010. DOI: 10.1109/TMTT.2010.2058933. [Online]. Available: http://ieeexplore.ieee.org/document/5549964/ (visited on 03/21/2017).

[82] R. J. Cameron, C. M. Kudsia, and R. R. Mansour, *Microwave Filters for Communication Systems: Fundamentals, Design, and Applications*. Hoboken, NJ, USA: John Wiley & Sons, 2007, ISBN: 978-0-471-45022-1.

[83] T. J. Rivlin, *The Chebyshev Polynomials*. John Wiley & Sons, 1974, ch. 3, p. 131, ISBN: 9780471724704.

[84] P. Jarry and J. Beneat, *Advanced Design Techniques and Realizations of Microwave and RF Filters*. Hoboken, NJ, USA: John Wiley & Sons, 2008, ISBN: 978-04-7029-416-1.

[85] L. Wanhammar, *Analog Filters Using MATLAB*. Springer, 2009, ISBN: 978-03-8792-766-4.

[86] J. Bechhoefer, "Kramers–Kronig, Bode, and the meaning of zero", *Am. J. Phys.*, vol. 79, no. 10, pp. 1053–1059, Oct. 2011. DOI: 10.1119/1.3614039.

[87] S. Cohn, "Direct-coupled-resonator filters", *Proc. IRE*, vol. 45, no. 2, pp. 187–196, Feb. 1957. DOI: 10.1109/JRPROC.1957.278389.

[88] H. Blinchikoff, "Derivative of group delay at band center", *IEEE Transactions on Circuit Theory*, vol. 17, no. 4, pp. 636–637, Nov. 1970. DOI: 10.1109/TCT.1970.1083183.

[89] F. Xiao, "Some notes on group delay in bandpass filter synthesis", in *2012 Asia-Pacific Microwave Conf. Proc.*, Kaohsiung, Taiwan: IEEE, Dec. 2012, pp. 220–222. DOI: 10.1109/APMC.2012.6421552.

[90] T. Henk, "The generation of arbitrary-phase polynomials by recurrence formulae", *Int. J. Circ. Theor. Appl.*, vol. 9, no. 4, pp. 461–478, Oct. 1981. DOI: 10.1002/cta.4490090407.

[91] A. I. Zverev, *Handbook of Filter Synthesis*. Baltimore, MD, USA: John Wiley & Sons, 1967, ISBN: 0-471-98680-1.

[92] H. Matthes, "Designing high-grade delay equalizers", *NTZ-CJ*, no. 4, pp. 177–185, 1965.

[93] K. Hajek, Z. Sedlacek, and B. Sviezeny, "New circuits for realization of the 1st and 2nd order all-pass LC filters with a better technological feasibility", in *Proc. 2002 IEEE Int. Symp. Circuits and Syst.*, vol. 3, Phoenix-Scottsdale, AZ, USA: IEEE, May 2002, pp. III–523–III–526. DOI: 10.1109/ISCAS.2002.1010276.

[94] *Advanced Design System (ADS) | Keysight (formerly Agilent's Electronic Measurement)*. [Online]. Available: https://www.keysight.com/en/pc-1297113/advanced-design-system-ads?cc=US&lc=eng (visited on 05/14/2019).

[95] *Coilsys Demo for ADS 2017 - YouTube*. [Online]. Available: https://www.youtube.com/watch?v=nos_fjcic-Y (visited on 05/14/2019).

[96] *Virtuoso layout suite*. [Online]. Available: https://www.cadence.com/content/cadence-www/global/en_US/home/tools/custom-ic-analog-rf-design/layout-design/virtuoso-layout-suite.html (visited on 06/17/2019).

[97] H. C. Luong and J. Yin, "Transformer Design and Characterization in CMOS Process", in *Transformer-Based Design Techniques for Oscillators and Frequency Dividers*, Cham: Springer International Publishing, 2016, pp. 7–19. DOI: 10.1007/978-3-319-15874-7_2.

[98] S. S. Mohan, "The design modeling and optimization of on-chip inductor and transformer circuits", Doctoral thesis, Stanford University, Dec. 1999.

[99] B. Leite, "Design and modeling of mm-wave integrated transformers in CMOS and BiCMOS technologies", Doctoral thesis, Université Bordeaux 1, Nov. 2011.

[100] B. Leite, E. Kerherve, J.-B. Begueret, and D. Belot, "Design and characterization of CMOS millimeter-wave transformers", in *2009 SBMO/IEEE MTT-S Int. Microwave and Optoelectronics Conf.*, Belém, Brazil: IEEE, Nov. 2009, pp. 402–406. DOI: 10.1109/IMOC.2009.5427555.

[101] T. T. Y. Wong, *Fundamentals of Distributed Amplification*. Norwood, MA, USA: Artech House, Inc., 1993, ISBN: 0-89006-615-9.

[102] S. Amari and J. Bornemann, "Using frequency-dependent coupling to generate finite attenuation poles in direct-coupled resonator bandpass filters", *IEEE Microw. Guided Wave Lett.*, vol. 9, no. 10, pp. 404–406, Oct. 1999. DOI: 10.1109/75.798030.

[103] N. Yildirim, O. A. Sen, Y. Sen, M. Karaaslan, and D. Pelz, "A revision of cascade synthesis theory covering cross-coupled filters", *IEEE Trans. Microw. Theory Techn.*, vol. 50, no. 6, pp. 1536–1543, Jun. 2002. DOI: 10.1109/TMTT.2002.1006415.

[104] M. Zukocinski and A. Abramowicz, "Center frequency of wideband direct-coupled resonator filters", in *2012 19th Int. Conf. Microwaves, Radar Wireless Commun.*, vol. 2, Warsaw, Poland: IEEE, May 2012, pp. 726–728. DOI: 10.1109/MIKON.2012.6233575.

[105] ——, "Wideband and UWB filters with complementary couplings", in *2012 Asia-Pacific Microwave Conf. Proc.*, Kaohsiung, Taiwan: IEEE, Dec. 2012, pp. 253–255. DOI: 10.1109/APMC.2012.6421563.

[106] M. Zukocinski and A. Abramowicz, "Lossy inverters and their influence on coupled resonator filter characteristics", in *2013 IEEE Int. Conf. Microwaves, Commun., Antennas and Electron. Syst.*, Tel Aviv, Israel: IEEE, Oct. 2013, pp. 1–5. DOI: 10.1109/COMCAS.2013.6685297.

[107] M. Zukocinski, A. Golaszewski, and A. Abramowicz, "Shaping frequency characteristics of wideband direct-coupled resonator filters by means of electric and magnetic couplings", in *2014 20th Int. Conf. Microwaves, Radar and Wireless Commun.*, Gdansk, Poland: IEEE, Jun. 2014, pp. 1–4. DOI: 10.1109/MIKON.2014.6899835.

[108] M. Zukocinski and A. Abramowicz, "Design method for wideband direct-coupled resonator filters with electric or magnetic couplings", in *2015 IEEE Int. Conf. Microwaves, Commun., Antennas and Electron. Syst.*, Tel Aviv, Israel: IEEE, Nov. 2015, pp. 1–4. DOI: 10.1109/COMCAS.2015.7360450.

[109] W. Meng, H.-M. Lee, K. A. Zaki, and A. E. Atia, "Synthesis of multi-coupled resonator filters with frequency-dependent couplings", in *2010 IEEE MTT-S Int. Microwave Symp. Dig.*, Anaheim, CA, USA: IEEE, May 2010, pp. 1716–1719. DOI: 10.1109/MWSYM.2010.5517793.

[110] ——, "Synthesis of wideband multicoupled resonators filters", *IEEE Trans. Microw. Theory Techn.*, vol. 59, no. 3, pp. 593–603, Mar. 2011. DOI: 10.1109/TMTT.2010.2095032.

[111] W. Meng, K. A. Zaki, and A. E. Atia, "Prototype network synthesis for wideband microwave filters", in *2011 IEEE MTT-S Int. Microwave Symp. Dig.*, Baltimore, MD, USA: IEEE, Jun. 2011, pp. 1–4. DOI: 10.1109/MWSYM.2011.5972894.

[112] W. Meng, "Synthesis and design of microwave wideband filters and components", PhD Thesis, University of Maryland, College Park, 2014.

[113] S. Tamiazzo and G. Macchiarella, "Synthesis of cross-coupled filters with frequency-dependent couplings", *IEEE Trans. Microw. Theory Techn.*, vol. 65, no. 3, pp. 775–782, Mar. 2017. DOI: 10.1109/TMTT.2016.2633258.

[114] K. Whiting, "The effect of increased design bandwidth upon direct-coupled-resonator filters (correspondence)", *IEEE Trans. Microw. Theory Techn.*, vol. 11, no. 6, pp. 557–560, Nov. 1963. DOI: 10.1109/TMTT.1963.1125734.

[115] Q. Zhang and C. Caloz, "Alternative construction of the coupling matrix of filters with non-paraconjugate transmission zeros", en, *IEEE Microw. Compon. Lett.*, vol. 23, no. 10, pp. 509–511, Oct. 2013. DOI: 10.1109/LMWC.2013.2278275. [Online]. Available: http://ieeexplore.ieee.org/document/6588357/ (visited on 05/16/2017).

[116] P. J. Burke, "Ultra-linear chirp generation via VCO tuning predistortion", in *1994 IEEE MTT-S Int. Microwave Symp. Dig.*, San Diego, CA, USA: IEEE, May 1994, pp. 957–960. DOI: 10.1109/MWSYM.1994.335198.

[117] A. Samarah, "A novel approach for generating digital chirp signals using fpga technology for synthetic aperture radar applications", Doctoral thesis, Universität Siegen, May 2012.

[118] M. L. Sanders and J. H. Ashton, "Chirp source with rolling frequency lock for generating linear frequency chirps", US 6,091,356, Jul. 2000.

[119] A. E. Siegman, *Lasers*. Sausalito, CA, USA: University Science Books, 1986, p. 717, ISBN: 978-0-935702-11-8.

[120] *Convolve–wolfram language documentation*. [Online]. Available: https://reference.wolfram.com/language/ref/Convolve.html (visited on 08/10/2019).

[121] J. D. Cook, *Fourier transform definition conventions and formulas*, 2017. [Online]. Available: https://www.johndcook.com/blog/fourier-theorems/ (visited on 02/24/2017).

[122] B. Osgood, *Lecture notes for EE 261: The Fourier transform and its applications*, 2007. [Online]. Available: http://search.proquest.com/openview/df3b2c7642c864fde435e099b5450381/1?pq-origsite=gscholar&cbl=40569 (visited on 02/24/2017).

[123] E. W. Weisstein, *Fourier Transform*, Text, Feb. 2017. [Online]. Available: http://mathworld.wolfram.com/FourierTransform.html (visited on 02/24/2017).

[124] J. L. Gonzalez, X. Aragonés, M. Molina, B. Martineau, and D. Belot, "A comparison between grounded and floating shield inductors for mmW VCOs", in *Proc. 33rd Eur. Solid-State Circuits Conf.*, Sevilla, Spain: IEEE, Sep. 2010, pp. 250–253. DOI: 10.1109/ESSCIRC.2010.5619882.

[125] N. Derrier, C. Deglise, C. Durand, T. Quemerais, and D. Gloria, *Bicmos9mw modeling training v2.0*, STMicroelectronics, Crolles, France, Sep. 2015.

université PARIS-SACLAY
ÉCOLE DOCTORALE
Physique et ingénierie : électrons, photons, sciences du vivant (EOBE)

Titre : Contribution à la Conception d'un Transformateur de Fourier Temps Réel en Technologie Intégrée

Mots clés : traitement du signal analogique, temps réel, transformateur de Fourier à modulation de fréquence, rétard de groupe arbitraire, filtre dispersif, circuit intégré

Résumé : L'accroissement constant des bandes passantes et des débits dans les applications de la vie courante (e.g., télécommunications, objets connectés), comme dans des applications plus spécialisées (e.g., radar, observations en radioastronomie), impose de très fortes contraintes en termes de vitesse, consommation de puissance et dissipation thermique aux étages de conversion analogique-numérique des chaînes d'acquisition. Par conséquent une tendance actuelle consiste à effectuer le traitement de signaux (e.g., transformation de Fourier) dans le domaine analogique pour pouvoir traiter des signaux ultra-large bande avec faible latence et de manière plus efficace en termes énergétiques. Plusieurs architectures de traitement de signal analogique repose sur des blocs encore peu explorées dans la littérature : les filtres à retard de groupe arbitraires. Ces filtres sont plutôt réalisés en technologie SAW ou avec des structures microondes discrètes (non intégrés), conduisant à des filtres avec des bandes passantes limitées et beaucoup de pertes, dans le cas des dispositifs SAW, ou avec un encombrement et poids importantes, dans le cas des filtres microondes. Très peu de réalisations intégrées en semi-conducteurs ont été reporté à ce jour.

L'innovation présentée dans cette thèse a deux aspects, un aspect architectural au niveau système, lequel a donné lieu à une proposition d'architecture pour un transformateur de Fourier analogique permettant d'améliorer les performances en précision par rapport aux autres architectures rapportées dans la littérature, et un aspect concernant le développement des méthodes de conception de filtres à retard de groupe linéaire et leur implémentation dans une technologie de circuit intégré. Trois réseaux de filtres différents ont été conçus en utilisant ces méthodes, un filtre passe-bande à minimum de phase dans une structure en échelle, un réseau passe-tout équilibré avec un retard de groupe linéaire à pente positive et un réseau passe-tout non équilibré avec un retard de groupe linéaire de pente négative. Il a aussi été démontré que les filtres passe-tout peuvent être transformés dans des filtres transversales basé sur la structure d'un amplificateur distribué.

Title : Contribution to the Design of a Real-Time Fourier Transformer in Integrated Technology

Keywords : analog signal processing, real-time, chirp Fourier transformer, engineered group delay, dispersive delay line, integrated circuit

Abstract : The constant increase of bandwidths and bitrates in everyday applications (e.g., telecommunications, internet of things), as also in more specialized applications (e.g., radar, radio astronomy observations), imposes stringent constraints in terms of speed, power consumption and heat dissipation at the analog-to-digital conversion stages of acquisition chains. Therefore, a current trend is to perform signal processing (e.g., Fourier transform) in the analog domain to be able to process ultra-wideband signals with low latency and in a more energy-efficient way. Many of the analog signal processing architectures rely on blocks that have not been widely explored in the literature: arbitrary group delay filters. These filters are generally realized in SAW technology or with discrete (non-integrated) microwave structures, leading to filters with limited bandwidth and high loss, in the case of SAW devices, or with a large size and weight, in the case of microwave filters. Very few integrated circuit implementations have been reported to date.

The innovation presented in this thesis has two aspects, a system-level architectural aspect, which gave rise to the proposal for an analog Fourier transformer architecture that enables improve the precision performance when compared to the previously reported architectures, and an aspect concerning the development of linear group delay filter design methods and their implementation in an integrated circuit technology. Three different filter networks were designed using these methods, a minimum phase band-pass ladder filter, a balanced all-pass network with positive-slope linear group delay, and a balanced all-pass network with a linear group delay of negative slope. It has also been shown that the all-pass filters can be transformed into distributed amplifier-based transversal filters.

Université Paris-Saclay
Espace Technologique / Immeuble Discovery
Route de l'Orme aux Merisiers RD 128 / 91190 Saint-Aubin, France